Electrokinetic Locomotion

Jeffrey Lawrence Moran

A dissertation
submitted in partial fulfillment of the
requirements for the degree of

Doctor of Philosophy

University of Washington

2013

Reading Committee:

Jonathan D. Posner, Chair

James J. Riley

Daniel T. Schwartz

Program Authorized to Offer Degree:
Mechanical Engineering
University of Washington

University of Washington

Abstract

Electrokinetic Locomotion

Jeffrey Lawrence Moran

Chair of the Supervisory Committee:
Associate Professor Jonathan D. Posner
Department of Mechanical Engineering

Background. The past decade has seen the rapid development of synthetic particles capable of propelling themselves at the micro- and nanometer scale through aqueous media. Several groundbreaking experiments have shown these so-called "nanomotors" to be capable of performing several useful microscale tasks. However, alongside this progress, the need has arisen to understand the physical mechanisms governing their motion, as well as the limitations on their capabilities. Explanations of the propulsion mechanisms driving synthetic nanomotors are critical not only for providing insight into novel physical phenomena, but also to guide and inform the design and implementation of nanomotors and nanomachines.

Bimetallic rods, 2 microns in length, were first shown to move autonomously using hydrogen peroxide fuel in 2004. Since then, a number of theories have been proposed to explain how these particles convert chemical energy in the hydrogen peroxide to kinetic energy of motion. The leading theory states that the rod functions as a short-circuited electrochemical cell, with electrochemical reactions occurring asymmetrically on its surface. These reactions are thought to generate an electric field, which propels the particle via electrophoresis. However, until now, this mechanism has not received a rigorous theoretical treatment as it applies to bimetallic rods, hindering the development of these particles for practical applications.

Research Goals. The goals of this dissertation are (*i*) to understand physically the motion of self-propelling metallic particles with electrochemical surface reactions, and (*ii*) to characterize the limitations on the propulsion mechanism. To accomplish these goals, I construct a complete numerical model for the motors using the finite-element method. The model includes the coupled Poisson-Nernst-Planck-Stokes equations with Frumkin-corrected Butler-Volmer boundary conditions to represent the surface reactions. I devote special attention to the transport phenomena occurring in the interfacial layer near the particle/solution interface, which play a key role in the locomotion.

The model enables one to understand how the rods' motion depends on the properties of their environment, such as hydrogen peroxide concentration, solution electrical conductivity, and solution viscosity. The numerical simulations are complemented with a scaling analysis based on the governing equations, which makes definite, verifiable predictions of these dependences. One of the most important trends that has been observed experimentally is the significant decrease in speed induced by adding sub-millimolar concentrations of inert electrolyte. It is important to understand the physical reasons for the electrolyte-induced speed decrease, in order to know whether it is fundamental to this propulsion mechanism, or if there is some feasible means to circumvent it.

Research Impact. Successful completion of this research will result in an improved understanding of the capabilities, as well as the risks and limits of applicability, of the bimetallic nanomotors for applications in nanotechnology and nanomedicine. Potential applications of the rods include the targeted delivery of drugs in the human body, sensing of chemical impurities in drinking water, and as engines to drive fabrication of microscale structures.

TABLE OF CONTENTS

Page

LIST OF FIGURES

Figure Number Page

LIST OF TABLES

DEDICATION

to my mother and father,
with love and gratitude

ACKNOWLEDGMENTS

This work was generously supported by the National Science Foundation through a Graduate Research Fellowship and grant CBET-0853379.

Throughout my graduate studies, I have benefited from numerous interactions with mentors, colleagues, and friends, and it is my distinct pleasure to acknowledge them here.

First and foremost, I wish to sincerely thank my advisor, Jonathan D. Posner, for introducing me to challenging problems in microfluidics and giving me the freedom to work independently on a project of my own choosing. His intellect, patience, positive energy, and mentorship were a constant source of motivation and made me a better researcher and communicator.

I am grateful to my Supervisory Committee of Christopher Bretherton, James Riley, Daniel Schwartz, and Amy Shen, who have not only enriched this thesis through challenging coursework and stimulating intellectual discussions, but also provided me with invaluable career advice and encouraged me to push through the last few months of graduate school. I especially thank Profs. Riley and Schwartz for serving on my thesis Reading Committee.

Outside of my immediate academic circle, several noteworthy individuals have provided inspiration and motivation along the way. Charles Dupré, my high school chemistry and physics teacher, got me truly excited about science. While at ASU I studied the double bass for two years with Dwight Kilian, who taught me to hit the ground running in life, and to always play in tune. Finally, Prof. Brian Greene of Columbia University has helped me to discover the joy in communicating science

to the general public, and to fully appreciate the meaning and fulfillment in being a scientist.

My labmates in the Posner Research Group have been some of my greatest friends throughout graduate school. My experience at ASU was enriched by Charlie Corredor, Wen-Che Hou, Abhishek Jain, Jung-Yeul Jung, Steven Klein, Nathan Marine, Babak Moghadam, Guru Navaneetham, Carlos Pérez, Kamil Salloum, Michael Schroeder, Juan Tibaquirá, and Philip Wheat, with whom I have savored every lunch, hiking excursion, and late-night intellectual discussion over the years. I will fondly remember the summer that Babak, Charlie, and I spent moving from Tempe to Seattle. Since making the move to UW, I have enjoyed working with Mark Borysiak, Jesse Butterfield, Kelly Connelly, Allison Pinto, William Walker, Jay Wolfer, Jianzhu Yin, and Zhenya Yuferova. In addition to being good friends, Nathan and Babak were fantastic roommates in Tempe and Seattle respectively. I thank Philip for performing the experiments discussed in Chapters 4 and 5 of this thesis.

My heartfelt gratitude goes out to my wonderful girlfriend, Jayme Kurland, who dealt with my move to Seattle and the resulting 21 months we spent living apart with grace and aplomb and has been a never-ending source of encouragement, love, and support; and to my brother, Daniel Moran, who continues to inspire me musically, philosophically, and personally. I treasure our friendship and mutual respect.

Finally, I dedicate this thesis to my parents, Michael Moran and Angelica Panos, who have believed in me and loved me unconditionally since the very beginning. Thank you for everything.

CITATIONS TO PREVIOUSLY PUBLISHED WORK

Portions of this thesis have appeared in the following published articles:

Chapters 2 and 4

J.L. Moran, P.M. Wheat, and J.D. Posner. Locomotion of electrocatalytic nanomotors due to reaction induced charge autoelectrophoresis. *Phys. Rev. E* 2010, Vol. 81, No. 6, 065302.

Chapters 2 and 5

J.L. Moran and J.D. Posner. Electrokinetic Locomotion due to Reaction Induced Charge Auto-Electrophoresis. *J. Fluid Mech.* 2011, Vol. 680, 31-66.

Chapter 1

INTRODUCTION

1.1 Motivation

The development of self-propelling micro- and nanometer scale motors capable of performing useful tasks is one of the grandest challenges facing nanotechnology today. The fabrication and analysis of micro- and nanometer scale devices capable of self-propelled motion in aqueous solutions has grown exponentially since the turn of the century [47, 74, 45, 38, 68]. These so-called "nanomotors" hold great promise for a wide variety of applications in nanotechnology, including cargo transport and delivery [10, 96], self-assembly of nanostructures [91], chemical sensors [50], and useful nanomachinery [97]. The realization of a self-propelling swimmer capable of performing useful tasks at the nano-scale would trigger a revolution in nanotechnology, and remains one of the grandest challenges facing the field ever since Richard Feynman issued a challenge to create the first "tiny motor" in his 1959 lecture "There's Plenty of Room at the Bottom."

Locomotion at the micro-scale is both abundant and important in nature, where microorganisms harvest chemical energy from the surrounding fluid environment and convert it to the mechanical energy of motion through a variety of processes. Examples include human spermatozoa, which must swim through hostile environments to fuse with an ovum during fertilization; the alga *Chlamydomonas reinhardtii*, which swims by beating two flagella in a variety of patterns which vary stochastically; and the unicellular protozoan *Paramecium*, which swims using thousands of cilia to evade predators [59]. At this size scale, mechanical swimming is no small feat: the so-called low Reynolds number regime is inherently unfavorable for mechanical swimming, where the swimmer's inertia exerts a negligible influence compared to viscous forces. In order to overcome this difficulty, any mechanical micro-swimmer must move by deforming itself in a time-irreversible manner; this axiom is known as Purcell's Scallop Theorem [81]. Thus, any microorganism that propels itself by mechanical means, such as a motile *Escherichia coli* bacterium or a human spermatozoon, must swim by a time-asymmetric deformation of a solid appendage, such as a single flagellum or thousands of cilia.

In 1956, the British biochemist Peter Mitchell proposed that in contrast to mechanical swimmers, some microorganisms might move by a non-mechanical propulsion mechanism [67]. He envisioned an organism that exchanges ions with the surrounding fluid, generating an ion current in the fluid near its body that flows opposite the swimming direction; this ion current leads to fluid motion, also opposite the swimming direction, propelling the organism in the same way as a track leads to the locomotion of a tank. Non-mechanical propulsion mechanisms have been investigated for specific types of organisms, *e.g.* by Mitchell [66], Waterbury *et al.* [99], and Anderson [2].

Recent advances in nanofabrication have enabled the engineering of synthetic analogues to naturally occurring micro-swimmers. Some artificial swimmers have emulated biological systems using moving interfaces such as rotating structures [12, 34], flagella powered by external magnetic fields [100, 37, 8], or deforming bodies [3] or artificial cilia [87]. However, many practically realized artificial swimmers also move by non-mechanical propulsion mechanisms similar to that proposed by Mitchell. A common thread among these is surface reactions, which establish gradients in chemical concentration or electric potential which generate fluid slip along the synthetic swimmer surface, setting it into motion (a so-called *phoretic propulsion mechanism*). To properly quantify these gradients and the influence they exert, it is often necessary to solve non-trivial fluid mechanics and transport problems, thus posing interesting problems for theoreticians.

An understanding of the physical mechanisms driving self-propulsion of natural and synthetic objects is essential not only for probing fundamental scientific problems, but also for the practical and rational design and implementation of micro- and nanoscale swimming devices, particularly for determining their usefulness for future applications. Experimental advances in artificial self-propellers are rapidly progressing [72, 97, 31, 36], but the applicability of synthetic self-propellers will be fundamentally limited until their mechanisms of energy conversion are thoroughly understood.

This thesis will focus on one particular realization of a synthetic swimmer known as a *bimetallic nanorod* or *nanomotor*. These rods were initially reported in 2004 to move autonomously along their axis in hydrogen peroxide solutions [74]. The rods are typically 2 microns in length, 300 nanometers in diameter, and consist of platinum and gold segments of equal length. Since their introduction, they have been shown to be capable of several potentially useful tasks in nanotechnology, such as towing and delivery of microscale cargo [96, 10], motion at up to 100 body lengths per second [58], externally controllable motion [10, 11], and motion-based chemical sensing [50]. The rods are touted as one of several candidates for a variety of applications in nanotechnology, such as targeted delivery of drugs in the human body, chemical sensors, sensing and removal of impurities in drinking water, and the fabrication of complex nanoscale structures.

Although the rods hold significant promise for practical applications, the physics governing their motion is not well understood. Considering that the rods have no moving parts, the governing propulsion mechanism is believed to be phoretic in nature. Several non-mechanical theories have been proposed to explain the mechanism of conversion of chemical to mechanical energy, some of which have garnered experimental support [74, 98, 76], but the theories that have been advanced thus far are generally qualitative in nature. To gain a more rigorous understanding, we seek to build the first quantitative theoretical model for the self-propulsion of bimetallic nanorods.

The study of micro-scale locomotion by non-mechanical means has a long history, dating at least as far back as Mitchell's proposal for microorganisms. To gain some context for the current work, we review the fundamentals of phoretic self-propulsion and discuss the most pertinent literature relating to the two most common realizations: self-electrophoresis and self-diffusiophoresis.

1.2 Literature Review on Phoretic Self-Propulsion

The word *phoresis* means “migration” and in transport science generally refers to the motion of dispersed particles or ions relative to a fluid under the influence of a gradient in a scalar quantity. The most common phoretic mechanisms are electrophoresis, diffusiophoresis, and thermophoresis, in which a particle moves in response to a gradient in electrical potential, chemical concentration, or temperature, respectively. Phoretic self-propellers are generally governed by the same physical principles as conventional phoretic particles, which are well-understood physically and have been analyzed in detail elsewhere. The distinguishing feature of phoretic swimmers is that they *generate* the propulsive gradients themselves, rather than requiring the gradient to be externally applied.

A general framework for analyzing phoretic swimmers was provided by Golestanian *et al.* [38]. They presented several designs for spherical and rod-shaped particles and considered self-electrophoresis, self-diffusiophoresis, and self-thermophoresis as possible mechanisms. Importantly, they identified two essential traits a phoretic swimmer must have in order to move: *surface activity* and *phoretic mobility.* By definition a phoretic swimmer migrates in response to a self-generated gradient in a scalar quantity. Surface activity describes the swimmer’s *ability to generate* the gradient; it is equal to the mass flux (for self-diffusiophoresis), current density (for self-electrophoresis), or heat flux (for self-thermophoresis) crossing the surface of the swimmer. Phoretic mobility quantifies how the swimmer *responds to* the gradient, and is a measure of the swimmer’s migration speed per unit of the gradient in temperature, potential, or concentration.

Golestanian *et al.* derive a general scaling relation for the speed of a phoretic swimmer:

$$U \propto \frac{\alpha\mu}{B}, \tag{1.1}$$

where α is the surface activity, μ is the phoretic mobility, and B is the solute diffusivity (for self-diffusiophoresis), solution electrical conductivity (for self-electrophoresis), or thermal conductivity (for self-thermophoresis). For self-electrophoresis, the phoretic mobility is equal to the electrophoretic mobility, given by the familiar Helmholtz-Smouluchowski expression as $\mu_e = \varepsilon\zeta/\eta$, where ε is the permittivity of the solution, ζ is the particle's zeta potential, which quantifies its surface charge, and η is the dynamic viscosity of the fluid. Diffusiophoretic and thermophoretic mobilities may be defined as well, but typically depend on the situation (*e.g.*, which solute exhibits the gradient, particle geometry, etc.).

Golestanian *et al.* argue that symmetry breaking in either surface activity and/or phoretic mobility is essential for swimming. For example, for a two-sided Janus sphere with homogeneous phoretic mobility and broken symmetry in the surface activity (one hemisphere produces a flux of heat, species, or ions while the other consumes it) they obtain the analytical result for the swimming speed

$$U_{Janus} = \frac{1}{8B}(\alpha_- - \alpha_+)(\mu_+ + \mu_-), \tag{1.2}$$

where + and − subscripts indicate the respective half of the sphere on which the quantity is evaluated. This equation predicts that a Janus swimmer with uniform surface activity ($\alpha_+ = \alpha_-$) will not move. Indeed, all successful realizations of Janus swimmers reported in the literature, from bimetallic rods [74] to polystyrene spheres half-coated with platinum [45], exhibit some form of broken symmetry in surface activity.

In this work, we will consider the motion of a particle that arises in part due to gradients in both concentration and electric potential. In the following subsections, we describe pertinent theoretical examinations of self-electrophoresis and self-diffusiophoresis. In each case, we begin with a brief introduction to the most common mathematical models used to describe these propulsion mechanisms, and then summarize and critique the most recent contributions and refinements to the modeling.

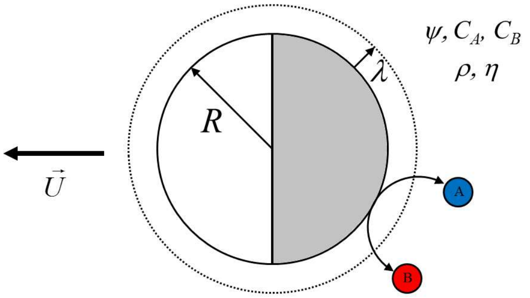

Figure 1.1: Schematic of a typical spherical swimmer which moves by neutral solute self-diffusiophoresis. A Janus sphere having catalytic (shaded) and inert (white) halves of radius R is immersed in a fluid with viscosity η containing A and B solute molecules with equilibrium concentrations C_A and C_B. In general, the A and B molecules experience different interactions with the swimmer. The solutes and particle can interact through many different mechanisms, such as van der Waals forces, steric interactions, electrostatics, and more; the interaction is described by a potential ψ and has characteristic length scale λ. For example, if the catalytic half of the particle converts A molecules into B molecules, this will cause a local excess of B molecules and depletion of A molecules. This process produces an asymmetric distribution of reactants and products, which implies asymmetric interaction forces on the particle. These forces, integrated over the entire particle surface, lead to a propulsive force on the particle.

1.2.1 Self-diffusiophoresis

Background

Self-diffusiophoresis is the autonomous motion of a particle up or down a self-generated gradient in chemical concentration. Self-diffusiophoresis is the autonomous analogue to diffusiophoresis, the migration of a particle in response to an externally imposed concentration gradient. The solute in which the gradient exists may be either uncharged (non-electrolyte or neutral solute diffusiophoresis) or charged (electrolyte diffusiophoresis).

For an uncharged solute, diffusiophoretic motion arises from generalized interactions between the solute(s) and the particle (*e.g.*, van der Waals forces, steric interactions, electrostatics, or osmotic pressure), which lead to a net propulsive force on the particle when the solute concentration is non-uniform. An asymmetry in the interaction forces leads to a corresponding asymmetry in fluid pressure, causing pressure gradients to form, which drive fluid flows. Thus, the fluid is set into motion due to the concentration imbalance.

For an electrolyte, diffusiophoresis is driven by two components: electrophoresis, which occurs due to an electric field established by asymmetric diffusion of positive and negative ions; and chemiphoresis, which is the electrolyte analogue of non-electrolyte diffusiophoresis, and results from the gradient in chemical potential associated with the salt concentration gradient. Externally driven diffusiophoresis has been known since the work of Derjaguin and others [20, 24], and was analyzed more recently for non-electrolytes by Anderson *et al.* [1] and for electrolytes by Prieve *et al.* [80], Keh & Wei [51], and Hsu *et al.* [46].

The seminal analysis of externally driven diffusiophoresis in an uncharged solute gradient was provided by Anderson *et al.* [1]. They considered a spherical particle in an infinite fluid in which a neutral solute exhibited a constant gradient and showed that the direction of motion of the particle depends on the nature of the interaction forces between the solute and particle. If the interaction is attractive, the particle will move toward higher solute concentrations; if it is repulsive, the particle will move toward lower solute concentrations. For the particle speed, they obtained the leading order result

$$U_0 = \frac{k_B T}{\eta} L^* K \frac{\mathrm{d}C}{\mathrm{d}x}, \tag{1.3}$$

where k_B is Boltzmann's constant, T is the absolute temperature, $\mathrm{d}C/\mathrm{d}x$ is the externally imposed concentration gradient, and L^* and K are two parameters relating to the potential profile of solute near the particle. K is commonly referred to as the Gibbs adsorption length and is related to the amount of excess solute adsorbed onto the surface. L^* is the first moment of the solute distribution and serves as a characteristic length scale for the particle-solute interaction. This relatively simple expression for externally driven diffusiophoresis captures much of the same physical ideas that would later describe self-diffusiophoretic swimmers.

Prieve *et al.* extended this analysis to motion of particles in electrolyte gradients (electrolyte diffusiophoresis) two years later [80] and described the two components of electrolyte diffusiophoresis in detail. They showed that the electrophoretic component ultimately arises from the fact that an electrolyte gradient consists of two species (the cation and the anion), and these two species have opposite charge and (generally) unequal mobilities. If a charged particle is immersed in an electrolyte gradient, then the concentration of both cations and anions is relatively high on one side of the particle and relatively low on the other. Due to their unequal mobilities, the ions will migrate down their respective gradients at different rates (creating a *diffusion current*). Over time, the faster ion accumulates on the low-concentration side more quickly than the slower ion, creating an asymmetry in charge. In turn, this asymmetry establishes a *diffusion potential* and an associated electric field, which drives a current equal and opposite to the diffusion current. Thus, at equilibrium, zero net current flows through the system. The electric field exerts a force on the charged particle, propelling it into motion by electrophoresis.

The chemiphoretic component is the electrolyte analogue of neutral-solute diffusiophoresis, and results from a propulsive force caused by the polarized diffuse layer of ions surrounding the particle. Because the bulk electrolyte concentration is higher to one side of the particle than the other, the diffuse screening layer is thinner on the side with higher bulk concentration. This leads to an asymmetric electrostatic interaction force between the particle and ions, producing a propulsive force on the particle toward the higher concentration of counterions (ions with opposite charge from the particle surface). Thus, the chemiphoretic component always directs the particle toward the higher concentration of counterions.

The direction of motion in electrolyte diffusiophoresis depends on the relative dominance of the electrophoretic and chemiphoretic components. The electrophoretic component can direct the particle in either direction, depending on the sign of the product $\beta\zeta$, where

$$\beta \equiv \frac{D_+ - D_-}{D_+ + D_-} \tag{1.4}$$

and ζ is the zeta potential of the particle. If $\beta\zeta > 0$, the electrophoretic component moves the particle up the gradient (toward high salt concentration). If $\beta\zeta < 0$, the particle is propelled toward lower salt concentration. If the mobilities are symmetric, *i.e.* if the cation and anion mobilities are equal, β vanishes and there is no electrophoretic contribution to the motion; in this case the motion occurs purely by chemiphoresis.

Self-diffusiophoresis is governed by the same physical principles as diffusiophoresis, except the gradients are generated by the swimmer itself, usually through some form of surface fluxes of species.

Neutral Solute Self-Diffusiophoresis

Many realizations of diffusiophoretic swimmers have been theorized or demonstrated to move under the influence of self-generated gradients in neutral solutes. Many of these swimmers are simple Janus particles, *i.e.* microspheres with one half coated with a catalytic material. The catalyst promotes the asymmetric generation and/or consumption of solute molecules, leading to a non-uniform distribution of solutes, producing unbalanced interaction forces which cause propulsion of the particle. This basic model for self-diffusiophoresis has been studied theoretically by Popescu *et al.* [78], Golestanian *et al.* [39], and Córdova-Figueroa & Brady [15], and was studied experimentally by Howse *et al.* [45]. Other experimental studies of diffusiophoretic motors have considered doublets of Janus spheres [29], Janus particles created from fluorescent polymer spheres (to reveal the direction of motion) [32], particles that polymerize a monomer solute molecule creating a propulsive gradient in monomer concentration [73], and Janus swimmers of varying size [30]. The latter study showed an inverse dependence of swimming speed on particle diameter, in agreement with theoretical predictions.

The first detailed theoretical model of a diffusiophoretic self-propeller was provided by Golestanian *et al.* [39], who analyzed a spherical swimmer with a single enzymatic reaction site on its surface that releases product particles (much smaller than the sphere) at a given rate, while the rest of the surface is impermeable. Since they are only generated at one point on the surface, the resulting distribution of product particles is non-uniform about the sphere. This non-uniform distribution results in a phoretic slip velocity and particle motion by self-diffusiophoresis. The product particles, having a concentration C, obey the time-dependent diffusive conservation law with a source term added to account for the reactions:

$$\frac{\partial C}{\partial t} - D\nabla^2 C = \frac{\mathrm{d}N_p}{\mathrm{d}t}\delta_D^3(\mathbf{r}-\mathbf{r}_S), \tag{1.5}$$

where $\mathrm{d}N_p/\mathrm{d}t$ is the rate of release of product particles, δ_D is the Dirac delta function, and $\mathbf{r}_S$ is the location of the catalytic site on the surface of the sphere. Since the reactions are explicitly accounted for in the governing equation, the boundary condition for the product particles simply expresses an impermeable surface,

$$\mathbf{r}\cdot\nabla C = 0. \tag{1.6}$$

The reaction rate is assumed not to depend on fuel concentration, which is not tracked in their analysis. The resulting asymmetry in the product particle distribution produces a first moment C_1 in the concentration distribution about the particle,

$$C_1(t) = \int_0^\pi C(r=R,\theta,t)\sin\theta\cos\theta d\theta. \tag{1.7}$$

Here R is the radius of the particle. This definition of the first moment is distinct from the definition provided by Anderson *et al.* (see (1.3)) for externally driven diffusiophoresis. In the latter case, the first moment is a length scale related to the equilibrium distribution of solute near the surface; in (1.7), the first moment has units of concentration (or number density) and expresses the asymmetry of the concentration of products near the particle. Thus, here C_1 is a measure of the strength of the concentration gradient generated by the enzymatic reaction. Making use of a result from Anderson [2], they argue that the particle speed U depends linearly on the first moment, such that

$$U = \frac{k_B T}{\eta} \frac{\lambda^2}{R} C_1, \tag{1.8}$$

where λ is a characteristic length scale for the solute-particle interactions. This equation is similar to the result obtained for conventional diffusiophoresis (1.3), with C_1/R acting as an effective concentration gradient generated by the surface reactions. Unsurprisingly, (1.8) implies that the speed of the motor depends on the type of solute-particle interaction. Different interactions have different characteristic length scales associated with them. One example interaction mechanism considered by Golestanian *et al.* is the steric exclusion of product particles, which is manifested as a repulsive force between the product particles and the spherical swimmer. As described by Staffeld and Quinn, the length scale for steric interactions is defined in terms of the potential energy profile as a function of separation from the particle [95]. For latex particles in gradients of Dextran concentration, they obtain $\lambda \approx 38$ nm.

Insertion of (1.7) for the first moment into (1.8), which is calculated by solving the diffusion equation (1.5), yields an expression for the time-dependent swimming speed of the particle:

$$U(t) = a \frac{3\lambda^2}{4R^2} \int \frac{d\omega}{2\pi} \frac{e^{-i\omega t} f(\omega) \left[1 - i\sqrt{\frac{i\omega R^2}{D}}\right]}{1 - i\sqrt{\frac{i\omega R^2}{D}} - \frac{i\omega R^2}{2D}}. \tag{1.9}$$

Here a is the radius of the product particles and $f(\omega)$ is the Fourier transform of $\mathrm{d}N_p/\mathrm{d}t$. This expression tells explicitly the relationship between the particle speed and the reaction rate. The authors go on to show that for a constant reaction rate with continuous generation of product particles, the swimming speed rapidly asymptotes to a steady-state value. On the other hand, for periodic particle release, with a well-defined time interval between release of individual particles, the swimming velocity fluctuates significantly. The magnitude of the fluctuations is controlled by the balance between the particle release time interval, τ, and the time required for the product particles to diffuse along the partical and equilibrate their profile. Therefore, for a stable swimming velocity, the reaction time interval must be much smaller than the characteristic diffusion time, in order to sustain the concentration gradient which is crucial to propulsion.

In a real self-diffusiophoretic system, it is likely that the reaction rate is constant relative to the time scale of solute diffusion, but depends on position along the motor surface and fuel/solute concentration. With this in mind, Golestanian *et al.* propose a possible kinetic mechanism for the enzymatic reaction leading to propulsion. The authors assume that the fuel is decomposed into two products (*e.g.*, hydrogen peroxide decomposing to oxygen and water) in a multi-stage reaction pathway that is accelerated by the presence of the catalyst. The catalyst functions as an enzyme in the familiar Michaelis-Menten framework for enzymatic kinetics. Thus the authors propose that the mean rate (mean inverse reaction time) for this reaction is given by a Michaelis-Menten expression

$$\frac{1}{\tau} = \frac{K_M}{k_1}\frac{C_{fuel}}{K_M + C_{fuel}}, \tag{1.10}$$

where C_{fuel} is the background fuel concentration, K_M is the Michaelis constant which depends on the rate constants for the intermediate reaction steps, k_1 is the rate constant for the initial adsorption step, and τ is the reaction time interval. Equation (1.10) predicts a form for the speed of the swimmer that is linear at low fuel concentration and asymptotically approaches a constant value at high fuel concentration.

Howse *et al.* [45] realized this system experimentally by creating Janus particles by half-coating polystyrene spheres in platinum and immersing them in hydrogen peroxide solutions. In this scenario, platinum functions as the artificial enzyme in the reaction scheme analyzed by Golestanian *et al.* [39] by catalyzing the decomposition of peroxide to water and oxygen, leading to a concentration gradient of oxygen surrounding the particle. Since oxygen molecules experience an interaction force with the particle, the distribution results in a non-uniform interaction force distribution and a propulsive flux on the particle. The authors measure the speed as a function of peroxide concentration and obtain a curve with negative curvature (concave downward), in agreement with the predictions of the Michaelis-Menten model (1.10) employed in [39]. Although Howse *et al.* argue in favor of self-diffusiophoresis as the operative propulsion mechanism for their particles, they do not mention which interaction force is thought to be operative between the oxygen molecules and the particle, and thus leave unanswered the question of the origin of the diffusiophoretic force in their system.

Córdova-Figueroa & Brady [15] considered theoretically a spherical Janus particle with a reactive half and a non-reactive half, similar to the particles of Howse *et al.*, which generates and/or consumes finite-size solute particles on the reactive half due to a catalytic reaction. These solute particles are much smaller than the swimmer, but are sufficiently large that they can be described by the equations of colloidal dynamics. Thus this situation is not necessarily analogous to the experiments of Howse *et al.*. In a similar fashion to conventional osmosis through a semi-permeable membrane, a slip flow is induced from the low to high particle concentration side, and the resulting gradient in osmotic pressure leads to a pressure difference across the particle surface, which yields a propulsive force on the particle toward the low-concentration side.

To compute the osmotic force, it is necessary to solve for the distribution of solute particles. The particles are produced by a reaction $\mathrm{R} \to s\mathrm{P}$, where R is the reactant particle and P the product particle, with stoichiometric ratio s. As long as $s \neq 1$, or if the diffusivity of the product particles is different from that of the reactnats, the osmotic pressure on the particle will be unbalanced and the particle will move. The distributions of the solute particles are governed by Laplace's equation, $\nabla^2 n_{R,P} = 0$, and the reaction at the surface is assumed to be first-order in the reactant concentration, *i.e.* $r = kn_R$, with k as a reaction velocity that functions as a rate constant. To describe the relative importance of reactions to diffusion, the authors define the Damköhler number as

$$Da = \frac{k(a+b)}{D_R}, \tag{1.11}$$

where a is the swimmer radius, b is the solute particle radius, and D_R is the diffusivity of the reactant particles.

All results shown in this work are for the case where the swimmer simply consumes reactant particles and does not release product particles ($s = 0$), and/or the product particles diffuse much more quickly than the reactants. In either case, the osmotic pressure distribution depends primarily on the reactant particle concentration. The swimmer is shown to move toward the low-concentration region created by the reactions, *i.e.* towards the catalytic end (in contrast to diffusiophoretic swimmers, which typically move away from the catalyst). The speed of the osmotic propulsion increases with Damköhler number up until $Da \approx 10$, at which point the speed levels off. This is because, even in the regime where reactions are much faster than diffusion ($Da \gg 1$), the swimming speed is still limited by the diffusion of reactant molecules because in the fast-reaction limit, the reactant particles are almost completely depleted around the catalyst site and the reaction rate is naturally limited by mass transport of reactant to the catalyst. There is not universal agreement on the validity of the osmotic mechanism: some researchers have expressed concerns with the physical details [33, 49], to which the authors have replied [16, 17].

Discussion

Most rigorous theoretical analyses of self-diffusiophoresis have been variations on a rather narrow theme: they have focused on spherical swimers, with varying fractions of the surface covered in catalyst, that move by generating gradients of neutral solutes. So far, this scenario has been realized with the Pt/polymer Janus spheres studied by Howse *et al.* [45]. By and large, the advances in the field of diffusiophoretic swimming in the past few years have been mostly theoretical.

On the other hand, there appears to be no corresponding analysis focusing specifically on diffusiophoretic swimming due to self-generated electrolyte gradients. The corresponding problem of externally driven electrolyte diffusiophoresis has received attention from Prieve *et al.* [80] and Keh & Wei [51]. Some experimental papers have claimed to observe electrolyte self-diffusiophoresis, often catalyzed by external illumination or the addition of a particular species to the solution. However, due to the need for external stimuli, these examples cannot be considered true instance of electrolyte self-diffusiophoresis. Indeed, it seems that an autonomous swimmer which generates an electrolyte gradient and moves solely in response to that gradient has yet to be demonstrated theoretically or experimentally. Anderson [2] argued that the speed of a particle undergoing motion due to an externally applied electrolyte gradient ∇C_∞ would scale as

$$U \propto \frac{k_B T}{\eta} \lambda_D^2 \left[\frac{ze\zeta}{2k_B T} \beta - \ln(1-\xi^2) \right] |\nabla C_\infty|, \tag{1.12}$$

where λ_D is the Debye length (the characteristic length scale of electrostatic interactions between the particle and ions), β is defined in equation (1.4), and $\xi = \tanh(ze\zeta/4k_B T)$. This expression suggests that, if the same physics hold true for a self-diffusiophoretic swimmer in an electrolyte gradient, the speed should scale directly with the square of Debye length, or inversely with the solute concentration and hence inversely with solution electrical conductivity. Thus, a self-diffusiophoretic motor may suffer a speed reduction in conductive solutions, as has already been observed [76] and predicted [38, 84] in the case of self-electrophoretic swimmers.

On the other hand, Keh & Wei [51] (see Figs. 4 and 5 in their paper) predict that the diffusiophoretic mobility of a sphere with a constant surface charge would *increase* as the ratio of particle radius to Debye length is increased, implying that diffusiophoretic swimmers should move *faster* in more concentrated electrolytes. The dependence of electrolyte self-diffusiophoretic propulsion on electrolyte strength is a key unanswered question that does not appear to have been addressed in the literature.

In general, the study of self-diffusiophoresis would benefit greatly from more real-world realizations. So far, the prototypical diffusiophoretic swimmer is the half-coated Janus sphere studied by Howse *et al.* [45]. The wealth of theoretical findings which have been summarized in this section should inform and inspire a variety of practical applications for diffusiophoretic motors, having varied geometries and moving by different catalysts and fuels. In particular, diffusiophoretic motors might provide an alternative to electrophoretic motors. However, predictions differ as to whether an increase in electrolyte strength will cause an increase or decrease in diffusiophoretic velocity. At this point, what is needed is a working prototype of a motor which moves unambiguously by electrolyte self-diffusiophoresis. Studies into such a swimmer's behavior could elucidate fully the dependence of self-diffusiophoretic speed on ionic strength.

1.2.2 Self-electrophoresis

Background

Self-electrophoresis is the mechanism by which a swimmer is propelled in response to a self-generated electric field (electric potential gradient). The velocity of the swimmer is generally proportional to its surface charge and the strength of the self-generated electric field, which is typically generated by asymmetric ion currents through its surface. Self-electrophoresis is the autonomous analogue of electrophoresis, which occurs when a charged particle migrates in a spatially uniform, externally applied electric field.

The surfaces of most organisms and particles are electrically charged. When a charged surface is brought into contact with an electrolyte solution, the surface attracts ions having the opposite charge from that of the surface (counterions) and repels ions having the same charge (coions). The ions form a diffuse screening layer known as the *Debye layer* or *diffuse layer* where counterions are locally enriched and coions are locally depleted. At equilibrium, the ions are arranged according to a balance between electrostatic attraction (which tends to attract counterions and attract coions to/from the surface) and thermal motion, which tends to spread the ions out. The charge on the surface is typically quantified by the *zeta potential*, defined as the potential of the surface relative to the bulk solution.

The characteristic thickness of the diffuse layer is given by the *Debye length* λ_D, which is defined as the length over which the electric potential decays from its value at the surface (the zeta potential, ζ) to ζe^{-1}. Assuming the Debye length is very small compared to the particle size, the speed of a particle undergoing conventional electrophoresis due to an applied electric field is given by the Helmholtz-Smoluchowski equation,

$$U = \frac{\varepsilon \zeta E}{\eta}. \tag{1.13}$$

Here ε is the permittivity of the solution, ζ is the zeta potential of the particle, E is the magnitude of the applied electric field, and η is the dynamic viscosity of the solution. Henry showed that for a diffuse layer of finite thickness, a normalized dimensionless correction factor, which is a function of the ratio of particle size to Debye thickness, should be multiplied by the right-hand side of (1.13) [42]. Several analyses of self-electrophoretic swimmers have predicted a form for the swimming speed that is proportional to (1.13), except that the electric field E is instead a characteristic electric field generated by the swimmer itself. The equation agrees with Golestanian's general scaling, equation (1.1), with the electric field replaced by $E = i/\sigma$, where i is the current density at the surface (called "surface activity" by Golestanian) and σ is the electrical conductivity of the solution. In the language of Golestanian's paper, the terms $\varepsilon\zeta/\eta$ constitute an effective phoretic mobility for the swimmer.

Models Prior to 2000: Biological Swimmers

In 1972, Mitchell revisited his earlier proposal [67] of self-electrophoretic locomotion of organisms and presented several possible realizations of the mechanism, as shown in Fig. 1.2 below [66]. Consider a bacterium which possesses a surface charge (usually negative), and is immersed in a fluid containing positive and negative ions. The surface will attract an excess of cations, which together with the surface will form an electrical double layer (EDL) surrounding the organism which is usually on the order of nanometers in thickness. Mitchell's mechanism suggests that through metabolic processes, the organism generates cations on one end of its body and consumes them on the other, producing a net flux of cations along its body, held close to the negatively charged surface by electrostatic attraction. These cations drag fluid with them as they move, causing propulsion of the organism in the opposite direction of the ion migration. At the same time, a cation current flows through the organism, completing the electrical circuit. Mitchell estimated that the electrical potential gradient required to drive the organism at 10 to 50 μm/s would be on the order of 10 V/cm, well within the capability of most microorganisms.

Mitchell's proposals followed years of research focusing on endogenous bioelectric fields, which provide directive force in cell morphogenesis. Spek hypothesized [92] and Lund & Jaffe showed [62] that asymmetric currents on the surface of a cell or embryo could generate electric fields that modify the shape of cells and tissues, as well as drive the transport of membrane-bound biomolecules. Many years later, Waterbury *et al.* [99] reported that a particular strain of marine cyanobacteria, *Synechococcus*, was able to swim at speeds up to 25 micrometers per second without flagella, suggesting that they move by a non-mechanical propulsion mechanism. In a 1989 review of colloid transport due to interfacial forces, Anderson [2] analyzed a cell that could generate asymmetric ion fluxes on its surface in the presence of a concentration gradient, similar to the cell proposed by Mitchell. If the current density flowing out of the cell depends

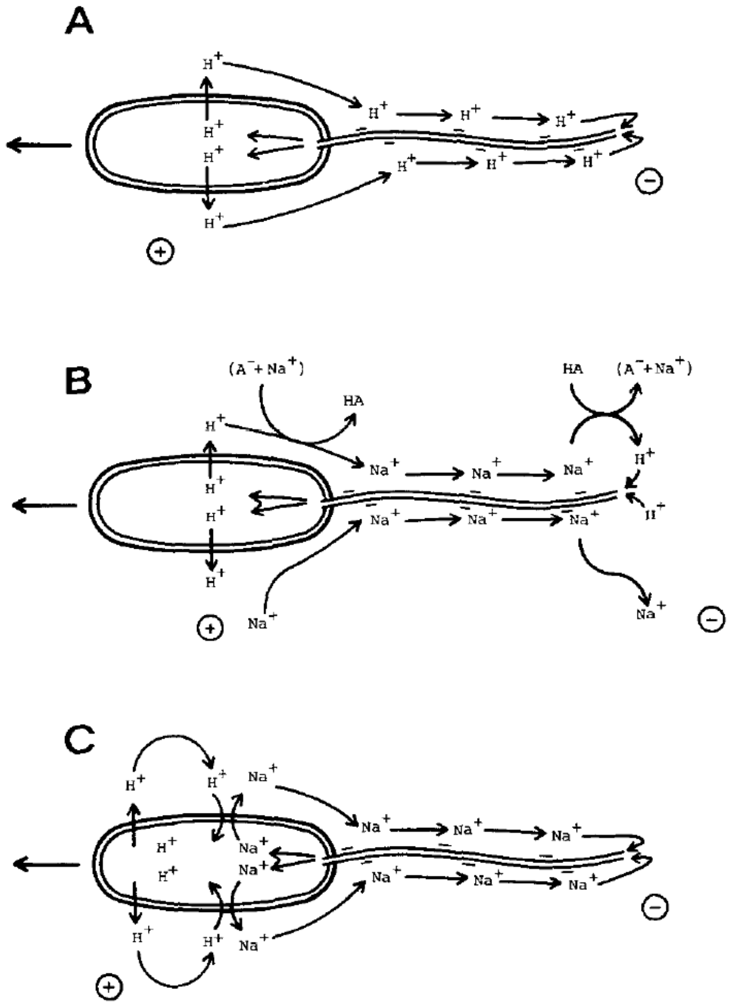

Figure 1.2: Possible mechanisms proposed by Mitchell [66] for electrophoretic locomotion of a bacterium. (A,B) Protons are released from the plasma membrane of the cell and migrate backwards toward the flagellum, which conducts protons back toward the body (a specific proton conductor). (C) In this case, the ion current is carried by Na^+ ions rather than protons, and the flagellum is a specific Na^+ conductor. In all cases, the ion migration induces a stream of water flowing from left to right, which is equivalent to motion of the bacterium from right to left. (Reprinted by permission of Federation of the European Biochemical Societies from "Self-electrophoretic locomotion in microorganisms: bacterial flagella as giant ionophores," by Peter Mitchell, *FEBS Letters*.)

on the concentration gradient according to $i = \chi \mathbf{n} \cdot \nabla C_\infty$, where χ is a constant proportional to the reaction rate, then Anderson's final expression for the particle velocity $\mathbf{U}$ is

$$\mathbf{U} = -\frac{1}{3}\frac{\varepsilon\zeta}{4\pi\eta}\frac{\chi}{\sigma}\nabla C_\infty. \tag{1.14}$$

Here, ∇C_∞ is the external concentration gradient, the terms $\varepsilon\zeta/4\pi\eta$ constitute an electrophoretic mobility, σ is the conductivity of the solution, and the term $\chi\nabla C_\infty/\sigma$ is an effective electric field generated by the cell. This equation thus shares some similarity with the Helmholtz-Smoluchowski equation and the equation derived by Golestanian *et al.* The major exception is that the latter formula does not require an externally applied concentration gradient. In deriving (1.14), Anderson apparently assumed that diffusiophoretic effects due to the external concentration gradient were negligible in comparison to the self-electrophoretic speed, $\mathbf{U}$.

Anderson also proposed that the self-electrophoresis mechanism originally proposed by Mitchell [67] and described by (1.14) may also apply to Waterbury's *Synechococcus* bacteria. Six years later, this hypothesis was rejected for cyanobacteria by Pitta and Berg [77]. They observed the motion of both *Synechococcus* and *E. coli* under an applied electric field in a saltwater medium, similar to the marine environments in which *Synechococcus* is naturally found. They did not observe any appreciable motion of the bacteria, and found that the electrophoretic mobility of *Synechococcus* is negligibly small in saltwater, indicating that self-electrophoresis is not the operative mechanism for these cyanobacteria. It has since been shown [76, 84] that synthetic particles which move by self-electrophoresis almost always slow down with increasing electrolyte concentration (but see [50]).

Lammert *et al.* [57] presented an analytical study of a cell which propels itself by a mechanism nearly identical to that proposed by Mitchell. The only major difference between their work and Mitchell's original scenario is geometric: instead of a bacterium, the swimmer is a simple spherical cell. Like most microorganisms, it is assumed to possess a negative surface charge. Through an unspecified mechanism, the sphere generates ion fluxes through its membrane that lead to a sinusoidal variation of electric potential (about the mean negative value) along its surface, such that the potential is most positive at the front of the cell and most negative at the back. The potential variation generates a dipolar electric field with a source at the front of the cell and a sink at the back. Due to the cell's negative surface charge, there is positive space charge in the diffuse layer surrounding the cell. Thus, the self-generated electric field exerts a body force on the positively charged fluid, setting the fluid and cell into motion with the front end forward. The authors derived a formula for the cell's swimming speed that is proportional to the familiar Helmholtz-Smoluchowski equation, which describes the speed of an electrophoretic particle when the interfacial diffuse layer is infinitely thin:

$$U = -\frac{\varepsilon \zeta E_0}{6\pi\eta}, \tag{1.15}$$

where ε is the permittivity of the solution, ζ is the cell's zeta potential, E_0 is a characteristic magnitude of the endogenous electric field, and η is the solution viscosity. Several other analyses of self-electrophoresis have obtained expressions for the swimming speed that are proportional to equation (1.15). In water, Lammert *et al.* estimate a propulsive speed on the order of 1-10 μm/s.

Models since 2000: Synthetic Swimmers

Studies of self-electrophoresis since the turn of the century reflect a conceptual shift in focus from understanding the motion of biological motors to fabricating, implementing, and modeling artificial self-propelled particles. As microfabrication techniques have become considerably more sophisticated, many variations of man-made self-electrophoretic microparticles have been demonstrated [75, 64, 10, 58, 19]. These experimentally realized systems have served as the inspiration for new theoretical models. Examples include the functionalized carbon fibers of Mano & Heller [64] and bimetallic rods reported by several groups [74]. Although most self-electrophoresis models now focus on artificial swimmers, the models vary considerably in the fuels, reactions, and particle materials used.

Mano & Heller [64] demonstrated the propulsion of a carbon fiber by reduction/oxidation reactions involving glucose and oxygen occurring on opposite sides of the fiber. The fiber moves by exchanging ions asymmetrically with the solution in much the same way as Mitchell's bacterium [67] or Lammert's cell [57]. As in the case of Mitchell's bacterium [66], a compensating current also flows through the body of the fiber in the direction opposite the ion current in the solution. Mano & Heller showed that when an insulator is placed between the ends of the fiber, disabling the current through the body, the self-propelled motion ceased, providing support for the self-electrophoretic mechanism. Propulsion due to electrochemical reactions has also been demonstrated with the decomposition of hydrogen peroxide. The peroxide undergoes two electrochemical half-reactions before finally yielding oxygen and water. Electrochemical peroxide decomposition has been reported to generate fluid flows around concentric electrodes [55] and in between interdigitated microelectrodes [76], as well as to propel microgears made from platinum and gold [12]. Finally, the most well-known examples of particles propelled self-electrophoretically by electrochemical reactions are likely the 2-micron bimetallic rods, which move autonomously in hydrogen peroxide.

1.2.3 Bimetallic Nanomotors

Bimetallic nanomotors can be considered the first experimental realizations (along with Mano & Heller's carbon fibers [64]) of the self-electrophoretic swimmers proposed by Mitchell and Lammert, although their motion was initially attributed to a different mechanism. They were first introduced to the scientific community by the research groups of Ayusman Sen and Thomas Mallouk at Pennsylvania State University in a 2004 paper by Paxton *et al.* [74]. Bimetallic nanomotors are generally cylindrical solid metallic particles, 2 microns in length and between 200-370 nanometers in diameter, and usually consist of a platinum (Pt) and a gold (Au) segment connected together. They are synthesized by sequentially electrodepositing Au and Pt into pores in an aluminum oxide (Al_2O_3) membrane, as described in detail by Martin *et al.* [65]. When immersed in 2-3 wt. % hydrogen peroxide, these particles exhibited self-propelled motion along their axis, with the Pt segment directed forward, at speeds of up to 10 body lengths per second.

Since their introduction, bimetallic nanorods have been engineered to swim at great speeds and perform a variety of microscale tasks. Laocharoensuk *et al.* [58] incorporated carbon nanotubes into the Pt segments of Pt/Au rods and added hydrazine (N_2H_4) to the peroxide solutions; these changes led to a dramatic increase in the observed swimming speed, in some cases exceeding 200 microns per second (100 body lengths per second). Kagan *et al.* [50] showed that, although the swimming speed decreases significantly when most electrolytes are added to the solution (as previously reported [76]), the addition of any electrolyte containing silver produces a roughly fivefold increase in swimming speed at a given H_2O_2 concentration. This increase was attributed to under-potential deposition of silver ions on the Au surface of the motors, which are then reduced in the presence of hydrogen peroxide. This leads to a faster effective reaction rate, increasing the surface activity discussed above, increasing the swimming speed.

External control over the speed and direction of the nanorods' motion is possible as well. A nanorod's velocity can be temporarily increased by applying heat pulses to the solution, which locally lower the viscosity and accelerate the reaction kinetics, both of which lead to an increased swimming speed [4]. One can accelerate or decelerate the motion by electrochemically modulating the local concentrations of hydrogen peroxide and molecular oxygen [11]. Directional control of the rods motion has been achieved by incorporating a small ferromagnetic segment, usually nickel (Ni), between the platinum and gold segments of the rod; the direction of motion is then controllable using external magnetic fields [10, 54]. The motors are capable of picking up, towing, and releasing micron-scale cargo, as shown by Burdick *et al.* [10] and Sundararajan *et al.* [96]. By observing the resultant drag forces when the motors tow cargo of different sizes, Burdick *et al.* calculated that the nanorods produce roughly 0.1 pN of force.

To explain the physical mechanism for the self-propulsion, Paxton *et al.* [74] proposed that the peroxide was being decomposed directly to water and oxygen on the platinum end of the rod, according to $H_2O_2 \rightarrow H_2O + 1/2\ O_2$. This oxygen generated on the platinum end remains dissolved in solution and spreads by diffusion along the gold end, generating a gradient in oxygen concentration. According to the theory, the dissolved oxygen disrupts hydrogen bonding of the water molecules, leading to a local decrease in interfacial tension. As a result, the concentration gradient in oxygen causes a gradient in interfacial tension to develop along the gold segment, driving a Marangoni flow from platinum to gold, resulting particle propulsion with the platinum end forward. Although this theory predicts a propulsive force of the appropriate magnitude, it does not predict the direction of motion and cannot explain certain phenomena that have since been observed with the rods, such as the dependence on solution conductivity. There is now a consensus that the interfacial tension gradient mechanism plays at best a minor role in the locomotion of the rods [98, 76].

Paxton *et al.* [75] proposed that a self-electrophoretic mechanism similar to those analyzed by Mitchell [66] and Lammert *et al.* [57] might apply to the rods. They proposed that, similar to Mano & Heller's carbon fibers [64], the nanorod acts like an electrochemical cell in short circuit, with Pt as the anode and Au as the cathode. On Pt, an oxidation reaction releases protons and molecular oxygen into the solution and liberates electrons into the metal:

$$H_2O_2 \rightarrow 2H^+ + 2e^- + O_2. \tag{1.16}$$

Driven by the difference in electron affinity between Au and Pt, the electrons conduct through the rod from Pt to Au. On the Au surface, a net peroxide reduction reaction combines peroxide, protons, and electrons to form water molecules:

$$H_2O_2 + 2H^+ + 2e^- \rightarrow 2H_2O. \tag{1.17}$$

The overall reaction is a decomposition of peroxide to oxygen and water, $2\ H_2O_2 \rightarrow 2\ H_2O + O_2$, as in the non-electrochemical decomposition scheme.

Experimental support for the electrochemical mechanism was provided the following year by Wang *et al.* [98], who predicted that the more negative metal (metal with lower electron affinity) should act as the anode in the electrochemical reaction scheme described above, and thus should be the metal directed forward when the rod moves. To determine the more negative metal, they measured the potential of zero net current (the mixed potential) for six noble metals (platinum, palladium, ruthenium, rhodium, gold, and nickel) in the presence of hydrogen peroxide. They then fabricated bimetallic rods composed of various combinations of the two metals. For any metal pair, the metal with the more positive mixed potential in peroxide was taken as the cathode and the other was taken as the anode. Since the anode should always be directed forward, one can therefore predict the direction of motion for a rod made from a given metal pair *a priori*, given their mixed potential values. These predictions were shown to be correct for all nine metal combinations studied, lending support to the electrochemical mechanism. The authors also fabricated a control nanorod consisting of a gold segment and a non-conductive polymer segment with a catalase coating that decomposes peroxide directly to oxygen and water, leading to oxygen evolution at a similar rate to that observed with Pt/Au rods. In other words, they fabricated a rod that is only capable of decomposing peroxide non-electrochemically. This rod did not move axially and showed only Brownian motion in hydrogen peroxide, again supporting the electrochemical mechanism.

Theoretical and experimental studies of similar electrochemical systems with different geometries also lend support to the self-electrophoresis mechanism for bimetallic nanorods. Building on their previous observations of catalytically induced fluid pumping between two concentric electrodes in peroxide [55], Kline *et al.* [56] described the system analytically using the Poisson, Nernst-Planck, and Helmholtz-Smoluchowski equations. They verified the accuracy of the model by predicting a form for the fluid velocity field, which allowed them to predict the radial location at which tracer particles would be deposited on the electrode surface. This prediction matched well with experimental measurements. Similarly, Paxton *et al.* [76] observed circulating fluid motion in between Pt and Au interdigitated microelectrodes (IMEs), as visualized using tracer particles. In the same study, they predicted an inverse relationship between speed and solution conductivity by combining the Helmholtz-Smoluchowski equation, Ohm's law, and the self-electrophoresis mechanism. Experimental measurements of rod speed as a function of solution conductivity bore out this prediction, further supporting the validity of the self-electrophoresis mechanism.

Although the self-electrophoresis mechanism is widely accepted to apply to bimetallic nanorods, the causal chain between the electrochemical reactions and the locomotion of the rod has yet to be established in rigorous, quantitative detail. If the rods are to be used in practical applications in nanotechnology and nanomedicine, a complete understanding of their capabilities (and limitations) is essential. This understanding would include the dependence of the motion on parameters of the system, such as the reaction rate on the particle surface, properties of the solution (including temperature, viscosity, and conductivity), fuel concentration, and surface properties.

Finally, a complete knowledge of the limitations on the rods' capabilities is crucial to attaining a complete understanding of their motion. The inverse dependence of the rods' speed on the solution conductivity is a potentially serious disadvantage if the rods are to be used in an electrically conductive system, such as the human body. We wish to understand fully if the conductivity-induced speed decrease is an inherent limitation to the propulsion mechanism, or if there is some way in which it may be overcome.

With their demonstrated capabilities for cargo-towing [10, 96], ultra-fast swimming motion [19, 58], chemical sensing [50], and externally guided motion [10, 11, 4], bimetallic nanorods have the potential to be widely applicable in nanotechnology. However, this applicability will be fundamentally hampered without a complete understanding of the origins, the capabilities, and the limitations of their self-propelled motion.

1.3 Scope and Outline of the Thesis

The questions to be answered in this thesis are:

1. Can the motion of the rods be modeled mathematically? What is the physical mechanism by which the electrochemical reactions lead to the motion of the rod?

2. How is the speed of the swimming affected by variations in system parameters, such as surface charge, reaction rate, peroxide concentration, solution viscosity, ion diffusivity, or solution conductivity?

3. What are the important limitations on the capabilities of bimetallic nanorods?

I choose to answer these questions by conducting simulations of a bimetallic nanorod in a hydrogen peroxide solution using finite-element software. In Chapter 2, I present a complete mathematical model including governing equations and boundary conditions, as well as a scaling analysis based on the governing equations which yields predictions of the dependence of the velocity on system parameters. Chapter 3 gives some details of the simulation algorithm. In Chapters 4 and 5, I show simulation results assuming both a charged and an uncharged particle surface, and using two separate models for the reaction kinetics. In Chapter 6, I apply the model developed in the previous chapters to understand physically why the rods move more slowly in conductive media. Finally, Chapter 7 concludes with some reflections on the successes and failures of this thesis, and offers some suggestions for future research.

Chapter 2

THEORETICAL FORMULATION

2.1 Introduction

In this chapter, we develop a general mathematical model for electrokinetic locomotion. The model is based on the Poisson-Nernst-Planck-Stokes system of equations, which are widely used to describe electrokinetic systems. Special attention is devoted to the boundary conditions, which describe the interfacial phenomena that ultimately lead to rod locomotion. The electrochemical reactions occurring on the rod's surface are modeled using Frumkin-corrected Butler-Volmer kinetics, reflecting the interdependence of the internal electric potential of the rod and the electrochemical reaction rates. To our knowledge, this model is the first to acknowledge and account for the existence of this coupling.

2.2 Description of the Problem

We consider a cylindrical particle, 2 microns in length and 300 nanometers in diameter, immersed in an infinite aqueous solution containing hydrogen peroxide (H_2O_2) and dissolved molecular oxygen (O_2). The solution may also contain dissolved carbon dioxide (CO_2) in equilibrium with carbonic acid (H_2CO_3) and/or a non-reactive background electrolyte. Due to the particle geometry, we use a cylindrical polar coordinate system, denoting locations in the simulation domain with the position vector $\mathbf{r} = (r, \theta, z)$.

The aqueous solvent self-ionizes into hydrogen cations (H^+) and hydroxide anions (OH^-) with a dissociation constant of $pK_w = 14$. If only H^+ and OH^- are present, electroneutrality requires that the concentrations of H^+ and OH^- be equal, thus resulting in a pH of 7. In the initial simulations (Chapters 4 and 5), in which protons and hydroxide ions are the only charged species present, the background concentrations of both H^+ and OH^- are set to 10^{-7} mol/L. In subsequent cases (Chapter 6), other charged species are accounted for, and so the equilibrium concentrations of H^+ and OH^- must be computed through acid/base equilibrium relations.

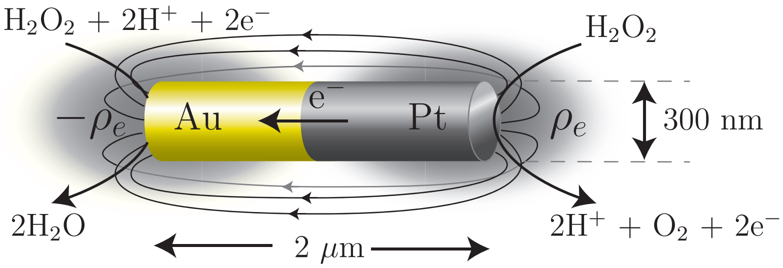

Figure 2.1: Schematic of Pt/Au nanomotor in hydrogen peroxide solution showing typical dimensions, electrochemical reactions, approximate charge density distribution, and approximate electric field lines. As shown here, the rod's motion is directed to the right.

Although hydrogen peroxide and molecular oxygen do not contribute to the charge density and electric fields which are ultimately responsible for the locomotion of the rods, they participate in the electrochemical reactions, and so we track their concentration distributions as well. We find that the peroxide concentration (on the order of 1 mol/L) is perturbed from its bulk value by less than 1 % by the reactions. This suggests that it would be an acceptable approximation to consider the peroxide concentration constant. For completeness, we present here the governing equations and boundary conditions for all species in the system.

Figure 2.1 shows a schematic of a platinum/gold nanorod in a hydrogen peroxide solution.[1] When the rod is immersed in peroxide, catalytic electrochemical reactions occur spontaneously on its surface. On the platinum (Pt) surface, an oxidation reaction decomposes peroxide into protons, electrons, and oxygen molecules. The oxidation reaction results in a local depletion of peroxide and abundance of protons and oxygen. Here, we assume that the concentration of oxygen is below the saturation limit (this assumption is well-justified for peroxide concentrations under approximately 10 wt. %) and thus the nucleation of oxygen bubbles is not considered.

---

[1] Throughout this thesis, we use the terms "nanomotor," "nanorod," and "rod" interchangeably to describe the bimetallic rod-shaped particle in Fig. 2.1.

This assumption is consistent with our experiments conducted with Pt/Au rods in low to moderate (1-6 wt. %) peroxide concentrations. The electrons conduct through the rod from platinum to the gold (Au) side. On the Au surface, a net peroxide reduction reaction combines protons, electrons and peroxide to form water molecules. Although it is possible that the reduction of molecular oxygen may also occur to some extent on the gold surface, as proposed by Wang *et al.* [98], this reaction must not be essential in driving the motion of the rod, since our previous work shows that the rods' motion still occurs in solutions that have been purged of oxygen and that oxygen-rich environments slow the motors (see [11]). At the Au end there is a net depletion of protons and peroxide. Overall, the rod behaves as a short-circuited galvanic cell which generates protons at the platinum anode and consumes protons at the gold cathode.

The rods also share similarities with bipolar electrodes, single electrodes on which reduction and oxidation are occurring simultaneously on opposite ends of the electrode. These electrodes have been studied in several recent works. Duval *et al.* [26, 27] analyzed Faradaic depolarization processes occurring on a metal surface in an externally applied electric field tangential to the metal surface. The imposed field caused a gradient in interfacial potential difference along the metal surface, leading to a spatially varying Faradaic current such that oxidation was occurring on one end and reduction on the other, similar to the case of bimetallic nanomotors. These systems were later investigated further using numerical models taking the reversibility of the Faradaic reactions into account (see [25, 28]. Dhopeshwarkar *et al.* [21], Laws *et al.* [60] and Hlushkou *et al.* [43] studied a bipolar electrode in a PDMS microchannel under an applied electric field. They generally found that the presence of the electrode, and the Faradaic reactions occurring on it, caused local non-uniformities in the electric field which could be used to locally enrich the concentration of an analyte.

Here, we provide a model that shows that locomotion is driven by fluid slip caused by self-generated electrical body forces. The excess and depletion of protons at the anode and cathode generate an electric field, denoted by $\mathbf{E}$. Electrical body forces, of the form $\rho_e\mathbf{E}$, are exerted by the tangential electric field, which points from the anode to the cathode (see Fig. 2.1) on free space charge in the solution, with volumetric density ρ_e. The space charge ultimately arises from two sources: the asymmetry in cation concentration induced by the reactions, and the net charge in the diffuse screening layer of ions surrounding the motor, which forms to screen the surface charge. The electrical body forces drive fluid motion and thus rod motion. Ultimately, locomotion of the rods is driven by a coupling of the net charge in the diffuse layer and the electric fields generated by the asymmetric distribution of reaction products established by the surface reactions. This mechanism combines effects of concentration gradients of charged species and electrical potential gradients, sharing similarities with an autonomous form of electro-diffusiophoresis, as studied by Rica and Bazant [82].

In the next section, we present the governing equations, all of which are valid assuming the simulation domain is a continuum and that all species are present in dilute amounts.

2.3 Governing equations

2.3.1 Species Transport

The concentration distributions of ionic and non-ionic species in solution are described by the conservation law,

$$\frac{\partial C_i}{\partial t} = -\nabla \cdot \mathbf{j}_i, \tag{2.1}$$

where C_i and $\mathbf{j}_i$ are the concentration and flux of species i. Here we consider fluxes due to convection (or advection), which arises due to bulk fluid motion, and migration, which occurs due to gradients in chemical potential:

$$\mathbf{j} = \mathbf{j}_{adv} + \mathbf{j}_{mig}. \tag{2.2}$$

The advective flux of species i is given by the product of the local concentration of i and the local fluid velocity, $\mathbf{u}$:

$$\mathbf{j}_{i,adv} = C_i \mathbf{u}. \tag{2.3}$$

For highly concentrated solutions, the migration flux may depend on interactions among species. In our case, the species concentrations never exceed the millimolar range (with the exception of hydrogen peroxide[2]), and so we make the common assumption in electrokinetics of a *dilute solution*; that is, we assume that the concentrations of all solutes are much smaller than that of the solvent and interactions among species are negligible. In this limit, the migration flux of species i is given by [14]

$$\mathbf{j}_{i,mig} = -\nu_i C_i \nabla \mu_i \tag{2.4}$$

where ν_i is the mobility of species i in the solution, having units of (s·mol)/kg, and μ_i is the *electrochemical potential* of species i. For dilute solutions, the electrochemical potential includes contributions due to diffusion and electromigration [14]:

$$\mu_i = RT \ln C_i + z_i F \phi \tag{2.5}$$

Here R is the universal gas constant, T is the absolute temperature, z_i is the valence of species i, F is Faraday's constant, and ϕ is the electrostatic potential. As noted by Chu and by Newman, the electrostatic potential is a well-defined quantity independent of any choice of a reference ionic species *only* in the dilute solution limit [14, 70].

Insertion of (2.5) into (2.4) gives the generalized migration flux expression for species i:

$$\mathbf{j}_{i,mig} = -(D_i \nabla C_i + z_i F \nu_i C_i \nabla \phi) \tag{2.6}$$

where we have made use of the Nernst-Einstein relation $D_i = \nu_i RT$ to relate the mobility to the diffusion coefficient D_i. Substituting (2.6) for the flux term in (2.1)

---

[2] The concentration of peroxide is allowed to be as high as 1.5 mol/L. This is still relatively small compared to the concentration of the aqueous solvent, which is 55 mol/L.

and making use of the linearity of the divergence operator, the conservation law becomes

$$\frac{\partial C_i}{\partial t} = -\nabla \cdot (C_i \mathbf{u}) + \nabla \cdot (D_i \nabla C_i + z_i F \nu_i C_i \nabla \phi). \tag{2.7}$$

In all simulations performed in this work, the system reaches steady state. Therefore the left-hand side of (2.7) is zero. Also, the first term on the right-hand side, the divergence of the convective flux, may be rewritten using the product rule as $\nabla \cdot (C_i \mathbf{u}) = \mathbf{u} \cdot \nabla C_i + C_i \nabla \cdot \mathbf{u}$. Here, the flow is incompressible, and so mass conservation requires that the velocity field be divergence free (see (2.12) below). Therefore, $\nabla \cdot \mathbf{u} = 0$, and only the first term in the product rule expansion remains. Implementing these changes, the conservation law becomes

$$\mathbf{u} \cdot \nabla C_i = \nabla \cdot (D_i \nabla C_i + z_i F \nu_i C_i \nabla \phi). \tag{2.8}$$

This equation, which is often referred to as the *Nernst-Planck equation* or the *advection-diffusion equation*, governs the concentration distributions for ionic and non-ionic species. For non-ionic species, the electromigration term (second term on the right-hand side of (2.8)) is omitted.

In the initial simulations presented in this thesis, the fluid medium includes H^+ cations and OH^- anions. In later cases, we consider a four-ion system including a nonreactive electrolyte, along with H^+ and HCO_3^- anions (the latter of which accounts for the presence of carbonic acid due to dissolved carbon dioxide). In principle, the model is capable of accounting for an arbitrary amount of ionic species.

2.3.2 Poisson's equation

At any point where the concentrations of cations and anions are unequal, the fluid element at that location carries a net electrical charge. The volumetric density of that charge is defined in terms of the ion concentrations as

$$\rho_e = F \sum_i z_i C_i. \tag{2.9}$$

Gauss's law relates the electric charge to the electric field at a particular location:

$$\nabla \cdot \varepsilon \mathbf{E} = \rho_e. \tag{2.10}$$

Here $\mathbf{E} \equiv -\nabla\phi$ is the electric field, the negative of the potential gradient, and ε is the permittivity of the solution. The permittivity may be written as the product of the vacuum permittivity ε_0 and relative permittivity ε_r, the latter of which we have taken to be constant.[3] Substituting the definition of electric field and applying the assumption of constant permittivity, (2.10) becomes, after some rearrangement,

$$\nabla^2\phi = -\frac{\rho_e}{\varepsilon_0\varepsilon_r}. \tag{2.11}$$

Equation (2.11) is known as *Poisson's equation* and relates the electric potential to the local ion concentrations.

2.3.3 Fluid flow equations

The fluid is assumed incompressible, and thus mass conservation requires that the velocity field be divergence-free:

$$\nabla \cdot \mathbf{u} = 0, \tag{2.12}$$

At any point in the domain where the charge density ρ_e and electric field $\mathbf{E}$ are both nonzero, a net electrical body force with magnitude $|\rho_e\mathbf{E}|$ is exerted by the field on the fluid element at that point in space. This body force is represented mathematically as a forcing term in the Stokes equations, which give the velocity field and pressure distributions,

$$\eta\nabla^2\mathbf{u} - \nabla p = \rho_e\nabla\phi. \tag{2.13}$$

Here η is the dynamic viscosity of the solvent, p is the pressure and $\rho_e\nabla\phi$ is the electrical body force. We ignore the inertial terms which are present in the full

---

[3] This assumption may be somewhat inaccurate near the rod surface. The electric fields very close to the surface are very strong, polarizing the solvent molecules, which can decrease the permittivity by approximately an order of magnitude. Here, we ignore this effect and assume the permittivity to be a constant.

Navier-Stokes equations, since we expect the Reynolds number of this flow to be very small due to the small particle size and slow swimming speeds.

Equations (2.8), (2.11), (2.12), and (2.13) are commonly referred to as the Poisson-Nernst-Planck-Stokes equations. This mathematical framework has been used to describe classical electrokinetic phenomena, such as electrophoresis [42] and more recently electrokinetic instabilities in microchannels [79, 69].

2.4 Boundary Conditions

2.4.1 Far from the surface of the rod

The simulations in this work are performed in the reference frame of the rod. From the perspective of the rod, the background fluid moves "backwards" (opposite the direction of swimming) at a speed that is equal to the rod's swimming speed. This swimming speed is unknown *a priori* and must be determined based on the concentration, electric field, and velocity field distributions. To allow the velocity far from the surface of the rod to be undetermined initially, we enforce a no-viscous stress condition on the outer boundary, expressed mathematically as

$$\eta\left[\nabla\mathbf{u}+(\nabla\mathbf{u})^T\right]\rightarrow 0 \text{ as } |\mathbf{r}|\rightarrow\infty, \tag{2.14}$$

where $\nabla\mathbf{u}$ is the velocity gradient tensor and the superscript T denotes the transpose. This boundary condition effectively imposes a slip condition the outer edge of the simulation domain, simulating a semi-infinite medium.

As distance from the rod approaches infinity, the concentrations of all species approach their bulk values,

$$C_i\rightarrow C_{i,\infty} \text{ as } |\mathbf{r}|\rightarrow\infty. \tag{2.15}$$

All electric potentials in the system are defined relative to the bulk solution. Thus, far from the rod, the electric potential decays to zero,

$$\phi\rightarrow 0 \text{ as } |\mathbf{r}|\rightarrow\infty. \tag{2.16}$$

In the simulations, (2.14)-(2.16) are applied at the boundary of the simulation domain opposite the rod, which is nearly 50 rod lengths from the surface. This distance was chosen so that the values of the field variables would be close to their values at an infinite distance from the rod. See Chapter 3 for further details on how the domain size was selected.

2.4.2 Surface of the rod: fluid flow

The familiar no-slip condition is applied on the surface of the rod. In the rod's reference frame, the rod is stationary and fluid flows around it. Thus, the fluid that adheres to the rod is also stationary:

$$\mathbf{u} = \mathbf{0}. \tag{2.17}$$

We apply (2.17) at the outer edge of the compact layer, which is the effective surface of the rod in the simulation domain.

2.4.3 Surface of the rod: electric potential

Figure 2.2 shows a schematic of the rod/solution interface and qualitatively depicts the variation in electric potential near the interface. We use the Gouy-Chapman-Stern model of the interface, which includes two distinct layers: a compact or *Stern layer* of adsorbed neutral and charged species, and a *diffuse layer* of solvated ions, free to move in solution, whose distribution is determined by a balance of electrostatic forces, which repel coions from and attract counterions to the surface, and diffusion, which tends to spread the ions out. The Stern and diffuse layers together constitute the *electrical double layer* (EDL). The ions and molecules making up the Stern layer are assumed to move with the particle. Thus, the simulation domain includes the diffuse layer but *not* the Stern layer. The outer edge of the Stern layer is often called the outer Helmholtz plane (OHP). It is assumed to be the point of closest approach for species in solution. For the flow problem, the outer edge of the Stern layer (the OHP)

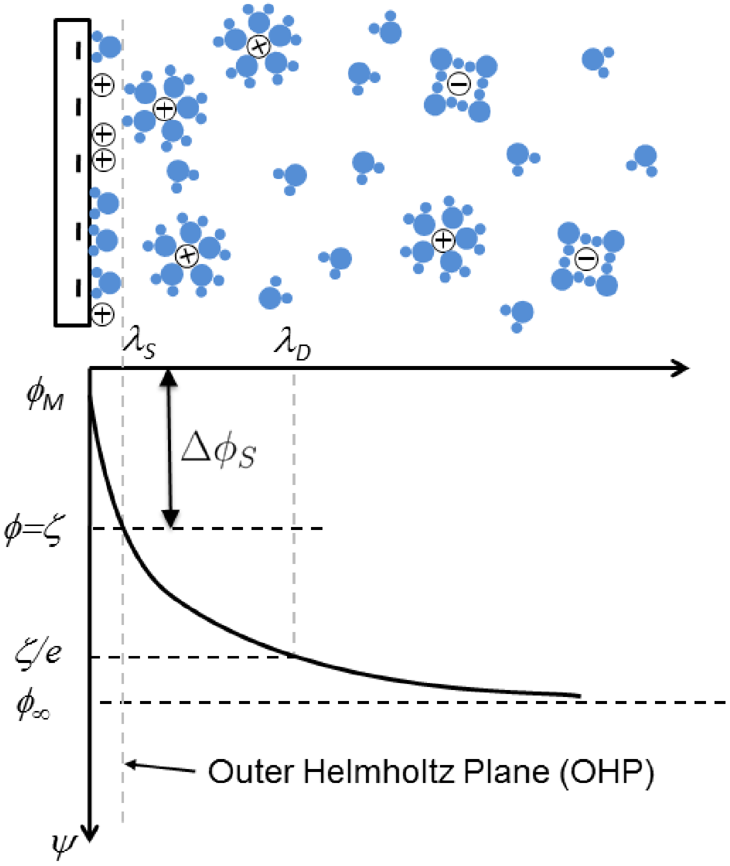

Figure 2.2: Schematic of the rod/solution interface, showing the Stern layer (with effective thickness λ_S) and the diffuse layer (with characteristic thickness λ_D, defined in (2.21)). The outer Helmholtz plane (OHP) is located at the outer edge of the Stern layer. We define the zeta potential ζ as the potential at the OHP with respect to the potential in the bulk solution, denoted here by ϕ_∞. In the simulations, we set $\phi_\infty = 0$. The potential profile within the Stern layer is linear, with slope equal to the potential gradient at the OHP.

is the effective surface of the rod. The Stern layer affects the system by altering the electric field at the rod surface, which is reflected in the boundary conditions for the electric potential and electrochemical reactions.

In this work, we follow Bard and Faulkner [5] and Bazant *et al.* [6] in assuming that the potential profile in the Stern layer is a linear extrapolation of the potential gradient at the reaction plane. This is expressed mathematically by a mixed Dirichlet/Neumann boundary condition on the potential, which is applied *at the outer Helmholtz plane*, which is the effective surface of the rod in the simulation domain:

$$\phi_M + \lambda_S \left(\mathbf{n} \cdot \nabla \phi\right)_{OHP} = \zeta, \tag{2.18}$$

where $\mathbf{n}$ is the unit normal vector pointing outward from the rod surface into the solution, ϕ_M is the electric potential of the rod interior relative to the bulk solution, λ_S is an effective thickness of the Stern layer (on the order of 1-10 Å), ζ is the zeta potential (*i.e.*, the potential at the OHP with respect to the bulk solution), and the subscript OHP indicates that the quantity is evaluated at the outer Helmholtz plane. Since the rod is conducting, we assume the internal potential ϕ_M to be uniform in the interior. The zeta potential is defined as the potential at the slip plane, where the no-slip condition is applied. Here, we apply the no-slip condition at the OHP, and thus assume that the slip plane and OHP are one and the same. Since the normal potential gradient at the OHP is not uniform in general, the zeta potential generally varies with position along the rod surface.

Figure 2.2 also visualizes $\Delta\phi_S$, the potential drop across the Stern layer, which will prove important in determining the rates of the reactions, and is defined here as

$$\Delta\phi_S \equiv \phi_M - \zeta = \lambda_S \left(\mathbf{n} \cdot \nabla \phi\right)_{OHP}. \tag{2.19}$$

To understand how the Stern voltage varies with system parameters, we can estimate its value from the Debye-Hückel solution for the electric field near a charged flat plate.

The potential distribution as a function of distance y normal to the plate is given by

$$\phi(y) = \zeta_p \exp\left(-\frac{y}{\lambda_D}\right), \tag{2.20}$$

where ζ_p is the zeta potential of the plate and the Debye thickness λ_D is given for a symmetric $z:z$ electrolyte by

$$\lambda_D \equiv \sqrt{\frac{\varepsilon_0 \varepsilon_r RT}{2z^2F^2C_{\pm,\infty}}}. \tag{2.21}$$

Differentiating (2.20) with respect to y and evaluating at $y = 0$, the normal potential gradient at the surface is given by

$$\frac{\mathrm{d}\phi}{\mathrm{d}y} = -\frac{\zeta_p}{\lambda_D}. \tag{2.22}$$

Insertion of the flat plate result (2.22) for the surface potential gradient into (2.19) and some rearranging gives the scaling relation

$$|\Delta\phi_S| \propto \frac{\lambda_S}{\lambda_D}|\zeta|. \tag{2.23}$$

For the rods, the zeta potential scales with the internal potential ϕ_M. Thus for the rods, we would expect

$$\left|\frac{\Delta\phi_S}{\phi_M}\right| \propto \frac{\lambda_S}{\lambda_D}. \tag{2.24}$$

Equation (2.24) implies that the relative importance of the Stern voltage compared to the rod potential is linearly related to the ratio of the Stern layer thickness to the Debye thickness. In this work, the Stern layer thickness is fixed at 2 Å, while the Debye thickness depends on the background ion concentration.

2.4.4 Surface of the rod: species transport

Flux of species at the surface

Since they do not participate in the electrochemical reactions, the flux of anions is set to zero at the surface,

$$\mathbf{n} \cdot (-D_- \nabla C_- - z_- F \nu_- C_- \nabla\phi + C_- \mathbf{u}) = 0. \tag{2.25}$$

Equation (2.25) also applies to any other species in the system that does not react, e.g. a background electrolyte, and enforces a balance of fluxes due to diffusion, electromigration, and convection. The boundary condition for protons represents their generation and consumption due to the electrochemical reactions, according to

$$\mathbf{n} \cdot (-D_+ \nabla C_+ - z_+ F \nu_+ C_+ \nabla \phi + C_+ \mathbf{u}) = \begin{cases} j_{anode} \\ j_{cathode}, \end{cases} \tag{2.26}$$

where j_{anode} and $j_{cathode}$ are the reaction-driven proton fluxes on the anode and cathode surfaces, respectively. The flux boundary conditions for peroxide and oxygen reflect the stoichiometry of the reactions. For every peroxide molecule that is consumed on the anode segment, two protons and one oxygen molecule are released into the solution. Thus on the anode, the appropriate boundary conditions for peroxide and oxygen are, respectively,

$$\mathbf{n} \cdot (-D_{H_2O_2} \nabla C_{H_2O_2} + C_{H_2O_2} \mathbf{u}) = -\frac{j_{anode}}{2}, \tag{2.27}$$

$$\mathbf{n} \cdot (-D_{O_2} \nabla C_{O_2} + C_{O_2} \mathbf{u}) = \frac{j_{anode}}{2}. \tag{2.28}$$

For every peroxide molecule consumed on the cathode surface, two protons are consumed. Here we assume that no reactions involving oxygen occur on the cathode surface. Wang *et al.* [98] suggested that the four-electron reduction of oxygen also occurs on the cathode, in addition to peroxide reduction. However, this reaction must not be essential to the motion of the rods, since it was later shown by Calvo-Marzal *et al.* [11] that the rods move faster in solutions that have been purged of oxygen, while at the same time oxygen-rich environments slow the rods' motion. Thus, here we ignore the possibility of oxygen reduction and assume oxygen is nonreactive on the cathode. The boundary conditions for peroxide and oxygen on the cathode are thus

$$\mathbf{n} \cdot (-D_{H_2O_2} \nabla C_{H_2O_2} + C_{H_2O_2} \mathbf{u}) = \frac{j_{cathode}}{2}, \tag{2.29}$$

$$\mathbf{n} \cdot (-D_{O_2} \nabla C_{O_2} + C_{O_2} \mathbf{u}) = 0. \tag{2.30}$$

The surface fluxes of neutral species are coupled to the surface flux of protons, which we have yet to define. The amount of protons released or consumed on the rod surface depends on the reaction rates, which are a function of the local species concentrations, internal rod potential, and kinetic properties of the peroxide reduction and oxidation reactions. To derive expressions for the reaction rates, we make use of the Butler-Volmer model of electrochemical kinetics. In what follows, we give a brief overview of the fundamentals of Butler-Volmer theory, and then adapt the standard model to the problem at hand. For further details on Butler-Volmer kinetics, the interested reader is referred to Bard and Faulkner [5], Delahay [18], and Newman [70].

The Butler-Volmer equation and Frumkin's correction

Consider the general n-electron reduction of species O, having valence z, to form species R, having valence $(z - n)$:

$$\mathrm{O}^{z} + ne^{-} \rightleftharpoons \mathrm{R}^{z-n}. \tag{2.31}$$

The Butler-Volmer equation gives the net current density i crossing the electrode surface associated with this reaction as a function of the electrode potential. For a one-dimensional system, with the electrode surface located at $x = 0$, the equation is given in [5] as:

$$i = i_0 \left[\frac{C_O(0,t)}{C_O^\infty} e^{-\alpha n f(\phi_M - \phi_M^{eq})} - \frac{C_R(0,t)}{C_R^\infty} e^{(1-\alpha) n f(\phi_M - \phi_M^{eq})} \right] \tag{2.32}$$

where i_0 is the exchange current density, $C_O(0,t)$ and $C_R(0,t)$ are the concentrations of O and R evaluated at the electrode surface (C_O^∞ and C_R^∞ are the bulk concentrations of the indicated species), α is a unitless parameter between 0 and 1 that quantifies the symmetry of the activation barrier for the reaction, $f = F/RT$ is the inverse thermal voltage, ϕ_M is the potential of the metal electrode interior with respect to the bulk solution, and ϕ_M^{eq} is the metal potential at equilibrium, *i.e.* in the absence of net current. The difference $\phi_M - \phi_M^{eq}$ is termed the *overpotential*, commonly written η.

Frumkin's key contribution [35] was to recognize that the potential drop across the diffuse layer implies that the potential at the reaction plane is different from the potential in the bulk solution. Since species O can penetrate the diffuse layer, when it gets close enough to the electrode to participate in the reaction, the potential it experiences is not the same as the potential in the bulk. This potential difference can affect the reaction rates in two ways [5]:

1. In general, if $z \neq 0$ and the electrode surface carries a net charge, the concentrations of O, R, or both at the surface of the electrode will be different from their bulk values. Let us assume that the ions follow a Boltzmann distribution[4], giving $C_O(x_2, t) = C_O^\infty e^{-zf\phi_2}$ and $C_R(x_2, t) = C_R^\infty e^{-(z-n)f\phi_2}$. Since O and R can come no closer to the electrode than the reaction plane, the concentrations are now evaluated *at* the reaction plane, denoted by x_2.

2. The potential difference driving the electrode reaction (2.31) is not $\phi_M - \phi_S$ (with ϕ_S as the potential of the bulk solution), but $\phi_M - \phi_2 - \phi_S$, where ϕ_2 is the potential at the reaction plane.

Let us now apply these two principles to equation (2.32). The equation is now expressed in terms of a true exchange current density, i_0^t. Some rearrangement yields

$$i = i_0^t e^{(\alpha n - z)f\phi_2} \left[e^{-\alpha n f(\phi_M - \phi_M^{eq})} - e^{(1-\alpha)nf(\phi_M - \phi_M^{eq})} \right]. \tag{2.33}$$

Equation (2.33), in which the term $e^{(\alpha n - z)f\phi_2}$ is sometimes called the *Frumkin correction*, is the same formulation of the equation given by Delahay [18] (see p. 158) and by Biesheuvel *et al.* [9] (their equation (7)). Stating the equation in this form makes clear the effect of the double layer on the kinetics: the apparent value of exchange current density, i_0, in (2.32) is actually a function of potential, since ϕ_2 varies

---

[4] This assumption is not necessarily valid in the case of bimetallic nanorods, and will be removed for the case of nanorods below.

with potential [5]. The true exchange current density i_0^t is constant with respect to potential.

Derivation of the Frumkin-Butler-Volmer equation used here

Equation (2.33) is not ideally formulated to describe the reactions occurring on the surface of a bimetallic nanorod. We wish to express this equation in a form that highlights the dependence of the reaction rate on the voltage across the Stern layer, $\Delta\phi_S$. Also, in general, since the ions are actively being generated and consumed on the particle surface, they will not necessarily follow a Boltzmann distribution. We thus also wish to remove the Boltzmann assumption in (2.33). Following Biesheuvel *et al.* [9], we make the following substitutions:

- Define the *Stern voltage* $\Delta\phi_S \equiv \phi_M - \phi_2$
- Replace $\exp(-zf\phi_2)$ by $C_O(x_2)/C_O^\infty$. This replacement removes the Boltzmann assumption for species O and is the most general formulation.
- Similarly, remove the Boltzmann assumption for R and replace $\exp(-(z-n)f\phi_2)$ with $C_R(x_2)/C_R^\infty$.

With these changes, equation (2.33) becomes

$$i = i_0^t \left[\frac{C_O(x_2,t)}{C_O^\infty} e^{-\alpha n f(\Delta\phi_S - \phi_M^{eq})} - \frac{C_R(x_2,t)}{C_R^\infty} e^{(1-\alpha)nf(\Delta\phi_S - \phi_M^{eq})} \right]. \tag{2.34}$$

(2.34) can be simplified further by combining groups of constants together in the following way. Let

$$K_R = \frac{i_0^t e^{\alpha n f \phi_M^{eq}}}{C_O^\infty}, \tag{2.35}$$

$$K_O = \frac{i_0^t e^{-(1-\alpha) n f \phi_M^{eq}}}{C_R^\infty}, \tag{2.36}$$

Here K_R and K_O are *effective rate constants* for the cathodic and anodic components of the reaction (2.31). Substituting (2.35) and (2.36) into (2.34),

$$i = K_R C_O(x_2, t) \exp\left(\frac{-\alpha n F \Delta\phi_S}{RT}\right) - K_O C_R(x_2, t) \exp\left(\frac{(1-\alpha) n F \Delta\phi_S}{RT}\right). \tag{2.37}$$

This version of the Frumkin-Butler-Volmer equation has been widely used recently in studies of transport phenomena near electrodes, e.g. [6, 9]. In this work, we use a very similar expression to (2.37) to describe the reaction-driven proton fluxes on the rod surface. To obtain our kinetic equations, we divide (2.37) by F (applying *Faraday's Law of Electrolysis*), giving an expression instead for the flux of protons (in mol/m^2·s).

For reactions with multiple reactants, such as the peroxide reduction reaction on the cathode, C_O and C_R are written as products of the concentrations of individual reactants raised to the power of their respective stoichiometric coefficients:

$$C_O = \prod_i^{N_c} C_{iO}^{s_{iO}}, \tag{2.38}$$

$$C_R = \prod_i^{N_a} C_{iR}^{s_{iR}}, \tag{2.39}$$

where C_{iO} and C_{iR} are respectively the concentrations of reactant species i for the cathodic and anodic reactions, the exponents s_{iO} and s_{iR} are the stoichiometric coefficients, and the products are taken over the N_c and N_a reactant species for the cathodic and anodic reactions.

K_R and K_O

K_R and K_O are effective rate constants for the cathodic and anodic components of the reaction (2.31), respectively. In this thesis, we choose appropriate values for K_R and K_O to yield realistic swimming velocities. Despite the dependence on background reactant concentration and equilibrium potential indicated in (2.35) and (2.36), we assume that K_R and K_O are constant throughout the range of peroxide and salt concentrations studied throughout this work.

Rate equations for H_2O_2 oxidation and reduction

For the peroxide oxidation reaction on the anode, equation (2.37) is written

$$j_{anode} = K_{O,anode} C_{H_2O_2} e^{(1-\alpha)nf\Delta\phi_S} - K_{R,anode} C_{O_2} C_+^2 e^{-\alpha nf\Delta\phi_S}, \tag{2.40}$$

and for peroxide reduction on the cathode,

$$j_{cathode} = K_{O,cathode} C_{H_2O}^2 e^{(1-\alpha)nf\Delta\phi_S} - K_{R,cathode} C_{H_2O_2} C_+^2 e^{-\alpha\Delta\phi_S}. \tag{2.41}$$

Here, for convenience, we use the sign convention that an oxidative proton flux (protons *leaving* the rod surface) is positive and a reductive proton flux (protons *entering* the rod surface) is negative. This is the opposite of the convention employed in (2.37) above.

We simplify these equations by assuming that the reactions proceed in the forward direction only. This is equivalent to assuming that the reactions are in the Tafel regime, or that they are electrochemically irreversible. We consider only the oxidation of peroxide on the anode and reduction of peroxide on the cathode, leaving

$$j_{anode} = K_{O,anode} C_{H_2O_2} e^{(1-\alpha)nf\Delta\phi_S}, \tag{2.42}$$

$$j_{cathode} = -K_{R,cathode} C_{H_2O_2} C_+^2 e^{-\alpha nf\Delta\phi_S}. \tag{2.43}$$

The Tafel approximation is applied primarily for simplicity. However, it is unlikely that the reverse components of the reactions would be significant if they were included. The reverse reactions on the anode and cathode are, respectively, two-electron reduction of molecular oxygen and two-electron oxidation of water, both of which produce hydrogen peroxide. It is possible that some oxygen is being reduced on the anode, especially if the anode metal is platinum, which is a good catalyst for oxygen reduction. It is unlikely that much oxygen is being reduced, however, given the trace amounts of oxygen present in the system and the relatively small amount of oxygen produced by peroxide oxidation on the anode.

It is also unlikely that water is being oxidized to a significant extent on the cathode because this reaction requires a significant overpotential on the cathode in favor of oxidation. Here, the entire rod attains a uniform potential such that the overpotential bias on the anode favors oxidation and the bias on the cathode favors reduction. Thus, we are effectively assuming that

$$\frac{k_{O,anode} C_{H_2O_2} e^{(1-\alpha)nf\Delta\phi_S}}{k_{R,anode} C_+^2 C_{O_2} e^{-\alpha nf\Delta\phi_S}} \gg 1 \tag{2.44}$$

due to the low concentration of O_2, and

$$\frac{k_{R,cathode} C_{H_2O_2} C_+^2 e^{-\alpha nf\Delta\phi_S}}{k_{O,cathode} C_{H_2O}^2 e^{(1-\alpha)nf\Delta\phi_S}} \gg 1 \tag{2.45}$$

due to the low value of $k_{O,cathode}$, which depends indirectly on overpotential.

2.4.5 Conservation of Current

At steady state, the total charge contained in the rod cannot evolve in time. In other words, the net current into or out of the rod must be zero. If this condition were not satisfied, the total charge in the rod would tend to positive or negative infinity. Thus we require that

$$I_{anode} + I_{cathode} = 0, \tag{2.46}$$

where I_{anode} and $I_{cathode}$ are the total currents (integrals of current density) over the indicated metal surfaces. Since the current density is proportional to the reaction rate by Faraday's law, in this case conservation of current reduces to conservation of proton flux. (2.46) becomes

$$\int_{anode} j_{anode} dA = -\int_{cathode} j_{cathode} dA, \tag{2.47}$$

where the fluxes j are given by (2.42) and (2.43).

Initially, the rod internal potential ϕ_M is a free parameter. The rod potential directly affects the reaction rates on both the anode and cathode. On the cathode, a more negative rod potential implies a more negative zeta potential, which attracts more protons electrostatically to the surface to screen the more strongly negative surface charge. From the kinetic expression above (2.43), the increase in available protons leads to an increased reaction rate. On platinum, making the potential more negative reduces the overpotential bias in favor of oxidation, which decreases the oxidative reaction rate.

Thus, the requirement of current conservation (2.47) *determines* the value of ϕ_M and gives closure to the mathematical model. The value of the electrode potential that gives zero net current into an electrode is often referred to in electrochemical literature as a "corrosion potential" or "mixed potential." The value of ϕ_M is adjusted iteratively in the simulations until the integrated current leaving the anode surface is equal to the integrated current entering the cathode surface (that is, until (2.47) is satisfied) to within 1 %.

2.5 Non-dimensionalization and Dimensionless Parameters

We use the following scaling values to non-dimensionalize the Stokes, transport, and boundary condition equations:

$$[\mathbf{u}] = U_{ev},\ [\nabla\phi] = E_0,\ [\rho_e] = \rho_{e,0} \tag{2.48}$$

$$[C_i] = C_{i,\infty},\ [p] = \eta U_{ev}/d,\ [j_+] = D_+ C_{+,\infty}/a. \tag{2.49}$$

$$[r, z] = a \text{ (advection-diffusion)}, d \text{ (Stokes)}. \tag{2.50}$$

U_{ev} is the *electroviscous velocity* (discussed in detail below), $\rho_{e,0}$ and E_0 are characteristic values for the charge density and electric field, $C_{+,\infty}$ is the bulk proton concentration, a is the length scale over which electrical body forces are important, and d is a viscous length scale. In dimensionless form, the Stokes and transport equations become

$$0 = \frac{1}{Re}\left(-\bar{\nabla}\bar{p} + \bar{\nabla}^2\bar{\mathbf{u}} + \bar{\rho}_e\bar{\mathbf{E}}\right), \tag{2.51}$$

$$Ra_e(\bar{\mathbf{u}} \cdot \bar{\nabla}\bar{C}_\pm) = \bar{\nabla}^2\bar{C}_\pm - \beta\bar{\nabla} \cdot (\bar{C}_\pm\bar{\mathbf{E}}), \tag{2.52}$$

where overbars denote dimensionless variables and the normalized ion concentration $\bar{C}_{\pm} \equiv C_{\pm}/C_{\pm,\infty}$. The Reynolds and electric Rayleigh numbers are defined as

$$Re \equiv \frac{\rho U_{ev} d}{\eta}, \tag{2.53}$$

$$Ra_e \equiv \frac{U_{ev} a}{D_+}. \tag{2.54}$$

The natural velocity scaling in this system is the electroviscous velocity, which is defined as

$$U_{ev} \equiv \frac{\rho_{e,0} E_0}{\eta/d^2}. \tag{2.55}$$

The electroviscous velocity was first reported by Hoburg and Melcher [44] and reflects the balance of viscous and electrical body forces in the system. We expect that the speed of the rod will scale with U_{ev}. To understand how U_{ev} varies with system parameters, we must therefore understand how $\rho_{e,0}$ and E_0 scale with those same parameters. Below we derive scaling relations for the charge density $\rho_{e,0}$ and electric field E_0 to determine the dependence of U_{ev} on various parameters of the system. We find that the form of $\rho_{e,0}$ depends on whether or not the rod surface is charged, and analyze the possible cases separately.

The Reynolds number describes the relative importance of inertial and viscous forces and is no larger than 10^{-3} in all results reported in this thesis. The electric Rayleigh number is defined similarly to a Péclet number; however, here fluid velocity arises not from bulk advection (as in the case of the Péclet number) but from internally generated electroconvection (similar to natural convection) and thus we refer to the dimensionless group as a Rayleigh number. The Rayleigh number, as defined here, describes the relative importance of electroconvection and diffusion in transporting mass in the system [79, 69, 61].

The dimensionless quantity β is defined as

$$\beta \equiv \frac{zFE_0 a}{RT}, \tag{2.56}$$

and describes the relative importance of electromigration and diffusion in transporting species in the system. Using the above scaling, the boundary condition for the proton flux can be stated in dimensionless form as

$$\mathbf{n}\cdot\left(-\bar{\nabla}\bar{C}_{+}+\beta\bar{C}_{+}\bar{\mathbf{E}}+Ra_{e}\bar{C}_{+}\bar{\mathbf{u}}\right)=Da, \tag{2.57}$$

where Da is the Damköhler number, a dimensionless parameter describing the relative importance of reactions and diffusion in transporting species. In this thesis, Damköhler number is defined differently depending on the reaction kinetic model being used. In general, Da is defined as the reaction-driven flux normalized by a characteristic diffusion-driven flux:

$$Da\equiv\frac{j_{+}a}{D_{+}C_{+,\infty}}. \tag{2.58}$$

In general, the proton flux j_{+} is given by a kinetic expression, and thus the Damköhler number depends on the reaction rate constant and takes a different form on the anode and cathode. On the anode end, (2.57) becomes[5]

$$\mathbf{n}\cdot\left(-\bar{\nabla}\bar{C}_{+}+\beta\bar{C}_{+}\bar{\mathbf{E}}+Ra_{e}\bar{C}_{+}\bar{\mathbf{u}}\right)=Da_{anode}\bar{C}_{H2O2}, \tag{2.59}$$

where

$$Da_{anode}=\frac{K_{O,anode}aC_{H2O2,\infty}}{D_{+}C_{+,\infty}}, \tag{2.60}$$

and on the cathode,

$$\mathbf{n}\cdot\left(-\bar{\nabla}\bar{C}_{+}+\beta\bar{C}_{+}\bar{\mathbf{E}}+Ra_{e}\bar{C}_{+}\bar{\mathbf{u}}\right)=Da_{cathode}\bar{C}_{H2O2}\bar{C}_{+}^{2}, \tag{2.61}$$

where

$$Da_{cathode}=\frac{K_{R,cathode}aC_{H2O2,\infty}C_{+,\infty}}{D_{+}}. \tag{2.62}$$

---

[5] In deriving these expressions, we have assumed the exponential terms in the kinetic equations (2.42) and (2.43) are equal to unity, effectively assuming that the Stern voltage is negligible. Although this assumption is not always valid, it is well-justified in the cases when no supporting electrolyte is present, as we will show in detail below. The definitions of the Damköhler numbers, (2.60) and (2.62), do not change regardless of whether or not the Stern voltage terms are included.

	Formula	**Numerical**
Ra_e	$1.2 \times 10^{-3}/4.9 \times 10^{-3}$	$1.1 \times 10^{-5}/6.0 \times 10^{-5}$
Da_{anode}	8.9/18	1.2/1.1
$Da_{cathode}$	16/32	1.2/1.1
β	0.037/0.071	0.20/0.18

Table 2.1: Calculated and estimated values of the Rayleigh and Damköhler numbers, as well as the parameter β. The first column shows the calculated values of the dimensionless parameters from equations (2.54), (2.56), (2.60), and (2.62) for bulk hydrogen peroxide concentrations of 0.75 mol/L and 1.5 mol/L. The second column shows numerical estimates of the dimensionless parameters for both values of peroxide concentration.

Although the Damköhler numbers are defined differently on the anode and cathode, the rate constants in (2.60) and (2.62) have different units, such that the Damköhler number is dimensionless in each case.

The dimensionless parameters defined above depend on various system properties, including reaction-driven flux; the viscous, electric field, and charge density length scales; and the viscosity and temperature of the aqueous solvent. Here we calculate the values of the Damköhler and Rayleigh numbers and β from their respective formulas using appropriate values of the system variables. In addition, we estimate these parameters using values we extract directly from the simulations.

Each parameter represents the relative dominance of one form of transport to another: reactions to diffusion (Da), electroconvection to diffusion (Ra_e), or electromigration to diffusion (β). To further understand the relative importance of these transport mechanisms, we calculate numerical approximations to these three parameters by numerically integrating the relevant fluxes throughout the system geometry and computing the appropriate ratios. The total flux (in mol/s) due to the reactions alone is given by the integral of the reaction-driven flux j_+ over the anode or cathode surface. The total diffusive, convective, and electromigration fluxes are estimated by integrating the z-components of the appropriate local fluxes over the two-dimensional annular disk surrounding the middle of the rod and extending from the rod surface to the boundary of the simulation domain. The vast majority of the flux occurs within the EDL, within 1 μm of the surface. In this way we obtain an estimate of the total number of cations transported from the anode side to the cathode side due to diffusion, electromigration, and electroconvection.

Table 2.1 shows the values of the dimensionless parameters calculated using equations (2.54), (2.56), (2.60), and (2.62), as well as estimates of the flux ratios calculated using numerical integration. The parameters are evaluated for two bulk hydrogen peroxide concentrations, 0.75 mol/L and 1.5 mol/L, separated by a forward slash. For the Rayleigh number, the simulated swimming speed of the rod was used for U_{ev}. For the electric field term in the parameter β we use a characteristic electric field E^*, which we define as the external electric field required to drive conventional electrophoresis of the particle at a speed equal to U_{ev}. Mathematically,

$$E^* = \frac{\eta}{\varepsilon\zeta} U_{ev}. \tag{2.63}$$

Under realistic experimental conditions, both the direct formula calculations and numerical approximations result in Rayleigh numbers of $O(10^{-3})$. This suggests that electroconvection is dominated by diffusion in driving cation transport. The Damköhler number is typically $O(10)$ in our system, indicating that the diffusive transport roughly balances the reaction-driven transport. The analytically determined values are roughly one order of magnitude larger. As defined, the Damköhler numbers depend on the bulk concentrations of reactants, which actually vary significantly within the double layer. Thus, the indicated values of the analytically determined Damköhler numbers may not accurately reflect conditions near the rod surface. The parameter β is $O(0.1)$ as calculated from both the formulas and numerical approximations. From the simulations, we can determine that more mass is transported by diffusion than my electromigration.

The values of β and Da calculated numerically change slightly with hydrogen peroxide concentration. We attribute this to variations in zeta potential that accompany variations in flux (due to the current conservation constraint, (2.46)). When the peroxide concentration increases, the transport due to diffusion, electromigration, and reactions increase by approximately the same amount and therefore the dimensionless parameters reflecting the relative dominance of these mechanisms do not vary appreciably. As expected, the Rayleigh number, although very small in comparison to β, increases with the electroviscous velocity for both the analytical and numerical calculations. As dictated by the formulas, the analytical values of the Damköhler numbers vary directly with background peroxide concentration. The variation in the analytical value of β with peroxide concentration is expected, given the definitions of E^* and β stated above, and also taking into account the variation in zeta potential with peroxide concentration.

In summary, we conclude from this analysis that transport in the system is driven primarily by diffusion and electromigration, and that contributions from electroconvection are negligible in this system. Since there will be no electroconvection, diffusion, or electromigration without reactions, we expect that the combination of these transport mechanisms will always balance the reaction-driven flux.

2.6 Scaling Analysis

It is instructive to determine the variation in electroviscous velocity U_{ev} with parameters of the system, since the swimming speed of the rod scales with U_{ev}. There are two primary sources of space charge in the system: the reactions, which inject and consume cations asymmetrically, leading to a dipolar charge distribution; and the surface charge on the particle, which attracts the oppositely charged diffuse screening layer, which surrounds the particle roughly uniformly.

The charge density derived from the reactions scales with the reaction-driven flux of protons, j_+, and the diffusivity of protons, D_+, according to

$$\rho_e \propto \frac{Fj_+L}{D_+}, \tag{2.64}$$

where L is a length scale over which finite charge density exists. As diffusion becomes stronger (*i.e.* as D increases or L decreases), it more efficiently spreads ions out over a larger volume, decreasing the charge density. The length scale L is a characteristic length over which the charge density decays to its bulk value of zero and is conceptually similar to the Debye length for the case with a charged rod surface.

Through Poisson's equation, we can relate the scaling for charge density (2.64) to the characteristic electric field generated *by* that charge density distribution, E_0, according to

$$\frac{Fj_+L}{D_+} \propto \frac{\varepsilon E_0}{a}, \tag{2.65}$$

where a is a length scale over which the tangential (parallel to the rod axis) electric potential gradient is significant. The electric field E_0 then scales linearly with the flux as

$$E_0 \propto \frac{Fj_+La}{\varepsilon D_+}. \tag{2.66}$$

Assuming the important space charge in the system arises due to the reactions *only*, we can combine (2.55), (2.64), and (2.66) and find

$$U_{ev} \propto \frac{F^2 j_+^2 a L^2 d^2}{\varepsilon \eta D_+^2} \tag{2.67}$$

for the electroviscous velocity scaling. We can simplify this expression by specifying values for the length scales. In general, the most important length scale in the system is the Debye length, (2.21). The charge density length scale, L, diminishes in size with increasing ion concentration, and approximately scales with the Debye length, λ_D. The tangential component of the dipolar electric field, which is ultimately responsible for initiating electro-osmotic flow, is also assumed to scale with the Debye thickness, λ_D. As the conductivity of the solution decreases, Ohm's law dictates that the electric field must decrease (assuming the reaction-driven current density in the solution is roughly constant). Finally, significant velocity gradients and viscous stresses exist primarily in the diffuse layer. Thus, the appropriate viscous length scale is also the Debye thickness, λ_D. We can thus rewrite (2.67) as

$$U_{ev} \propto \frac{F^2 \lambda_D^5}{\varepsilon \eta D_+^2} j_+^2. \tag{2.68}$$

Equation (2.68) is valid if the dominant source of space charge is the reactions. However, if the rod is charged, the surface will attract counterions from the bulk solution which form a diffuse screening layer, as discussed above. The ion concentrations are highly unbalanced in this layer, resulting in a high density of charge in the diffuse layer that counterbalances the charge on the surface. Depending on the relative magnitudes of the surface charge and reaction-driven flux, either source of charge density may dominate.

For the values of surface potential considered in this work, the charge density due to the diffuse layer dominates. The potential ϕ in the diffuse layer scales with the surface potential, $\phi \propto \zeta$, and so we can write a characteristic charge density based on the Boltzmann distribution as

$$\rho_{e,0} \propto \frac{F^2 z^2 C_{\pm,\infty} \zeta}{RT} \propto \frac{\varepsilon \zeta}{\lambda_D^2}. \tag{2.69}$$

Although the charge in the diffuse layer is greater in magnitude than that due to the reactions, the asymmetry in reaction-driven charge density still generates the electric field E_0, which is still the only electric field in the z-direction. Thus, we insert the charge density expression (2.69) and the electric field generated by the reactions (2.66) into the electroviscous velocity definition (2.55) to obtain

$$U_{ev} \propto \frac{\zeta F j_+ L a d^2}{\lambda_D^2 \eta D_+}. \tag{2.70}$$

Using the same scalings discussed above ($L \propto \lambda_D$, $a \propto \lambda_D$, $d \propto \lambda_D$), we can simplify (2.70) to obtain

$$U_{ev} \propto \frac{F \lambda_D^2}{\eta D_+} \zeta j_+. \tag{2.71}$$

Note that (2.71) can be expressed in a form similar to the Helmholtz-Smoluchowski equation,

$$U_{ev} \propto \frac{\varepsilon\zeta}{\eta} E_0 = \frac{\varepsilon\zeta}{\eta} \frac{F j_+ \lambda_D^2}{\varepsilon D_+}, \tag{2.72}$$

in which the particle has the usual electrophoretic mobility $\varepsilon\zeta/\eta$, but the electric field is the characteristic internally generated electric field given in (2.66).

For a charged rod, our scaling analysis thus predicts that the velocity will increase linearly with the reaction flux j_+ and zeta potential ζ. We also expect that the velocity will vary inversely with the background ion concentration through the dependence on the square of Debye thickness.

Chapter 3

SIMULATION DETAILS

3.1 Finite Element Method

We solve the governing equations (2.8), (2.11), (2.12) and (2.13) using the finite element method. The continuous simulation domain is discretized into a set of discrete, triangular sub-domains called "mesh elements." The subdivision of the domain into simpler parts has a several advantages, including most importantly the accurate representation of complex geometries. Due to the strong gradients in the field variables in the region near the rod, the mesh resolution is much finer in the vicinity of the rod than in the bulk solution (see Fig. 3.1).

The finite element method discretely approximates the system of continuous partial differential equations, in such a way as to reduce the problem to a sparse matrix equation, of the form

$$-L\mathbf{u} = \mathbf{b}, \tag{3.1}$$

where the vector $\mathbf{b}$ is known, L is a (generally very large) sparse, positive definite matrix, and $\mathbf{u}$ is the unknown solution vector. A number of numerical solvers exist that exploit the sparseness of the matrix L to solve the system (3.1) using methods that are much more efficient than actually inverting the matrix L. In this work, we use the PARDISO linear system solver developed by Schenk & Gärtner [88, 89], which is a high-performance, robust, and memory-efficient software for solving large sparse symmetric and unsymmetric linear systems. The solver is implemented using COMSOL Multiphysics version 3.5a, a commercial finite-element analysis software package.

3.2 Simulation Domain

The simulations are conducted in a square domain having area $100 \times 100\ \mu\text{m}^2$. We have determined that this is a sufficient size to suitably approximate an infinite medium. Since the problem is axisymmetric, we solve the equations over a two-dimensional "slice" of the three-dimensional problem.

Figure 3.1 shows the region of the simulation domain near the rod and visualizes the mesh, whose resolution is fine near the rod and coarse in the bulk solution. The rod's centroid is positioned at the midpoint of the left side of the domain, on the axis of symmetry. The length of the simulated rod is 2 microns and its radius is 150 nanometers. To prevent electric field singularities from appearing near the corners of the rod, they are rounded with a radius of curvature of 25 nm. This rounding also accounts for possible imperfections during rod fabrication.

The size of the domain was determined by first running simulations in domains of size 30×30, 50×50, and 100×100 μm^2. The calculated values of the rod swimming speed changed by less than 1 % when the domain size was increased from 50×50 to 100×100 μm^2. We thus concluded that the 100×100 μm^2 domain was sufficiently large to approximate an infinite medium, and that the fluid speed in the direction of swimming measured at the far edge of the domain was sufficiently close to the fluid speed an infinite distance from the rod (in the rod reference frame), which by definition is equivalent to the speed of the rod with respect to the fluid.

The domain is typically discretized into approximately 128,000 triangular mesh elements. The mesh resolution is much higher near the particle surface than in the bulk solution. As shown in the zoomed version of Fig. 3.1, in the region within the electrical double layer, a mesh element typically measures roughly 1 nm on one side.

3.3 Validation

In order to verify that the finite-element solver computes physical solutions, we solved the Poisson-Nernst-Planck-Stokes equations for electrophoresis of a spherical non-conducting particle of radius 1 μm in an externally applied electric field. As in the simulations of the swimming rods, we measured the electrophoretic speed as the speed on the domain boundary opposite the particle as a function of the sphere's zeta potential and applied electric field. We compared our results with Henry's equation,

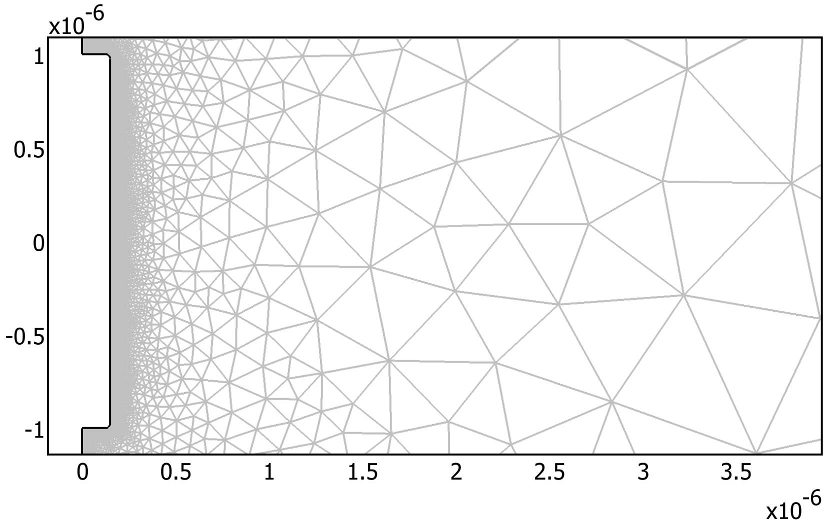

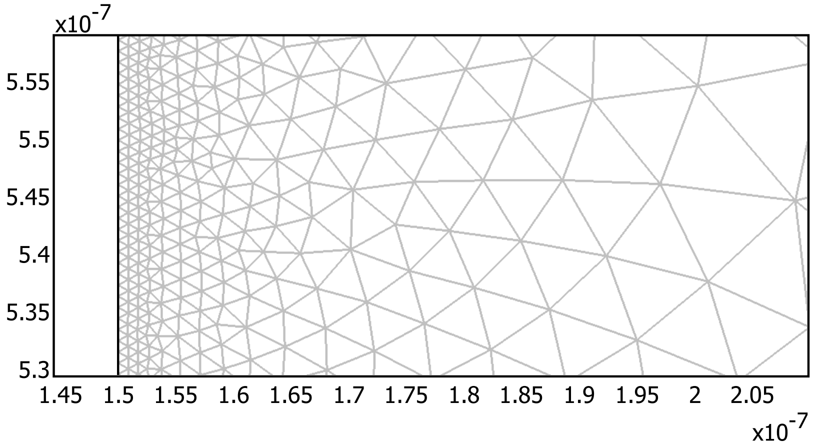

Figure 3.1: (top) Finite-element mesh used for nanorod simulations; (bottom) Zoomed version showing mesh element resolution near the rod surface. The simulation domain contains approximately 128,000 triangular mesh elements, most of which are concentrated near the rod surface, shown in the left of this figure. The r and z coordinates (in meters) are shown on the horizontal and vertical axes, respectively.

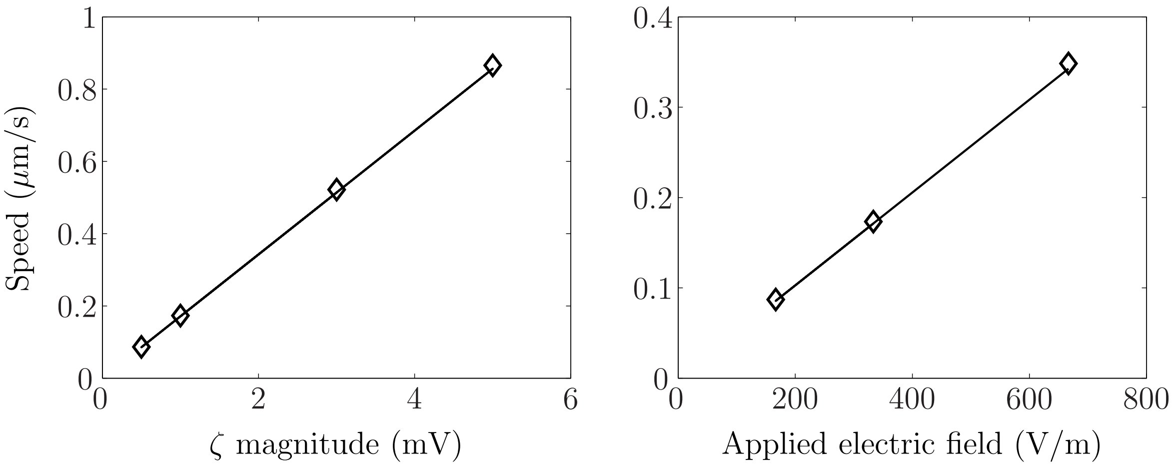

Figure 3.2: Results for validation simulations of externally driven electrophoresis of an insulating spherical particle of radius 1 μm. In both figures, simulations are indicated with open diamonds, and the speed U_{Henry} predicted by (3.2) is shown with a solid line. (left) Speed vs. zeta potential magnitude for a constant applied electric field of 333 V/m. (right) Speed vs. applied electric field for a constant zeta potential of magnitude 1 mV.

[42]:

$$U_{Henry} = \frac{2\varepsilon\zeta E_{app}}{3\eta} f\left(\frac{R_s}{\lambda_D}\right), \tag{3.2}$$

where E_{app} is the applied electric field, $R_s = 1$ μm is the radius of the sphere, and f is Henry's function. Figure 3.2 shows excellent agreement between the simulations and the predictions of (3.2) for several values of the applied electric field and zeta potentials smaller in magnitude than the thermal voltage.

3.4 Constants

Table 3.1 shows the values and units of important constants used in the simulations. In this work, the constants $K_{O,anode}$ and $K_{R,cathode}$ are used as fitting parameters. Their values were chosen to yield values of the proton fluxes equivalent to current densities that are comparable to those measured by Paxton et al. [76].

Constant	Description	Value
$K_{O,anode}$	Oxidation rate constant, anode	5.5×10^{-9} m s^{-1}
$K_{R,cathode}$	Reduction rate constant, cathode	1 m^{7} s^{-1} mol^{-2}
D_+	Diffusivity, protons	9.311×10^{-9} m^{2} s^{-1}
D_-	Diffusivity, hydroxide ions	5.273×10^{-9} m^{2} s^{-1}
$D_{H_2O_2}$	Diffusivity, hydrogen peroxide	6.6×10^{-10} m^{2} s^{-1}
D_{O_2}	Diffusivity, molecular oxygen	2×10^{-9} m^{2} s^{-1}
η	Solution viscosity	8.9×10^{-4} Pa s
ρ	Solution density	998 kg m^{-3}
$C_{\pm,\infty}$	Bulk concentration, ions	10^{-7} mol L^{-1}
$C_{O_2,\infty}$	Bulk concentration, molecular oxygen	0.2×10^{-3} mol L^{-1}
ε_r	Solution dielectric constant	78.4
λ_D	Debye thickness	0.961 μm
λ_S	Effective Stern layer thickness	1 nm

Table 3.1: Values of relevant constants used in the simulations. The mobilities of the charged species are given by the Nernst-Einstein relation, $\nu_i = D_i/RT$, where R is the ideal gas constant and $T = 298.15$ K. The value of the bulk hydrogen peroxide concentration, $C_{H_2O_2,\infty}$ is not shown because it is varied throughout the work.

Chapter 4

UNCOUPLED MODEL

4.1 Introduction

This chapter presents the results of simulations conducted in the early stages of the thesis research, prior to the development of the coupled reaction kinetic model presented in Chapter 2. Here, we imagine the simplest model possible of the rods by assuming that the rod has a constant surface charge (either zero or nonzero) and piecewise uniform reaction rates on its surface, and that these parameters can be varied independently of one another.

This chapter has two parts. In §4.3, we present results for a rod whose internal electric potential is initally set to zero and allowed to float. Although the results presented in this section are not realistic in that they do not allow the rod to have an innate electrical potential, they are instructive in showing that electrochemical reactions alone, in theory, are capable of generating concentration polarization, electric fields, and a resulting electroviscous flow that is nonlinear in the reaction rate. The reactions alone generate a symmetric, quadrupolar velocity field that is reminiscent of induced-charge electro-osmosis [93].

In §4.4, we show the effects of assuming a constant, negative zeta potential on the rod surface. We show that the surface charge breaks the symmetry of the quadrupolar flow generated by the reactions, and causes the locomotion of the rod. The results in this chapter imply that surface charge is necessary for locomotion of the rod to occur; furthermore, the magnitude and sign of the zeta potential (which quantifies the surface charge) determine the speed and direction of the rod's motion, respectively. If the sign of the zeta potential is switched, the motion reverses direction.

4.2 Mathematical Model

The mathematical model employed for these simulations is simpler than that presented in Chapter 2. For this chapter, we make two important simplifying assumptions.

The first assumption is that the charge on the rod surface is uniform. Thus, in this case, the electric potential boundary condition on the rod surface (2.18) is replaced with

$$\phi_M = \zeta = \zeta_0, \tag{4.1}$$

where ζ_0 is a constant, chosen based on published values of the surface charge on metal rods in aqueous solutions. Dougherty *et al.* measured the zeta potential of monometallic gold, silver, and bimetallic gold/silver nanorods and found values ranging from 0 to -60 mV [22]. Paxton *et al.* measured the zeta potential of platinum/gold bimetallic nanorods and reported an average value of -41 mV [76] . To examine the effects of varying zeta potential on the motion, in particular the linear dependence of speed on zeta potential predicted by (2.71), here we consider values of ζ_0 ranging from 0 to -40 mV.

The second assumption is that the reaction-driven fluxes are piecewise uniform on the rod surface. Adopting the convention that positive flux corresponds to protons released from the rod into the solution, we set the flux to a constant positive value on the anode side,

$$j_{anode} = j_0, \tag{4.2}$$

and an equal and opposite value on the cathode side,

$$j_{cathode} = -j_0, \tag{4.3}$$

where j_0 is a prescribed constant value. Equations (4.2) and (4.3) replace the Butler-Volmer expressions, equations (2.42) and (2.43) respectively, in the boundary condition for proton flux, equation (2.26). The values for j_0 are chosen based on the data of Paxton *et al.* [76], who measured the catalytically generated current density on Pt and Au interdigitated microelectrodes in hydrogen peroxide. Their measured values are equivalent to proton fluxes ranging from 10^{-6} to 10^{-5} mol/(m^2·s). Here, we allow the reaction-driven flux j_0 to vary from 10^{-6} to 7×10^{-6} mol/(m^2·s).

These simplifications effectively remove the coupling between the surface charge and reaction rates, making them independent, adjustable parameters. For this reason, we refer to the model presented in this chapter as the *uncoupled model.* A similar model was developed by Kline *et al.* [56] to analyze the catalytically driven fluid flows generated by concentric metallic electrodes in hydrogen peroxide, as they observed previously [55]. Although this approach is not as realistic as a fully coupled model, it can yield plausible results for the field variables and swimming speed and gives some insight into the locomotion physics, especially the importance of the surface charge.

We find that the behavior of the system changes significantly depending upon whether the rod surface is uncharged or charged (that is, if ζ_0 is zero or finite). We analyze the two cases separately in the following sections.

4.3 Uncharged Rod; Constant Flux

We first present the results for an uncharged rod with piecewise constant fluxes on its surface. The reactions occurring on the surface drive electrical and ion polarization and generate electroviscous flows that are nonlinear in the flux j_0. However, these effects do not lead to net locomotion of the rod.

Since the surface charge is assumed to be zero, these simulations show the effects of the reactions alone. The continuous injection and consumption of charged species causes a polarized non-classical diffuse layer of dipolar space charge to form around the rod. The interior of the rod remains at zero potential, but the potential at the outer Helmholtz plane (OHP) relative to the bulk solution is allowed to float. Thus, the potential at the OHP (the effective zeta potential) is determined by the local charge density induced by the reactions. This could be interpreted physically as a rod with zero internal potential with a spatially varying potential drop across the Stern layer. Thus, although we refer to this case as “uncharged,” the zeta potential of the rod does in fact vary slightly with position, in a nearly identical fashion to the potential variation prescribed by Lammert *et al.* on the surface of a spherical cell

[57]. The "uncharged" label thus refers to the internal potential of the rod, which is zero at steady state.

The distributions of proton concentration, electric potential, electric field, and charge density are shown in Fig. 4.1. The contour values for concentration, potential, and charge density have been non-dimensionalized and negative values are indicated by dotted contour lines. Figure 4.1 (a) shows contours of the dimensionless perturbation to the equilibrium proton concentration, given as

$$\tilde{C}_{+} = \frac{C_{+} - C_{+,\infty}}{C_{+,\infty}}. \tag{4.4}$$

Figure 4.1 (b) shows contours of the electric potential, which has been normalized by the thermal voltage,

$$\tilde{\phi} = \frac{\phi F}{RT}. \tag{4.5}$$

Figure 4.1 (c) shows streamlines of the electric field, showing the dipolar pattern expected from the potential profile in (b). Finally, the dimensionless charge density, plotted in Fig. 4.1 (d), is given by

$$\tilde{\rho}_e = \frac{\rho_e F \lambda_D^2}{\varepsilon RT}. \tag{4.6}$$

In Figs. 4.1 (a-d), the flux j_0 is defined such that $j_0/j_d = 0.78$, where the flux has been normalized by a characteristic flux j_d based on Nernst's diffusion-limited current density, as discussed in ref. [6]. It is defined as

$$j_d = \frac{4D_{+}C_{+,\infty}}{\lambda_D}. \tag{4.7}$$

The distributions of $\tilde{C}_{+}$ and $\tilde{\rho}_e$ are qualitatively very similar, as indicated in Figs. 4.1 (a) and (d), respectively. Both quantities are strongly positive near the anode and strongly negative near the cathode. The polarized charge clouds surrounding the rod effectively generate an electric dipole whose moment increases with reaction rate. This dipole generates an electric field, as illustrated by the electric field streamlines in Fig. 4.1 (c). The electric field points from the anode to the cathode, and so on the

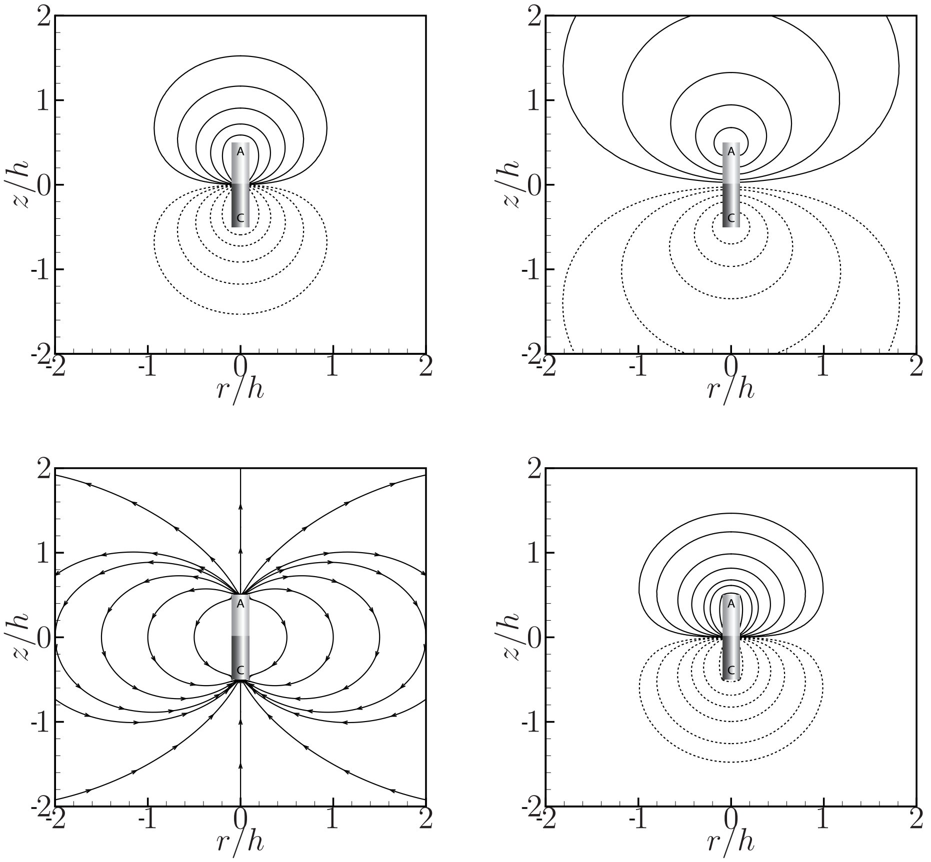

Figure 4.1: Simulation-generated plots created assuming piecewise constant proton fluxes and an uncharged rod. (a) Dimensionless proton concentration plotted for values of $\tilde{C}_+ = \pm 0.025$, 0.05, 0.1, 0.2, and 0.4 (values increase in absolute value approaching the rod surface), (b) dimensionless electric potential plotted for $\tilde{\phi} = \pm 0.005$, 0.01, 0.02, 0.03 and 0.04 (from the outside inward), (c) dipolar electric field lines, and (d) dimensionless charge density, plotted for $\tilde{\rho}_e = \pm 0.005$, 0.01, 0.025, 0.05, 0.1, 0.15, and 0.3 for the case of an uncharged rod and flux $j_0/j_d = 0.78$. These figures look qualitatively very similar for other values of the flux j_0. Note that strong qualitative similarity between the profiles of proton concentration and charge density, indicative of the strong coupling between the two quantities. Dashed contour lines indicate negative values. In these figures, as with similar figures throughout this thesis, the anode (where protons are being generated) is denoted with a letter A and the cathode (where protons are being consumed) with a C; the r and z coordinates are normalized by the length of the rod, $h = 2$ μm.

sides of the rod the z component of the field is negative (*i.e.*, downward in Fig. 4.1 (c)). The electrical body force is given by the product of charge density and electric field; thus, when the charge density at a particular location is positive (negative), the body force and electric field vectors point in the same (opposite) directions. At the anode, the electric field exerts a body force on the fluid that points in the negative z direction. At the cathode, the field exerts a body force in the positive z direction. These opposing body forces are of comparable strength and lead to electro-osmotic flows in their respective directions along the rod surface. The two fluid streams intersect at the anode/cathode junction and are driven radially outward from the rod to conserve mass. As a result, the velocity field takes on a quadrupolar shape which is reminiscent of induced-charge electro-osmosis (ICEO), as shown in Fig. 4.2 (see [93]). Due to the near-perfect symmetry of the flow field and small velocity magnitudes, in this case there is no considerable net locomotion of the particle.

ICEO flows around ideally polarizable rod-like particles have been described in several recent works. Rose *et al.* [83] observed the rotation of metallic nanorod particles under an applied electric field, which was driven by ICEO flows generated by the field. Induced-charge electrophoresis (ICEP) around ideally polarizable colloidal rods was investigated theoretically and numerically by Saintillan *et al.* [85], who focused on hydrodynamic interactions among multiple colloidal rods undergoing ICEP. The same authors later further extended this analysis to colloidal metallic rods sedimenting in a gravitational field [86], whose motion was stabilized by the application of an electric field and the resulting ICEP flow. In contrast, here the ICEO-like flow does not require an external electric field but is instead driven by the interaction between the dipolar charge density distribution induced by the reactions and the electric field it creates.

Figure 4.3 shows the maximum fluid velocity magnitude in the system as a function of the dimensionless flux j_0/j_d. The speed increases quadratically with the flux, as predicted by the scaling relationship (2.67) and shown in the solid line, which is a

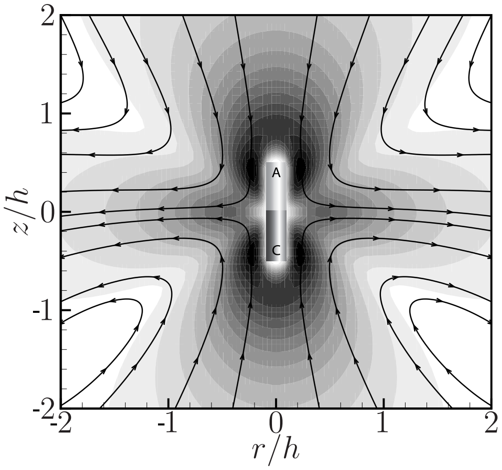

Figure 4.2: Velocity field magnitude (color) and streamlines for the case of no surface charge and piecewise constant reaction-driven flux. Dark and light colors indicate high and low velocity magnitudes, respectively. The velocity magnitude is maximized near the rod. Here the dimensionless flux $j_0/j_d = 0.78$, but this figure looks qualitatively very similar for other values of the flux j_0. On the anode end, the positive charge density (Fig. 4.1 (d)) and electric field in the $-z$ direction (Fig. 4.1 (c)) coupled to produce an electrical body force that also points in the $-z$ direction. On the cathode end, the negative charge density and electric field (which still points in the $-z$ direction) couple to produce an electrical body force in the $+z$ direction. These opposing body forces are of comparable strength and lead to fluid slip in their respective directions along the rod surface. Downward-moving fluid collides with upward-moving fluid at the rod equator, and the streams are forced outward due to incompressibility. The flow profile resembles induced-charge electro-osmosis (ICEO) and does not cause any locomotion of the particle.

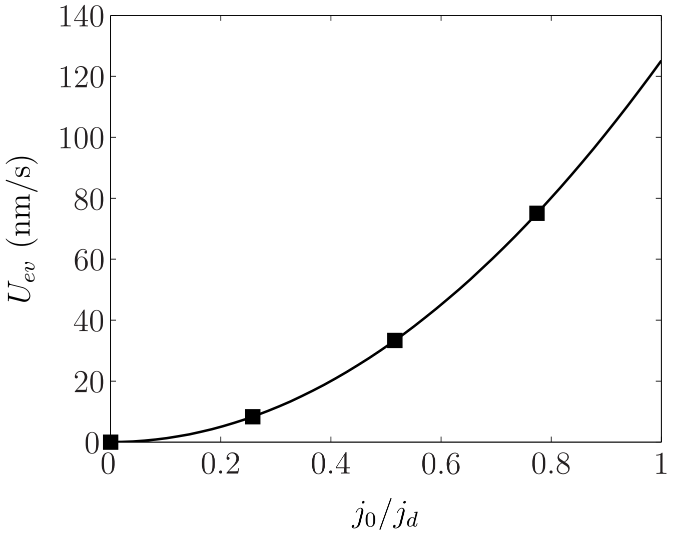

Figure 4.3: Maximum electroviscous velocity (maximum magnitude in figure 4.2) in the system as a function of dimensionless reaction-driven flux for the case of an uncharged rod. The solid line is a quadratic fit to the data. This figure verifies the prediction of (2.68) that, for an uncharged rod, the fluid speed should depend quadratically on the flux. Although here we plot the maximum velocity in the entire simulation domain, the Eulerian fluid velocity measured at any given point varies quadratically with the flux as well. However, the velocity vanishes as $|\mathbf{r}| \to \infty$ in all cases, indicating that the rod does not move with respect to the fluid.

quadratic least-squares fit to the data. While the rod generates these flow profiles in its immediate vicinity, the bulk fluid far from the rod does not flow appreciably. The velocity magnitude is maximized at 0.1 μm/s, suggesting that the quadrupolar flow generated by the reactions alone would be negligible compared to the ubiquitous Brownian motion. Although these simulations suggest that an uncharged rod will not exhibit detectable axial motion, this case is useful in demonstrating how the injection of charge due to electrochemical reactions can drive an electro-osmotic flow. In the next section, we will show that the inclusion of a constant, negative surface charge leads to rod locomotion with the anode forward, as is seen experimentally.

4.4 Constant, Negative Zeta Potential; Constant Flux

In this section, we present simulations of a rod with the same piecewise constant reaction fluxes as before and a constant, negative zeta potential between -10 and -40 mV. This range of values was determined following the measurements of Dougherty *et al.* [22] and Paxton *et al.* [76].

Figure 4.4 shows the distribution of dimensionless proton concentration (a,d,g), electric potential and electric field lines (b,e,h), and charge density (c,f,i). In all 9 figures, the zeta potential of the particle is set to -10 mV.

The top three plots (a,b,c) are for the case with no reactions and show the distributions of the field variables due to the surface charge only. Figure (a) shows that the proton concentration is locally enriched (since the perturbation to the concentration, $\tilde{C}_+$, is uniformly positive), forming a diffuse screening layer due to the negative surface charge that can be predicted by the Gouy-Chapman model.

The middle three plots (d,e,f) are for the case with reaction-driven flux $j_0/j_d = 0.39$, and in the bottom three plots (g,h,i) the flux is increased to $j_0/j_d = 0.78$. These cases show the combined effects of the surface charge and reactions. Most notably, the charge density is now uniformly positive (due to the positively charged diffuse layer), but is most positive near the anode, where protons are being generated, and is weakly positive near the cathode, where they are being depleted.

The shape of the electric field in Figs. (e) and (h) can be understood by examining the electric field due *only* to the reactions, Fig. 4.1 (c), and the electric field due *only* to the surface charge, Fig. 4.4 (b). The electric fields shown in Figs. 4.4 (e) and (h) are the result of the superposition of these two electric fields. This superposition is responsible for the apparent source of electric field forward of (above) the anode. This source is located closer to the rod surface in the higher-flux case (h). In the no-flux case (b), the electric field lines are everywhere normal to the rod surface, as predicted by Gouy-Chapman theory. When the flux is finite, proton fluxes are introduced into

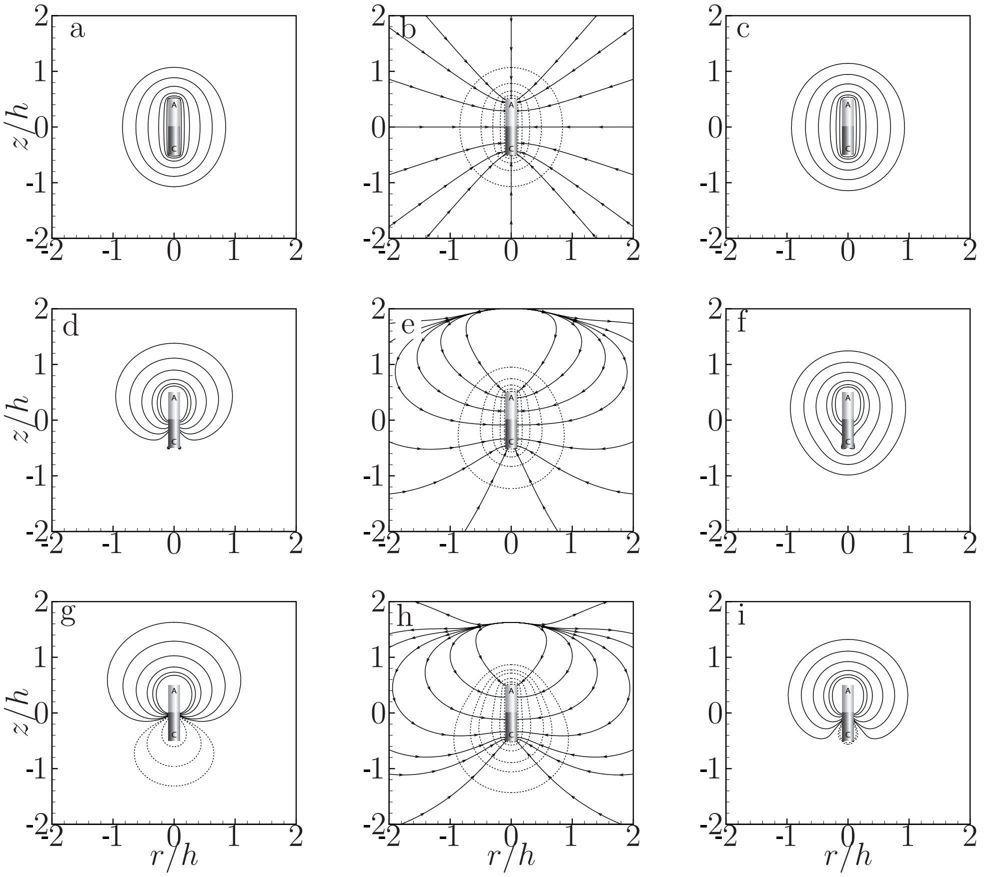

Figure 4.4: Simulation-generated plots created using the uncoupled model assuming a constant, negative zeta potential of -10 mV. Contours are shown of dimensionless proton concentration, dimensionless potential (with electric field streamlines), and dimensionless charge density for three separate cases. (a,b,c): no flux ($j_0 = 0$), corresponding to a case with no peroxide. Thus (a,b,c) show the effects of the negatively charged surface only. (d,e,f): j_0/j_d =0.39. (g,h,i): j_0/j_d =0.78. The contour values for the concentration $\tilde{C}$ are (a,d,g): 0.025, 0.05, 0.1, 0.2, 0.3, 0.4 (in (g) negative contours have been added corresponding to -0.025, -0.05, -0.2); potential $\tilde{\phi}$ (b,e,h): -0.025, -0.075, -0.15, -0.25, -0.35; charge density $\tilde{\rho}_e$ (c,f,i): 0.05, 0.1, 0.2, 0.4, 0.6, 0.8 (in (i) negative cotnours have been added corresponding to -0.05 and -0.1). All contour values increase with decreasing distance to the rod surface. Dotted contour lines indicate negative values.

the system and a second electric field develops that has a source at the anode surface. When these electric fields are combined, the overall field appears to have a source near the anode end of the rod. We have confirmed that there is a weak, but real, source of electric field at the point indicated in Figs. 4.4 (e) and (h) by plotting the divergence of electric field, which is proportional to the charge density distribution. This source goes unnoticed in the charge density plots (Figs. 4.4 (f) and (i)) because it is two orders of magnitude weaker than the electric field sink at the negatively charged rod surface.

The position of the source is controlled by the relative dominance of the reaction-induced and the surface-induced electric fields. The more dominant the reaction-induced electric field is in relation to the surface-induced field, the more closely the entire plot resembles Fig. 4.1 (c), and the closer the source is to the anode end. The more dominant the surface-induced field is over the reaction-induced field, the more closely the plot resembles Fig. 4.4 (b). Moving from (e) to (h), the flux is increased but the surface charge is kept constant; thus, the reaction-induced electric field becomes stronger, while the surface-induced electric field stays roughly constant. For this reason, the source of electric field moves closer to the rod.

Figure 4.5 shows the rod swimming speed as a function of the flux j_0/j_d as obtained from the simulations, scaling analysis, and experiments. The experiments and simulations show good agreement assuming a native surface potential of -25 mV, which is in the range of measured values for the zeta potential of gold and platinum particles in aqueous solutions [22, 23]. The rods used in the experiments were grown using electrochemical deposition as described previously [58]. The dimensions of these rods were similar to those in the simulations. We obtained the experimental data in Fig. 4.5 by measuring the speed of Pt/Au rods using optical microscopy in varying concentrations of hydrogen peroxide. Each data point at finite peroxide concentration represents the average of between roughly 15 and 35 rods.

Paxton *et al.* measured the dependence of electrocatalytically generated current

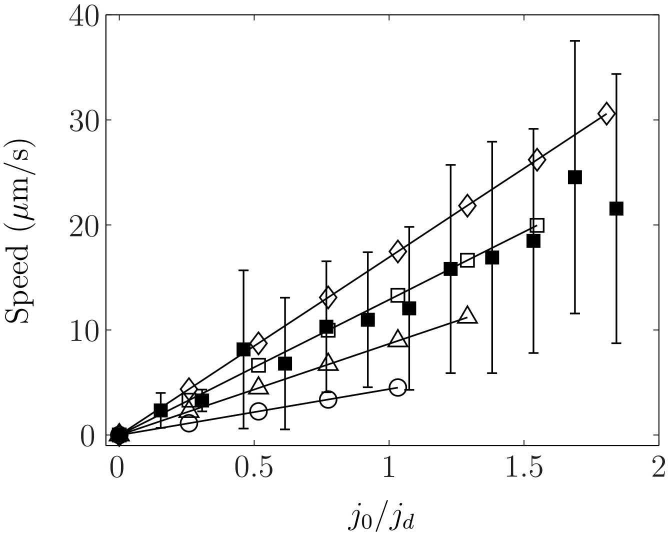

Figure 4.5: Swimming speed as a function of dimensionless reaction-driven flux for simulations and experiments. Simulations (open symbols), scaling analysis (lines), and experiments (black squares) show good agreement. Simulations are shown for four different values of zeta potential: −10 mV (open circles), −20 mV (open triangles), −30 mV (open squares), and −40 mV (open diamonds). The flux data for the experimental data were estimated based on the dependence of flux on peroxide concentration given by Paxton *et al.* [76]. Error bars on the experimental data indicate one standard deviation in each direction. Each experimental data point represents the average of between 15-35 rods.

density on Pt and Au interdigitated microelectrodes [76]. Their measurements suggested a linear dependence of current density on peroxide concentration. A linear fit of the data presented in table 1 of their work yields a fitting equation of

$$i_{cat} = 0.1148 C_{H_2O_2}, \tag{4.8}$$

where i_{cat} is the current density in A/m^2 and $C_{H_2O_2}$ is measured in wt. %. We use this fitting equation to estimate the current density, which is then related linearly to the flux by $j_{cat} = i_{cat}/z_+F$ (Faraday's law), as a function of peroxide concentration, providing the values of j_0/j_d at each peroxide concentration shown in Fig. 4.5. In Fig. 4.5, we have subtracted out the characteristic Brownian velocity of the rods (measured here to be 4.87 μm/s) from all experimental data points in order to only consider the axial component of the velocities measured in the experiments.

4.5 Total Propulsive Force Generated by the Rod

The simulations enable us to estimate the total electrical body force generated by the rod, thereby giving an estimate of the propulsive force generated by the reactions. Burdick *et al.* [10] estimated the propulsive force a nanorod could generate by observing a magnetically guided Pt/Au/Ni/Au rod, with the Pt segment doped with carbon nanotubes, as it dragged cargo of different sizes through a fluid, and recording the migration speeds of the nanorod/cargo complex. Their measurements indicated a propulsive force of roughly 0.16 pN.

We estimate the propulsive force by computing the integral of the total body force in the simulation domain V, according to

$$F_{body,z} = \int_V \rho_e E_z dV. \tag{4.9}$$

Figure 4.6 shows same simulation-generated data for swimming speed shown in Fig. 4.5 as a function of $F_{body,z}$, showing a strong linear correlation. This was initially suggested by the definition of the electroviscous velocity, equation (2.55). This linear

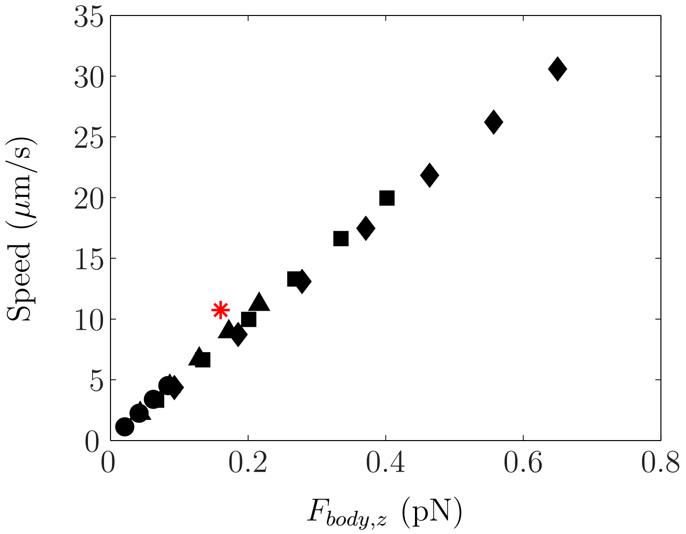

Figure 4.6: Rod swimming speed versus total z-direction electrical body force in the simulation domain, as defined in (4.9). The figure shows a strong linear correlation between swimming speed and body force, as predicted in the definition of electroviscous velocity, (2.55). Red asterisk indicates the experimental measurement of Burdick *et al.* [10] for Pt-CNT/Au/Ni/Au rods towing cargo of size 1.3 μm.

relationship is also in agreement with Stokes' law, considering that the rod is propelled by electrical body forces and opposed by viscous forces, which are balanced at steady state. For the case with $j_0/j_d = 1.0$, $\zeta = -20$ mV, we obtain a propulsive force of 0.17 pN, in good agreement with the value of 0.16 pN computed by Burdick *et al.* [10]. Similar estimates of the propulsive force were reported for Pt/Au nanorods by others [74, 75].

4.6 Conclusion

This chapter has presented scaling analyses, detailed simulations, and experiments relating to the locomotion of bimetallic rods in hydrogen peroxide. The analysis shows that rod movement is the result of an electroviscous slip velocity that is driven by electrical body forces resulting from a coupling between space charge in the solution and the electric field it generates.

The simulations of an uncharged rod with asymmetric constant proton fluxes predict a quadrupolar velocity field around the rod. This flow field does not drive any net locomotion and is qualitatively similar to that observed in induced-charge electro-osmosis near a stationary ideally polarizable particle. The magnitude of the electroviscous velocity depends quadratically on the flux, as predicted by the scaling analysis. To our knowledge, the velocity fields surrounding an uncharged motor shown in Fig. 4.2 have not been observed experimentally because most metallic surfaces obtain some finite surface charge in aqueous solutions, due either to differential adsorption or to electrochemical reactions. In addition, these flows by themselves are too slow to be distinguished from Brownian motion. The results for an uncharged rod illustrate the importance of the charge density and self-generated electric field in generating the electrical body forces that drive fluid motion.

This work shows that surface charge plays a crucial role in causing the locomotion of the rod and determining its direction. In the cases where a nonzero surface charge is assumed, the surface gives rise to a net positive charge in the diffuse layer, which breaks the symmetry of the quadrupolar flow and gives rise to particle motion, as in the case of induced-charge electrophoresis. The electric field pointing from the anode to the cathode couples with the predominantly positive charge density in the diffuse layer to generate an electro-osmotic flow from the anode to the cathode. By Galilean invariance, this is equivalent to the rod moving through the solution with the anode forward. These results indicate that in order to attain the speed and swimming direction observed experimentally, the rods must have a negative effective zeta potential. The scaling analysis and simulation results reveal that the electroviscous velocity depends linearly on the zeta potential and reaction-driven flux. We conclude that the sign and magnitude of the rod surface charge play a crucial role in determining the rods' motion.

The simulations provide quantitative predictions of the nanomotor's swimming velocity for a given set of surface fluxes and zeta potentials. The focus of the thesis now turns to developing a more realistic reaction kinetic model for the rod that more accurately reflects the coupling between the fluxes and potentials.

Chapter 5

COUPLED MODEL

5.1 Introduction

Although the model presented in Chapter 4 captures many important details of the electrochemical locomotion mechanism, such as the direct dependence of the speed on zeta potential and reaction rate, it is unphysical in that it does not reflect the coupling that exists in a real electrochemical cell between the internal electric potential of the rod and the reaction rates. To provide an accurate, quantitative description of the system, the model must allow the reaction rates and rod potential to depend on each other, as well as on the concentrations of the reactants at the surface of the rod. To include this coupling, we remove the assumptions of piecewise constant flux and constant, prescribed surface potential that were made at the beginning of Chapter 4. Here, the boundary conditions for the reaction-driven flux are based on the Butler-Volmer expressions given in (2.42) and (2.43). They are coupled to the internal rod potential ϕ_M, which is then related to the zeta potential through the boundary condition, (2.18). Unlike in Chapter 4, the internal rod potential ϕ_M is not fixed at the beginning of the simulation; it is unknown *a priori* and determined by satisfying the current conservation constraint, (2.47).

5.2 Mathematical Model

As in the previous chapter, the rod is immersed in an aqueous solution containing hydrogen peroxide, protons, and hydroxide ions. The solution is at pH 7, with a background ion concentration of 10^{-7} mol/L, implying a Debye thickness of approximately 1 μm. The effective thickness of the Stern layer is fixed at 2 Å. Thus, the Stern layer is approximately three orders of magnitude thinner than the diffuse layer. In this case, (2.24) implies that $|\Delta\phi_S/\phi_M| \ll 1$, *i.e.* that the Stern voltage is negligible compared to the rod potential, and it is thus a reasonable approximation to set $\Delta\phi_S \approx 0$. Thus, for low electrolyte concentrations, (2.18) reduces to a simple

Dirichlet boundary condition on the potential,

$$\zeta = \phi_M. \tag{5.1}$$

The internal rod potential ϕ_M is determined iteratively by satisfying the current conservation constraint, Eq. (2.47). Also, since the Stern voltage is negligible, the exponential terms in the reaction kinetic expressions (2.42) and (2.43) are approximately equal to unity. The reaction rate equations used in this chapter are thus

$$j_{anode} = K_{O,anode} C_{H_2O_2}, \tag{5.2}$$

$$j_{cathode} = K_{R,cathode} C_{H_2O_2} C_+^2. \tag{5.3}$$

These expressions essentially model the electrochemical processes on the anode and cathode as simple chemical rate processes and are similar to those used by Chang & Jaffé [13].

5.3 Results and Discussion

Figure 5.1 shows the distributions of dimensionless proton concentration (a,d,g), electric potential and electric field streamlines (b,e,h), and charge density (c,f,i) for three cases: no peroxide (a,b,c); peroxide concentrated at 0.75 mol/L (d,e,f); and peroxide at 1.5 mol/L (g,h,i). To facilitate comparisons among the cases, the contour values for each variable are the same at each peroxide concentration. The concentration and potential have been non-dimensionalized as before, according to

$$\tilde{C}_+ = \frac{C_+ - C_{+,\infty}}{C_{+,\infty}}, \tag{5.4}$$

$$\tilde{\phi} = \frac{\phi F}{RT}. \tag{5.5}$$

In this case, the dimensionless charge density is defined in terms of the zeta potential of the rod, according to

$$\tilde{\rho}_e = \frac{\rho_e \lambda_D^2}{\varepsilon \zeta}. \tag{5.6}$$

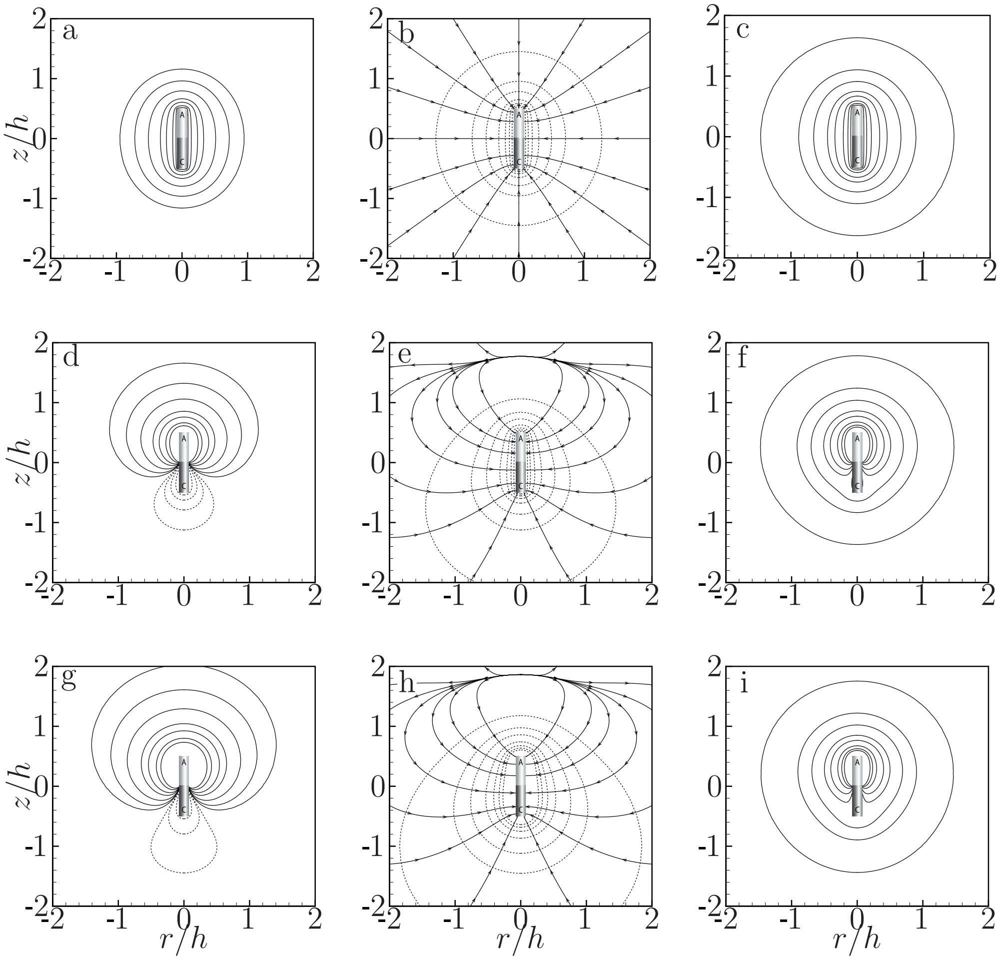

Figure 5.1: Plots created using the modified Butler-Volmer kinetic model. Contours of dimensionless proton concentration, dimensionless potential and electric field streamlines, and dimensionless charge density are shown for three separate cases. Top row: no peroxide, $\zeta = -15.25$ mV; middle row: $C_{H2O2,\infty}$ =0.75 mol/L, $\zeta = -15.25$ mV; bottom row: $C_{H2O2,\infty}$ =1.5 mol/L, $\zeta = -32.15$ mV. For each case, the contour values plotted for concentration are: $\tilde{C}_+$ =0.025, 0.05, 0.1, 0.2, 0.3, 0.5, 0.7; in (d) and (g), negative contours have been added corresponding to -0.025, -0.05, -0.1 and -0.2. For each case, the potential contour values are $\tilde{\phi} = -0.5$, -0.4, -0.3, -0.2, -0.1, -0.05, -0.01. Finally, for each case, the charge density contour values are $\tilde{\rho}_e$ = 0.01, 0.05, 0.1, 0.2, 0.3, 0.5, 0.7, 0.9. All contour values increase in absolute value with decreasing distance to the rod surface. For the contours, dashed lines indicate negative values.

We emphasize that here ζ is not a constant, but depends on the peroxide concentration and is determined from the internal rod potential ϕ_M (see (5.1)), which in turn is determined by satisfying the current conservation constraint, (2.47). Without reactions, there are no surface proton fluxes; in this case (2.47) is trivially satisfied, and any value of the rod potential gives closure to the problem. In Figs. 5.1 (a-c) we have set the rod potential to -15.25 mV, to facilitate comparison with (d-f), in which the zeta potential is determined from the kinetic expressions and current conservation to be -15.25 mV. In (g-i), where peroxide is set to 1.5 mol/L, the simulation-determined zeta potential is -32.15 mV.

In Figs. 5.1 (a-c), the peroxide concentration is zero, and thus there is no reaction-driven flux. Since the rod is negatively charged, the diffuse layer surrounding it carries a net positive charge. Since the rod zeta potential is uniform, the distributions of proton concentration, electric potential, and charge density are all symmetric about the rod. Without an asymmetry in charge density, there is no tangential electric field (the electric field lines are all normal to the surface in the figure), no tangential body force, and hence no net fluid motion along the axis of the rod. Without surface reactions, the rod does not move axially and the distributions of ion concentration and potential can be predicted using Gouy-Chapman theory.

When peroxide is added to the solution, the reaction-driven fluxes become finite and the resulting proton concentration is asymmetric, as shown in Figs. 5.1 (d) and (g). The dipolar proton distribution due to the reactions shown in Fig. 4.1 (a) is thus added onto the distribution due to the surface charge, Fig. 5.1 (a). As we increase the peroxide concentration from 0 in (a-c) to 0.75 mol/L in (d-f) and 1.5 mol/L in (g-i), the reaction rates increase and the asymmetry in proton concentration becomes more pronounced.

Figures 5.1 (e) and (h) show the normalized electric potential and electric field for cases with reactions. As discussed in §4.4, once again a source of electric field appears near the anode end. Unlike the case with the uncoupled model, the source does not approach the rod when the reaction rate is increased (*i.e.*, as peroxide is increased) from (e) to (h). In Fig. 4.4, the zeta potential is fixed in all cases at −10 mV. Here, when the peroxide concentration is increased from 0.75 to 1.5 mol/L, the zeta potential also increases in magnitude, strengthening the electric field due to the charged surface. Since both the reaction-driven and the surface-driven electric fields increase in strength by approximately the same proportion when peroxide is added, the apparent source of electric field does not move appreciably.

Figures 5.1 (c), (f), and (i) show how the distribution of charge density changes with peroxide concentration. Without peroxide (c), an excess of counterions symmetrically surrounds the rod, leaving only positive charge density. As peroxide concentration is increased, charge density becomes more strongly positive near the anode, where protons are being generated, and decreases in magnitude at the cathode, where they are being consumed. Since the rod is still surrounded by protons screening the negative surface charge, the charge density is only weakly negative near the cathode in Figs. 5.1 (f) and (i) compared with the uncharged case shown in Fig. 4.1 (d).

The qualitative similarity between the proton concentration plots (Figs. 5.1 (a,d,g) and (c,f,i)) indicate that the charge density distribution is strongly influenced by the proton concentration. This is shown more clearly in Fig. 5.2 which shows the dimensionless proton and hydroxide concentrations, $\tilde{C}_+$ and $\tilde{C}_-$, as a function of radial distance from the rod for several values of the hydrogen peroxide concentration. Figure 5.2 (a) shows that as peroxide concentration increases, the dimensionless proton concentration increases to several times the equilibrium value near the anode. The reactions cause a significant perturbation to the cation concentration that is of the same order as the bulk value. This suggests that a perturbation analysis based on the assumption of asymptotically small perturbations from equilibrium may not be appropriate here.

Figure 5.2 shows that as peroxide concentration increases, protons are depleted near the cathode surface. Without peroxide, the flux is zero and the proton concen-

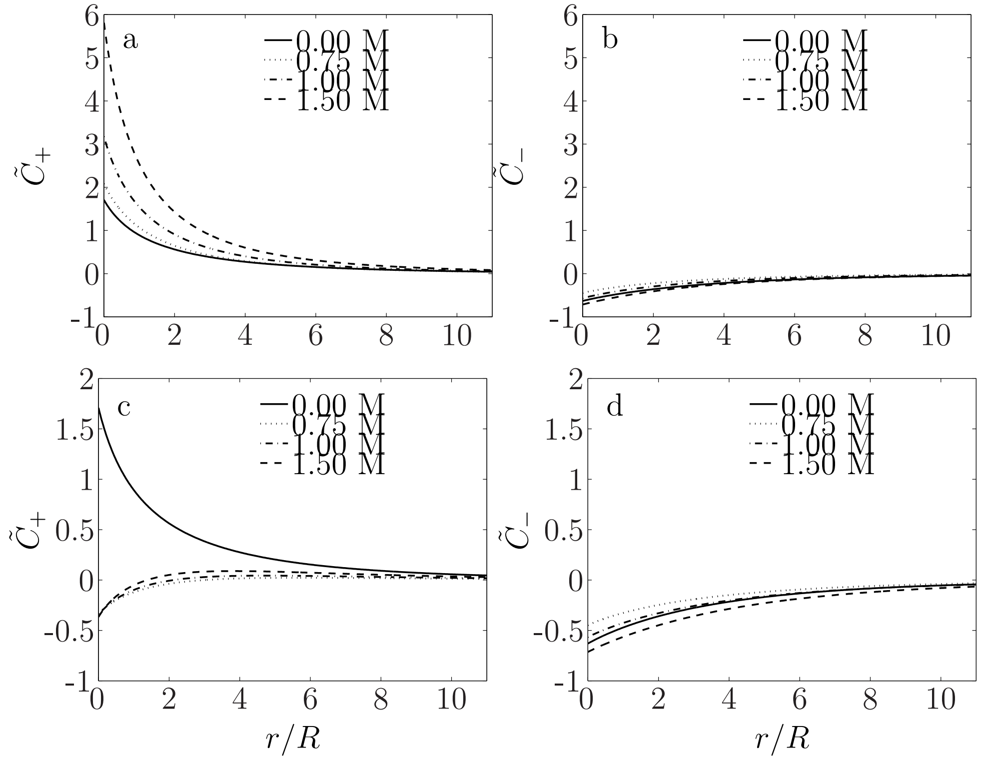

Figure 5.2: Concentrations of positive (a,c) and negative ions (b,d) as a function of radial distance (normalized by the radius of the rod, $R = 150$ nm) from the anode (a,b) and cathode (c,d) surfaces for the hydrogen peroxide concentrations indicated in the legend (units of mol/L). The figures demonstrate that the cation concentration varies much more strongly with flux than anion concentration. For the curves corresponding to zero peroxide concentration, the zeta potential is set to -25.6 mV (the thermal voltage). For the curves corresponding to finite peroxide, the zeta potential is variable and determined from the current conservation constraint, (2.47); The zeta potential varies in these cases from -15.25 to -32.15 mV.

tration is elevated above the equilibrium value due in order to screen the negatively charged surface, as indicated by the solid line. At higher peroxide concentrations, and therefore higher fluxes, protons are consumed more rapidly and proton concentration dips below the equilibrium value at the cathode. Figures 5.2 (b) and (d) show that anion concentration varies negligibly with proton flux. Since anions do not participate in the electrochemical reactions and their flux is set to zero, the anion concentration follows a Boltzmann distribution. The slight variations in anion concentration profiles with peroxide concentration in Figs. (b) and (d) are attributed to the variations of surface potential due to the varying proton flux (see Figs. 5.1 (b,e,h). These variations in potential affect the anion distribution through the Boltzmann dependence of the anion concentration on electric potential. Figures 5.2 (a-d) indicate that proton concentration varies much more widely throughout the simulations than the hydroxide ion concentration, showing that the charge density in the fluid depends much more strongly on the proton concentration than the hydroxide ion concentration. Variations in proton concentration lead to similar variations in charge density.

The asymmetries in proton concentration and charge density are dipolar in nature. Figure 5.3 shows the z-component of the self-generated electric dipole moment vector about the center of the rod as a function of peroxide concentration. The dipole moment is determined by performing the following integral numerically throughout the simulation domain:

$$\mathbf{p}(\mathbf{r}_{center}) = \int_V \rho_e(\mathbf{r})(\mathbf{r} - \mathbf{r}_{center})dV, \tag{5.7}$$

where $\mathbf{p}$ is the electric dipole moment vector (about the center of the rod), $\mathbf{r}$ is an arbitrary position vector within the simulation domain V, and $\mathbf{r}_{center}$ is the position vector corresponding to the very center of the rod [48, 40]. The figure indicates that the induced electrical dipole strength increases linearly with peroxide concentration.

As in the case of the uncharged rod, §4.3, the charge density making up the elec-

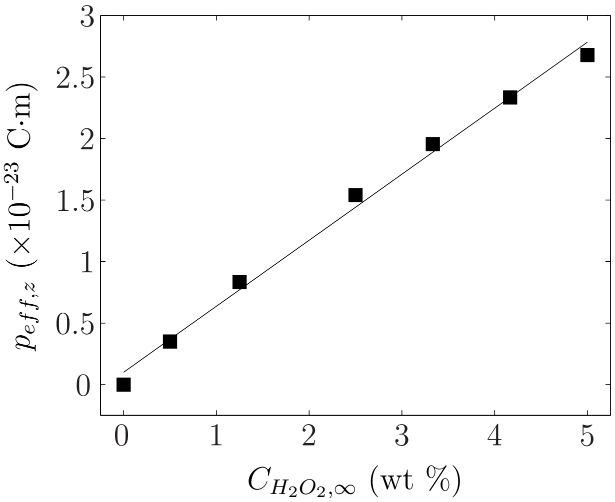

Figure 5.3: Reaction-induced electrical dipole moment (z-component) about the center of the rod as a function of hydrogen peroxide concentration.

trical dipole generates an electric field, as described by Poisson's equation, (2.11). However, with a charged rod the electric field primarily acts on the free charge in the EDL that shields the charged surface, resulting in an electrical body force and electroosmotic flow from the anode to the cathode. The flow from the anode to the cathode is equivalent, *via* a Galilean transformation, to the rod swimming through the fluid with the anode forward, as originally predicted by Paxton *et al.* [75] and verified experimentally for rods composed of several bimetallic combinations (see [98]). Protons migrate through the solution from the anode to the cathode primarily through diffusion and electromigration. As the rod moves through the solution, the gradients in proton concentration and charge density are continually re-established by the surface reactions, which inject and consume protons.

Figure 5.4 shows the velocity field surrounding the rod for the case where the peroxide concentration is set to 1.5 mol/L and the zeta potential $\zeta = -32.15$ mV. The simulations are conducted in the refrence frame of the rod. The fluid velocity at the rod surface obeys the no-slip condition and is set to zero. The fluid velocity reaches a maximum far from the rod. The velocity field has strong fore-aft symmetry,

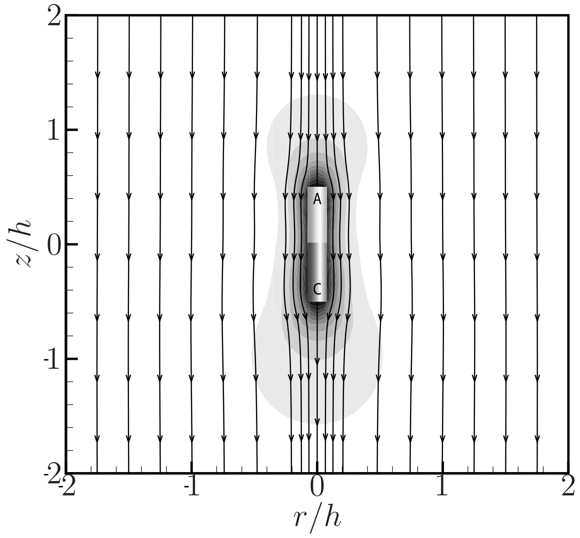

Figure 5.4: Velocity magnitude and flow streamlines for the case with $\zeta = -32.15$ mV and $C_{H2O2,\infty} = 1.5$ mol/L. Here, lighter colors indicate larger magnitudes of velocity. Note that this velocity field is computed in the reference frame of the particle. Near the surface, the velocity decays to zero, as required by the no-slip condition.

as expected for a low-Reynolds number flow. The qualitative appearance of this figure is nearly identical for other values of peroxide concentration. The reaction-induced velocity field for a rod with finite surface charge is qualitatively similar to the fields calculated for externally driven electrophoresis; at the same time, it is distinct from the case with an uncharged rod (Fig. 4.2), which shows quadrupolar flow. We use the magnitude of the fluid velocity at the far edge of the domain, where the no-stress boundary condition (2.14) is applied, as a measure of the rod's swimming speed with respect to the bulk fluid.

The observation that a charged surface is necessary for net particle motion was previously noted for induced-charge electro-osmosis and electrophoresis by Bazant & Squires [7]. They showed that a charged ideally polarizable sphere will move due to broken symmetry in the quadrupolar flow. Squires & Bazant [94] more generally examined the consequences of broken symmetries for ICEO and ICEP flows. In many cases, broken symmetries can lead to net motion or rotation of ideally polarizable particles by an induced-charge electrokinetic mechanism. Building on this idea, Catchmark *et al.* [12] fabricated an asymmetric gear-shaped particle with platinum deposited on the teeth of gold gears and showed that the particle rotates in a hydrogen peroxide solution by essentially the same electrochemical/electrokinetic mechanism as is driving the rods. In that work, the motion was attributed to a mechanism based off of gradients in interfacial tension, which was later rejected in favor of the electrochemical mechanism studied here.

Figure 5.5 shows the rod swimming speed as a function of hydrogen peroxide concentration for three data sets: (i) the simulated velocity for a rod with $\zeta = -30$ mV assuming the uncoupled model presented in §4.4; (ii) simulated velocity computed using the coupled reaction kinetic model presented in this chapter; and (iii) experimental data collected in our lab. The experimental data points represent the average velocity of between roughly 15 and 35 rods at each peroxide concentration, measured using optical microscopy. In Chapter 4, we presented the electroviscous velocity as

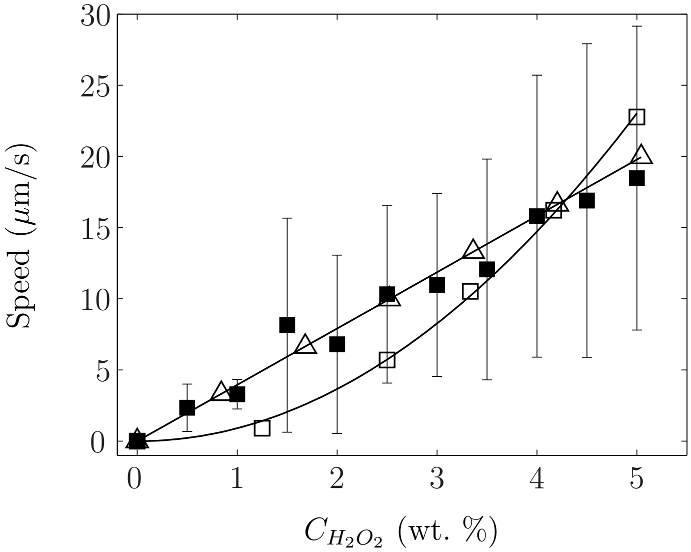

Figure 5.5: Experimentally measured rod swimming speeds (black squares) and simulated swimming speeds from the uncoupled model (open triangles) and coupled model (open squares) plotted versus bulk hydrogen peroxide concentration. In the uncoupled case, we assume a zeta potential of -30 mV and vary reaction-driven flux only, while in the coupled simulations both the flux and the zeta potential vary with peroxide concentration. The uncoupled data shows that the velocity increases linearly with the reaction flux at constant zeta potential, as predicted by equation (2.71). In the coupled case, the quadratic dependence of speed on peroxide concentration is observed due to the coupled linear dependences of U_{ev} on zeta potential and flux, also predicted by equation (2.71).

a function of proton flux instead of peroxide concentration. Here, we report one of the data sets presented previously (for a zeta potential of -30 mV) as a function of peroxide concentration instead. We determine the equivalent peroxide concentration for a given value of flux from the experimental data published in ref. [76], in which Paxton *et al.* measured the catalytically generated current density at interdigitated Pt/Au microelectrodes as a function of peroxide concentration.

The data from the uncoupled simulations and experiments suggest a linear dependence of speed on peroxide concentration. The coupled model predicts a quadratic dependence of speed on peroxide concentration. These observations can be understood by examining the scaling expression for a charged rod, (2.71), which predicts that electroviscous velocity should scale linearly with both rod zeta potential and reaction-driven flux. As hydrogen peroxide concentration increases, the reaction-driven flux increases linearly, as required by (5.2) and (5.3). However, at the same time the rod zeta potential must also vary in order to satisfy the current conservation constraint, (2.47). The rod zeta potential at which the net current into the rod is zero is also a linear function of peroxide concentration (not shown). Thus, when peroxide concentration is increased, both the zeta potential and flux increase linearly, resulting in a quadratic dependence of velocity on peroxide concentration.

Although the quadratic dependence of U_{ev} on peroxide concentration can be explained by the scaling analysis, it is not clear that the experimental data follow a quadratic trend. It is possible that the coupled kinetic model is incomplete; for example, the kinetic rate constants $K_{O,anode}$ and $K_{R,cathode}$ may decrease with increasing peroxide concentration. Here, for simplicity, we have assumed that $K_{O,anode}$ and $K_{R,cathode}$ are constants. If this effect were incorporated into the simulations, the fluxes at higher peroxide concentrations would be slightly lower, leading to a slower rod velocity and flattening the quadratic curve slightly. A more detailed kinetic model incorporating possible variations of rate constants with peroxide concentration would be a worthwhile future project.

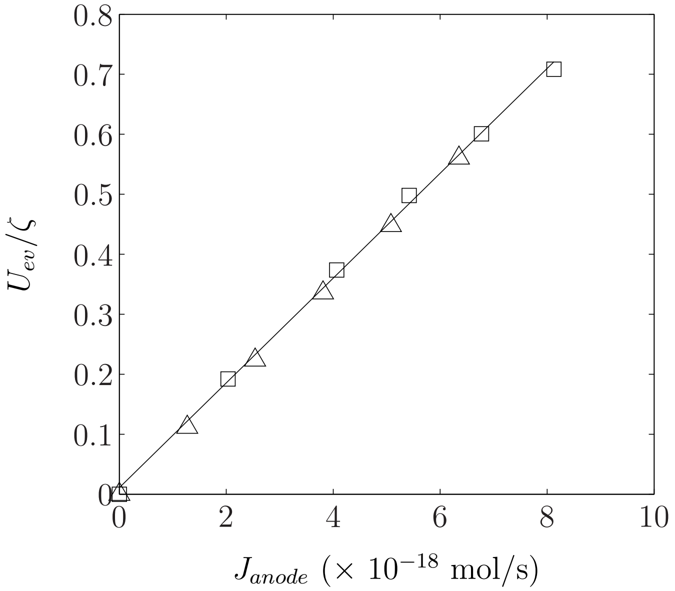

Figure 5.6: Electroviscous velocity normalized by zeta potential (units of μm/(s·mV)) as a function of total proton flux out of the anode surface J_{anode} (defined in the text) for the uncoupled simulations (open triangles) and coupled simulations (open squares). These plots support the prediction of (2.71) that the ratio of velocity to zeta potential should scale linearly with the proton flux. Also note that the slope of the uncoupled and coupled data is essentially the same; this is expected because the constants in the scaling relationship (λ_D, h, D_+, etc.) are unchanged from the uncoupled to the coupled simulations.

The agreement between the simulations and scaling analysis is more clearly illustrated by examining the relationship between the ratio U_{ev}/ζ and the flux of protons, j_+. In the coupled model, the flux j_+ varies with position, and so in Fig. 5.6 we plot U_{ev}/ζ as a function of the total flux at the anode side, J_{anode}, defined as

$$J_{anode} = \int_{anode} j_{anode} dA, \tag{5.8}$$

where j_{anode} is given by (5.2). Since the total proton flux out of the anode is equal to the total proton flux into the cathode, as dictated by the current conservation constraint, Fig. 5.6 would look identical if the variable on the abscissa were $J_{cathode}$ instead of J_{anode}. This figure shows that when the effects of varying zeta potential are removed, the linear relationship between speed and flux predicted by (2.71) is recovered. In addition, the figure shows that the two sets of simulation data collapse onto the same line when normalized by the zeta potential. Figure 5.6 illustrates that the quadratic relationship between U_{ev} and peroxide concentration observed in Fig. 5.5 is due to the variations in zeta potential with peroxide concentration.

In this work, we have neglected the native surface potential the rod my attain due to differential adsorption of ions or impurities in the solution. Dougherty *et al.* [22] measured the native surface potential of both bare and coated gold, silver, palladium and gold/silver rods in inert electrolyte solutions and showed that the values of zeta potential were almost universally negative versus the bulk and tended to become more negative with increasing pH. It is well known that the zeta potential of metal oxides is a strong function of the electrolyte ion composition (see, *e.g.*, [101, 52]). Arguably, the effective zeta potential of metal rods on which electrochemical reactions are occurring will depend both on their native charge due to differential adsorption as well as the kinetics of the reaction. Future work could focus on a model that incorporates the effects of both native and electrochemically-induced surface potentials.

Figure 5.7 shows the rod speed as a function of the reciprocal of solution viscosity at three different peroxide concentrations. The solid lines are linear fits to the

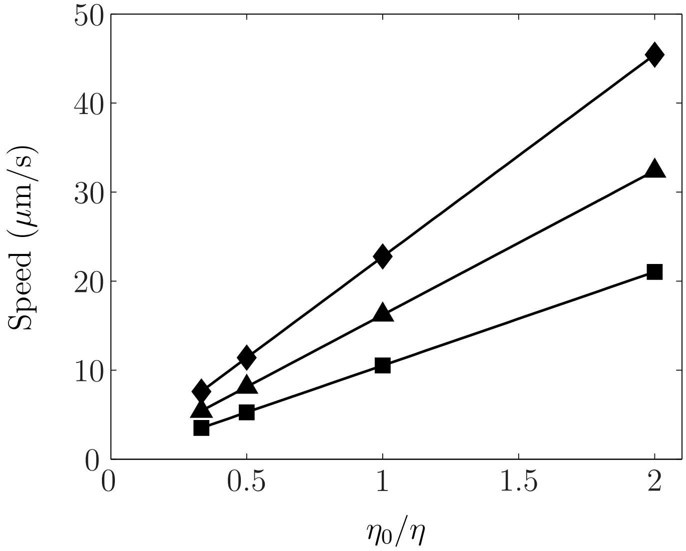

Figure 5.7: Electroviscous velocity (computed using the coupled model) as a function of reciprocal of viscosity (normalized by the viscosity of water at 25 °C, η_0) for three different peroxide concentrations: 1.5 mol/L (diamonds), 1.25 mol/L (triangles), and 1 mol/L (squares). The solid lines are linear least-squares fits to the data. These results strongly suggest that the prediction of (2.71) of an inverse dependence of electroviscous velocity on viscosity is valid.

data, confirming the inverse proportionality between speed and viscosity predicted by the definition of electroviscous velocity, (2.55), and the scaling result for a charged rod, (2.71). Solutions with higher viscosity generate viscous stresses that more efficiently dissipate electrical body forces, thus decreasing the electroviscous velocity. Balasubramanian *et al.* [4] showed that Pt/Au nanorods move faster in solutions after local heat pulses were applied, and attributed the speed increase primarily to a local decrease in viscosity due to the increase in temperature. Considering that Fig. 4.6 shows a linear relationship between speed and electrical body force, and Fig. 5.7 shows an inverse relationship between speed and viscosity, we find that the speed of the rod is driven by electrical body forces and opposed by viscous forces, as expected for an electroviscous flow and demonstrated by (2.55).

The scaling analysis makes other predictions that are confirmed by the simulations. Equation (2.71) predicts that the electroviscous velocity should increase quadratically with the Debye thickness λ_D. This suggests that longer rods and rods with thicker EDLs surrounding them should swim faster. We have also conducted simulations to verify that electroviscous velocity varies inversely with the diffusivity of the charge carriers, confirming the prediction of (2.71) of an inverse dependence of speed on cation diffusivity. Overall, we find that the scaling analysis predicts the dependence of rod velocity on these controlling parameters with great accuracy.

5.4 Conclusion

This chapter has presented governing equations, scaling analyses, and numerical simulations using the coupled reaction kinetic model presented in Chapter 2. We numerically solved the coupled Poisson-Nernst-Planck-Stokes system of equations and represent the kinetics of the electrochemical reactions with Frumkin-corrected Butler-Volmer equations in the Gouy-Chapman and Tafel regime limits. The simulation results show good agreement with scaling analyses and experimental measurements of the rods' average swimming velocity as a function of hydrogen peroxide concentration. Strong evidence has been shown that the rod movement is the result of fluid slip driven by electrical body forces generated by a coupling of free charge and the reaction-induced electric field.

One of the most important improvements to the coupled model that can be made relates to the reaction kinetic modeling. In this work we have assumed that the reactions are simple one-step processes that are first-order in the peroxide concentration and, in the case of the cathodic reaction on the anode, second-order in protons. This is likely a significant simplification of the actual kinetics of these reactions. The electrochemical decomposition of hydrogen peroxide on platinum electrodes was studied by Hall *et al.* [41]. Sabass & Seifert [84] recently considered possible decomposition pathways for the anodic and cathodic reactions, and argued that both could be considered linear in peroxide as a first approximation.

The following chapter will discuss investigations into the dependence of rod velocity on background electrolyte concentration. Several papers suggest that the rod's velocity decreases with increasing background electrolyte concentration (excluding silver ions [50]), *e.g.* [76]. In addition, an improved understanding of the impact of changing the geometry of the nanomotors may yield improved engineered designs for practical nanomotors, capable of generating greater swimming speeds and forces.

Chapter 6

ROLE OF SOLUTION CONDUCTIVITY IN ELECTROKINETIC LOCOMOTION

6.1 Introduction

The previous chapters of this thesis have shown that the self-propulsion of bimetallic rods arises from a complex interaction between the reaction- and surface-induced space charge distributions and the electric fields they create. In this chapter, we turn our attention to assessing the performance of the rods in practical situations. In particular, we wish to understand fully the physical reasons for the significant decrease in speed that is observed when electrolyte is added to the hydrogen peroxide solution.

Paxton *et al.* [76] measured the speed of platinum/gold (Pt/Au) rods with varying concentrations of sodium nitrate ($NaNO_3$) and lithium nitrate ($LiNO_3$) added to a 3.7 wt. % hydrogen peroxide solution. By observing the variation in speed at conductivities ranging from 8.8 to 410 μS/cm, they found a roughly inverse relationship between speed and conductivity. They argued, as have several works before them [2, 57, 75], that the swimming speed of a self-electrophoretic swimmer is given by the Helmholtz-Smoluchowski equation,

$$U = \mu_e E_0, \tag{6.1}$$

where μ_e is the swimmer's electrophoretic mobility and E_0 is a characteristic magnitude of the self-generated electric field. Paxton *et al.* assumed the electric field is given according to Ohm's law, $E_0 = i/\sigma$, where i is the current density in the fluid due to the electrochemical reactions and σ is the electrical conductivity of the solution. Substituting Ohm's law into (6.1),

$$U = \frac{\mu_e i}{\sigma}. \tag{6.2}$$

Note the similarity between (6.2) and the formula for a self-electrophoretic cell derived by Anderson 16 years earlier, (1.14); the only major difference between the two is that in Anderson's model, the swimmer required an external concentration gradient in order to generate a propulsive electric field. Both equations imply that speed is inversely related to solution conductivity, if mobility and current density are constant. The experimental data of Paxton *et al.* appear to agree with the prediction of an inverse dependence on conductivity; however the agreement is not perfect. This suggests that the mobility and current density do not necessarily remain constant as conductivity is increased.

Although [76] established definitively that the speed and conductivity are roughly inversely related, not all electrolytes cause a decrease in rod swimming speed when added to the peroxide solution. Kagan *et al.* [50] showed that the presence of electrolytes containing silver ions (Ag^+) in the peroxide solution does not decrease the speed but instead increases the speed of Pt/Au rods by roughly an order of magnitude. This unusual result was attributed to deposition of Ag^+ ions on the Au surface, which are then reduced in the presence of hydrogen peroxide. While this mechanism has not been rigorously investigated, it appears that there is at least one exception to the inverse relationship between speed and conductivity. Nevertheless, in this work we do not consider salts containing silver ions and focus on electrolytes that are known to lead to a decrease in swimming speed.

In addition to experimental works, the dependence of self-electrophoretic swimming on conductivity has been predicted analytically. Golestanian *et al.* [38] derived formulae for the steady-state speed of several different phoretic swimmers, one of which was a Janus cylinder similar to the Pt/Au rods considered here. Their result for the speed of the cylinder is (their equation (16))

$$U = \frac{1}{4\sigma}\left(\frac{R}{L}\right)\ln\left(\frac{L}{4R}\right)\left(\mu_+\alpha_- - \mu_-\alpha_+\right), \tag{6.3}$$

where R is the radius of the rod, L is the half-length, μ is the electrophoretic mobility, α is the reaction-driven surface current density, and subscripts denote the forward $(+)$ and backward $(-)$ ends of the rod.

For a rod with a uniform mobility ($\mu_+ = \mu_- = \mu$) and piecewise constant current density ($\alpha_+ = -\alpha_- = \alpha$), (6.3) simplifies to

$$U = -\frac{R}{2L}\ln\left(\frac{L}{4R}\right)\frac{\alpha\mu}{\sigma}. \tag{6.4}$$

Since the current density in the diffuse layer, i, scales as the surface current density α, the final grouping of terms $\alpha\mu/\sigma$ in (6.4) is proportional to the right-hand side of (6.2). The two expressions differ only by the geometrical corrections in (6.4) that account for the non-spherical swimmer geometry.

In this chapter, we will modify the coupled model from Chapter 5 to include variations in the solution conductivity. We begin our analysis by revisiting the mathematical model developed in Chapter 2, and note some necessary modifications that are made. We then present the results of simulations of bimetallic rods in hydrogen peroxide in the presence of several different electrolytes. The simulations solve the full Poisson-Nernst-Planck-Stokes equations with multiple ionic species and use nonlinear Butler-Volmer boundary conditions to represent the electrochemical reactions. The model also accounts for the presence of dissolved atmospheric carbon dioxide (CO_2) and its contribution to the overall ion concentration. We use three different monovalent electrolytes (potassium chloride (KCl), lithium nitrate ($LiNO_3$), and sodium nitrate ($NaNO_3$) to vary the solution conductivity and show the differences in results for each electrolyte. We compare the simulation results to the experimental and analytical results discussed above, as well as to the scaling analysis derived in Chapter 2, which predicts the dependence of swimming speed and Stern voltage on solution conductivity (through the quadratic dependence of speed on Debye length). The long-term goal of this work is to determine whether the decrease in speed with conductivity is inherent to the electrokinetic propulsion mechanism, or if there may be some means to allow bimetallic rods to function in conductive media.

6.2 Modifications to the Mathematical Model

The mathematical model for the simulations presented in this chapter is largely unchanged from that presented in Chapter 2. The distributions of species concentration, electric potential, and fluid velocity are again given by the advection-diffusion (2.8), Poisson (2.11), and fluid continuity and momentum equations (2.12,2.13), respectively. The conditions at the far boundary (on the opposite side of the domain from the rod) are unchanged from those presented in §2.4, and the no-slip condition is again applied to the rod surface. Below we discuss the modifications to the model that are necessary in order to account for all contributions to solution conductivity, as well as account for the effect of increasing conductivity on the surface boundary conditions for the reactions and electric potential.

6.2.1 Carbonic Acid

Carbonic acid is formed when atmospheric carbon dioxide (CO_2) dissolves in water. The gas dissolution equilibrium is expressed by

$$\mathrm{CO_2}(g) \rightleftharpoons \mathrm{CO_2}(aq). \tag{6.5}$$

The dissolved gas concentration is determined from Henry's law, $[\mathrm{CO_2}(aq)] = p_{CO_2}/k_H$, where p_{CO_2} is the partial pressure of carbon dioxide above the solution and the Henry constant $k_H = 29.41$ atm/(mol/L) at room temperature. The dissolved CO_2 forms an equilibrium with carbonic acid (H_2CO_3):

$$\mathrm{CO_2}(aq) + \mathrm{H_2O} \rightleftharpoons \mathrm{H_2CO_3}(aq). \tag{6.6}$$

The equilibrium constant for the hydration of carbon dioxide is $K_h = [\mathrm{H_2CO_3}]/[\mathrm{CO_2}] = 1.7 \times 10^{-3}$ for water. The dissolution of the acid introduces protons (H^+) as well as bicarbonate (HCO_3^-) and carbonate (CO_3^{2-}) anions into the solution, in addition to the protons and hydroxide ions (OH^-) already present due to the self-ionization of water. The presence of the dissolved acid adds to the total ion concentration, and thus increases the conductivity of the solution.

We track the concentration of dissolved carbonic acid in the simulations. Since it is diprotic, carbonic acid is capable of dissociating twice: first, it produces a proton and a bicarbonate anion, HCO_3^-, according to

$$H_2CO_3 \rightleftharpoons H^+ + HCO_3^-, \quad pK_a = 3.6. \tag{6.7}$$

The bicarbonate ion may then further dissociate, producing another proton and a carbonate ion, CO_3^{2-}:

$$HCO_3^- \rightleftharpoons H^+ + CO_3^{2-}, \quad pK_a = 10.329. \tag{6.8}$$

In addition, water self-ionizes into protons and hydroxide ions, according to

$$H_2O \rightleftharpoons H^+ + OH^-, \quad pK_w = 14. \tag{6.9}$$

Finally, the bulk solution must be electrically neutral,

$$\sum_i z_i C_{i,\infty} = 0. \tag{6.10}$$

The equilibrium equations corresponding to reactions (6.5)-(6.9), along with (6.10), constitute six equations for the six unknown concentrations of CO_2, H_2CO_3, H^+, OH^-, HCO_3^-, and CO_3^{2-}. Analytical and numerical solutions (the latter with MinEQL+ software) of these six equations show that for a pH of approximately 6, the concentrations of CO_3^{2-} and OH^- are negligible compared to the concentration of HCO_3^-, and the system may thus be treated as a binary electrolyte with equal concentrations of H^+ and HCO_3^-. Here, the background concentrations of H^+ and HCO_3^- are set to 9×10^{-7} mol/L, implying a pH of 6.05. Although the omission of hydroxide and carbonate ions may cause some error in the swimming speed, we assume that this error is negligible due the similarity in mobilities between these ions and bicarbonate (see table 6.1).

6.2.2 Stern-layer Voltage

Due to the greater ionic strengths considered in this chapter, the diffuse layer around the rod in these cases is thinner than those considered in Chapters 4 and 5. Since the Stern layer thickness is kept constant at 2 Å, the ratio λ_S/λ_D increases with solution conductivity and therefore (2.24) implies that the Stern voltage becomes more significant in comparison to the rod potential as conductivity is increased. Thus, here we do not assume a negligible Stern voltage and use the full Frumkin-Butler-Volmer equations, (2.42) and (2.43), to describe the kinetics of the electrochemical reactions. Additionally, to account for the effect of the Stern voltage on the zeta potential distribution, we use the full mixed boundary condition for the potential, equation (2.18). We thus remove the assumptions made in §5.2 of a spatially uniform zeta potential (see (5.1) and Chang-Jaffé kinetic expressions (5.2,5.3) for the reactions.

6.2.3 Flux Weighting

In general, the flux expressions for the anode and cathode are not equal at the junction between them, located at $z = 0$. To avoid problematic discontinuities in the reaction flux and flux gradient, we multiply the entire flux profile along the length of the rod by a sigmoidal dimensionless weighting function, $\xi(z)$, defined as

$$\xi(z) = \left| \frac{2}{1 + e^{-\gamma z}} - 1 \right|, \tag{6.11}$$

where $\gamma = 10^7$ m^{-1} and z is in meters. The weighting function has the effect of reducing the reaction rates close to the intersection between anode and cathode. For a real rod, the junction between the anode and cathode is likely somewhat jagged, and as a result the density of available reaction sites is not as high as on the rest of the rod. Additionally, the concentration of protons near the Pt/Au junction may lead to unphysically high fluxes on the cathode, which would be slightly reduced as a result of the use of the weighting function.

6.2.4 Constants and Dimensionless Parameters

Table 6.1 shows the relevant constants used in the simulations. Since the conductivity of a solution is a function of ion mobilities, different concentrations are required for different electrolytes to achieve the same value of conductivity. As in previous chapters, the rate constants $K_{O,anode}$ and $K_{R,cathode}$ are fitting parameters. We chose values of $K_{O,anode}$ and $K_{R,cathode}$ so that the simulated swimming speed at a conductivity of 8.8 μS/cm (assuming KCl is the background electrolyte) matches the speed measured by Paxton *et al.* [76] at the same conductivity. In this chapter, $K_{O,anode}$ is almost two orders of magnitude larger than in Chapter 5. This change is necessary in order to produce a swimming speed (with current conservation (2.47) satisfied) of 22 μm/s at a conductivity of 8.8 μS/cm. In the cases without electrolyte, the simulations needed to produce roughly the same swimming speed (approximately 20 μm/s), but at a peroxide concentration of 5 wt. % (instead of the 3.7 wt. % considered in this chapter) and with only H^+ and OH^- in the system, instead of KCl and bicarbonate ions; in other words, in the previous work the simulations needed to produce the same swimming speed at a lower conductivity. As a result, a lower rate constant was required than in the current case. Considering that the model in this chapter incorporates more physical phenomena than in previous chapters, it is likely that the value of $K_{O,anode}$ considered in this chapter is closer to the true value.

Once again, we wish to estimate the relative importance of different transport mechanisms in the system. Table 6.2 shows the results of the computations of the same dimensionless parameters computed in Chapter 2 for the cases with varying conductivity: the electric Rayleigh number, which tells the relative importance of electroconvection and diffusion in transporting protons in the system; the parameter β, which tells the relative importance of electromigration and diffusion; and the Damköhler number, which relates reaction- and diffusion-driven transport. As before, we calculate approximations to these three parameters by numerically integrating the

Constant	Description	Value
$K_{O,anode}$	Oxidation rate constant, anode	2.2×10^{-7} m s^{-1}
$K_{R,cathode}$	Reduction rate constant, cathode	1 m^7 s^{-1} mol^{-2}
D_+	Diffusivity, protons	9.311×10^{-9} m^2 s^{-1}
D_-	Diffusivity, bicarbonate ions	5.273×10^{-9} m^2 s^{-1}
$D_{H_2O_2}$	Diffusivity, hydrogen peroxide	6.6×10^{-10} m^2 s^{-1}
D_{O_2}	Diffusivity, molecular oxygen	2×10^{-9} m^2 s^{-1}
D_{Li^+}	Diffusivity, lithium ion	1.029×10^{-9} m^2 s^{-1}
D_{Na^+}	Diffusivity, sodium ion	1.334×10^{-9} m^2 s^{-1}
D_{K^+}	Diffusivity, potassium ion	1.957×10^{-9} m^2 s^{-1}
$D_{NO_3^-}$	Diffusivity, nitrate ion	1.902×10^{-9} m^2 s^{-1}
D_{Cl^-}	Diffusivity, chloride ion	2.032×10^{-9} m^2 s^{-1}
η	Solution viscosity	8.9×10^{-4} Pa s
ρ	Solution density	998 kg m^{-3}
$C_{\pm,\infty}$	Bulk concentration, protons and bicarbonate ions	9×10^{-7} mol L^{-1}
$C_{O_2,\infty}$	Bulk concentration, molecular oxygen	0.2×10^{-3} mol L^{-1}
$C_{H_2O_2,\infty}$	Bulk concentration, hydrogen peroxide	1.11 mol L^{-1}
ε_r	Solution dielectric constant	78.4
λ_S	Effective Stern layer thickness	0.2 nm

Table 6.1: Values of relevant constants used in the simulations. The mobilities of the charged species are given by the Nernst-Einstein relation, $\nu_i = D_i/RT$, where R is the ideal gas constant and $T = 298.15$ K. The bulk electrolyte concentration is not shown because it is varied throughout the work between 56.4 and 820 μmol/L. The rate constants, $K_{O,anode}$ and $K_{R,cathode}$, are fitting parameters and are chosen to yield a swimming speed approximately equal to that observed by Paxton *et al.* [76] at a conductivity of 8.8 μS/cm.

	8.8 μS/cm	**35 μS/cm**
Ra_e	0.777	0.172
Da	0.585	0.5633
β	0.0073	0.0024

Table 6.2: Calculated and estimated values of the Rayleigh and Damköhler numbers, as well as the parameter β, for two different salt concentrations. In the first case, KCl has been added at a concentration of 56.4 μmol/L; in the second, KCl concentration is 231 μmol/L. All parameters were estimated using the same numerical method reported in Chapter 2. The values of the parameters indicate that the majority of proton transport in the system is due to diffusion.

diffusion-, electromigration-, convection-, and reaction-driven fluxes over the system geometry and computing the relevant ratios. The total reaction-driven flux of protons is given by the integral of the reaction-driven flux j_+ over the anode surface. The total diffusive, convective and electromigration fluxes of protons through the fluid are estimated by integrating the z-components of the appropriate local fluxes over the two-dimensional annular disk surrounding the middle of the rod and extending from the rod surface to the boundary of the simulation domain.

The values of the parameters in table 6.2 indicate that protons are transported primarily by diffusion, more than by electromigration and much more than by convection. This is likely due to the much higher fluxes of protons considered in this chapter compared to the previous chapter, considering that the rate constant on the anode is two orders of magnitude higher (see above). As a result, protons are produced more rapidly in these cases, resulting in high proton concentrations near the anode and extremely sharp concentration gradients at the junction between the anode and cathode, where the dimensionless parameters in table 6.2 are evaluated. These sharp concentration gradients, in turn, lead to larger diffusive fluxes.

6.3 Results and Discussion

In this section we present the results of simulations for three monovalent electrolytes at different concentrations. In all cases, the bulk hydrogen peroxide concentration is fixed at 1.11 mol/L. By varying electrolyte concentration, we observe the variation in the proton concentration, electric potential, electric field, and velocity distributions. We compare our results for the swimming speed to previous analytical and experimental results.

Figure 6.1 shows the fluid velocity magnitude (color) and flow streamlines for cases without (a) and with salt (b). Figure (a) is for a simple case with only peroxide, oxygen, protons, and bicarbonate ions. As stated above, the bulk concentration of protons and bicarbonate ions is 0.9 μmol/L, resulting in a conductivity of 0.35 μS/cm. In (b), KCl has been added at a concentration of 56.4 μmol/L, yielding a bulk conductivity of 8.8 μS/cm, which is the lowest conductivity considered by Paxton *et al.* [76].

Since the color scales are the same in these two figures (with red indicating high and blue indicating low fluid speed), it is clear that the speed of the rod is significantly reduced in the salt case. In both cases, a region of high fluid velocity magnitude is clearly visible near the equator of the rod. These high-speed regions appear because of the extremely strong charge density and electric fields near the rod. The strong charge density in the diffuse layer, which arises to screen the surface charge scales inversely with the square of Debye length; thus, as salt is added to the solution, the diffuse layer shrinks, dramatically increasing the charge density in the diffuse layer. This strong charge density couples with the z-direction electric field, which is especially strong in this region due to the large gradient in charge density, to produce electrical body forces on the order of 10^7 N/m^3 in the vicinity of the rod. These especially strong body forces are responsible for the regions of high fluid speed in Figs. 6.1 (a)

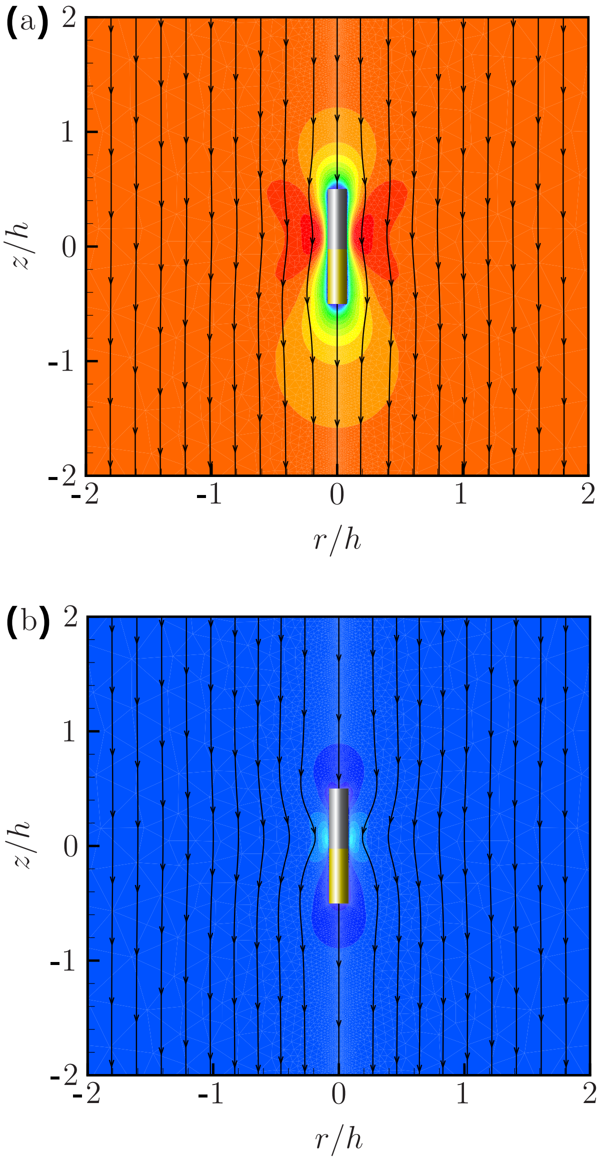

Figure 6.1: Simulation-generated plots of velocity field (color) and flow streamlines. (a) $[\mathrm{H}^+] = [\mathrm{HCO}_3^-] = 0.9$ μmol/L, no electrolyte, implying a conductivity of 0.35 μS/cm. (b) $[\mathrm{H}^+] = [\mathrm{HCO}_3^-] = 0.9$ μmol/L, $[\mathrm{K}^+] = [\mathrm{Cl}^-] = 56.4$ μmol/L, implying a conductivity of 8.8 μS/cm. Color scale is the same for both plots, indicating that the fluid velocity (and thus particle velocity) is significantly reduced in case (b).

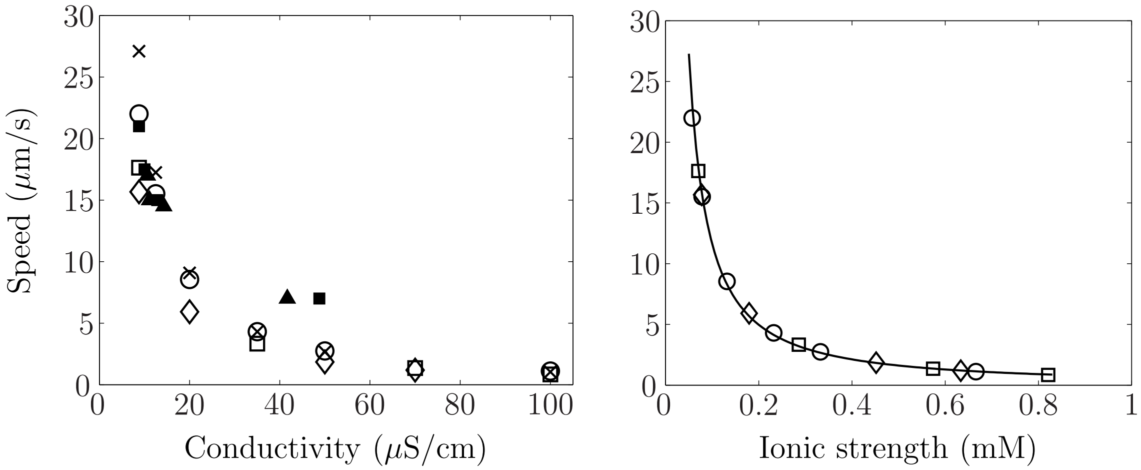

Figure 6.2: (left) Axial swimming speed versus solution conductivity in 3.7 wt. % H_2O_2 for experiments, theory, and computations. Open symbols indicate current computational work, with KCl (circles), $NaNO_3$ (squares) and $LiNO_3$ (diamonds) as the background electrolyte. Experimental data for $NaNO_3$ (black squares) and $LiNO_3$ (black triangles) is taken from Paxton *et al.* [76]. × symbols indicate data from the equation derived by Golestanian et al. [38], equation (6.3), with values for the phoretic mobility, surface activity, and conductivity taken from our simulation data. (right) The same simulation data plotted versus ionic strength. The data sets collapse onto a single curve, suggesting a direct correlation between ionic strength and swimming speed. The solid line is a fit curve, showing $U_{ev} \propto I^{-1.228}$.

and (b), which become more prominent as salt concentration is increased.[1]

Near the center of Fig. 6.1 (b), the flow streamlines bend inward toward the rod. This bending occurs due to the aforementioned increase in flow speed near the rod surface. The contraction of the streamlines near the rod surface is a natural consequence of mass continuity, satisfying the requirement for incompressible flows that the volume flow rate between two adjacent streamlines must be constant.

---

[1] According to the simulations, the magnitude of electric field in the diffuse layer is on the order of 10^7 V/m. With fields this strong, it is possible that water molecules near the rod surface may be polarized to such an extent as to lower the dielectric constant of the fluid. This would result in an overall decrease in the electric field strength near the rod. As a result, the actual electric field may be slightly weaker than predicted by the simulations. The local increase in fluid velocity predicted by Figs. 6.1 (a) and (b) would be extremely difficult to measure in reality. The swimming speed is still determined by measuring the fluid velocity on the outer edge of the simulation domain.

The simulations depicted in Fig. 6.1 were run for conductivities between 8.8 and 410 μS/cm, the same range studied experimentally by Paxton *et al.* [76]. Figure 6.2 (a) shows the variation in rod swimming speed with solution conductivity for the simulations with added KCl, $NaNO_3$ and $LiNO_3$; the experimental data from [76], with $NaNO_3$ and $LiNO_3$ as the background electrolytes; and the predictions of (6.4), with values of the surface activity α and phoretic mobility μ at a given conductivity determined by the simulations. The results of the simulations and experiments are comparable at low conductivity because the values of the rate constants $K_{O,anode}$ and $K_{r,cathode}$ were chosen to yield identical values at 8.8 μS/cm. Figure 6.2 (a) shows that the simulations reproduce the same trend of speed vs. conductivity that is observed experimentally.

Equation (6.4) requires the surface activity α, phoretic mobility μ, and conductivity σ as inputs; for a given value of conductivity, we use the area-averaged zeta potential (determined from the simulations) to calculate the electrophoretic mobility from $\mu_e = \varepsilon\zeta/\eta$, and the area-averaged current density out of the anode (also determined from the simulations) as the surface activity. The agreement between the simulations and (6.4) is generally excellent, especially at high conductivities. At low conductivities, (6.4) overpredicts the swimming speed by a margin that increases as conductivity decreases. We attribute this deviation to the assumption of equation (6.4) that the diffuse layer is infinitely thin, which becomes less accurate as conductivity is decreased and the diffuse-layer thickness becomes finite.

The scaling analysis result for a charged rod, (2.71), predicts a quadratic relationship between speed and Debye length. The same relationship was also derived by Sabass and Seifert [84] (see their equation (33)). Figure 6.3 shows the same swimming speed data shown in Fig. 6.2 as a function of Debye length. The near-perfect agreement between the simulation data and the prediction of the scaling analysis (shown as a quadratic fitting curve) again suggests that the swimming speed is fundamentally related to the solution ionic strength (since Debye length is inversely proportional to

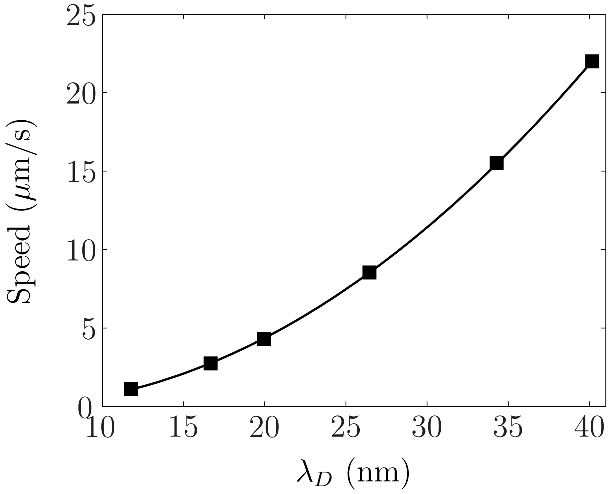

Figure 6.3: Swimming speed data visualized in figure 6.2 plotted versus Debye length, varied by tuning the concentration of KCl. Black squares indicate simulation data, while the solid line is a quadratic least-squares fit.

the square root of ionic strength; see (2.21)), rather than the conductivity.

Given the results of Figs. 6.2 and 6.3, it is not clear from Fig. 6.2 (a) that conductivity is the fundamental parameter which controls the swimming speed. If the same conductivity is achieved with two different salts, the swimming speeds are generally different. Due to differences in ionic mobility, different salt concentrations are required for different salts to achieve a given value of conductivity. Figure 6.2 (b) shows the same simulation data as Fig. 6.2 (a), plotted versus ionic strength. For solutions at infinite dilution, conductivity σ and ionic strength I are calculated from

$$\sigma = \sum_i z_i^2 \Lambda_i C_i, \tag{6.12}$$

$$I = \frac{1}{2} \sum_i z_i^2 C_i, \tag{6.13}$$

where Λ is the molar conductivity of ion i. Ionic strength thus differs from conductivity in that the mobilities of the ions are not considered. Figure 6.2 (b) shows that the three data sets collapse onto the same curve when plotted versus ionic strength, suggesting that speed and ionic strength are inversely correlated. We are not aware of any other works that distinguish the dependence of rod speed on ionic strength from the dependence on solution conductivity. As will be demonstrated below, the simulations also suggest that rod potential is also inversely correlated with ionic strength.

Several previous analyses, including our own, predict a linear relationship (proportional to the Helmholtz-Smoluchowski equation) between the surface charge on a self-electrophoretic swimmer and its swimming speed. Examples include the work of Lammert *et al.* [57], Paxton *et al.* [75, 76], Golestanian *et al.* [38], Sabass and Seifert [84], and Chapters 4 and 5 of this thesis. Here, we again observe a strong correlation between speed and surface potential. Figures 6.4 (a) and (b) show the variation in area-averaged zeta potential with conductivity and ionic strength, respectively, similar to Figs. 6.2 (a) and (b). When electrolyte is added to the system, the reaction rates are affected asymmetrically, requiring the rod potential to become less negative in order to satisfy current conservation. Thus, the rod potential, and hence the zeta potential, become less negative in response to an increase in conductivity.

Figure 6.5 shows the z-direction electric field E_{50} measured at the junction between the anode and cathode, 50 nm from the rod surface, and the characteristic electric field E^* defined in Chapter 2 (see (2.63)), as a function of solution conductivity. Since it is measured roughly one Debye length away from the surface, E_{50} is an estimate of the electric field driving the electroviscous flow and nanorod motion. However, the electric field varies significantly with position throughout the simulation domain, and is significantly more complicated than the relatively uniform electric field applied for conventional electrophoresis. To get an idea of how the electric field distribution varies as a whole, we focus our attention on the variation of E^* with respect to conductivity. Recall that E^* is defined as the external electric field required to drive conventional electrophoresis of the particle at a speed equal to the observed swimming speed of the rod:

$$E^* = \frac{\eta}{\varepsilon\zeta} U_{ev}, \tag{6.14}$$

where here U_{ev} is the observed swimming speed of the rod. E^* is thus indicative of

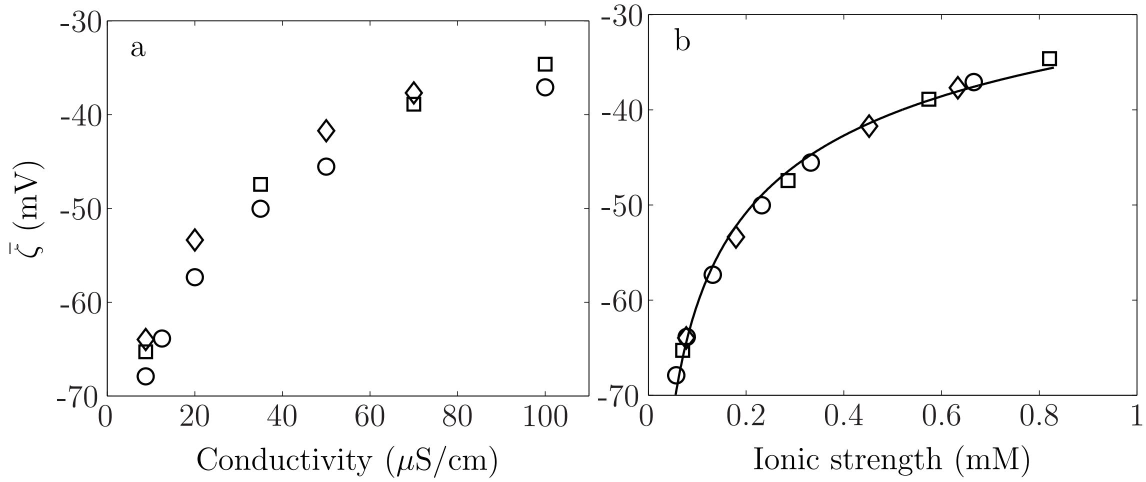

Figure 6.4: Area-averaged zeta potential as a function of solution conductivity for three different electrolytes: KCl (circles), $NaNO_3$ (open squares), and $LiNO_3$ (open diamonds). (b) The same zeta potential data as in (a) as a function of ionic strength. As with the swimming speed, the data collapse onto a single curve, indicating the direct correlation between zeta potential and ionic strength. Close examination of this figure and of Fig. 6.2 reveals that differences in speed between different electrolytes at the same conductivity are correlated with the same differences in zeta potential. These plots together suggest a direct correlation between rod potential and swimming speed.

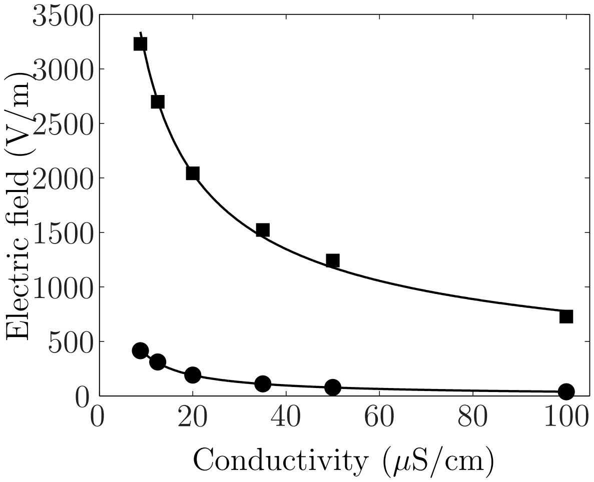

Figure 6.5: Electric field (in the z direction) at 50 nm from the rod surface, E_{50} (black squares) and characteristic electric field E^* (black circles) as a function of solution conductivity. Solid lines are power-law fits to the data. The fit results show that $E_{50} \propto \sigma^{-0.6}$, while $E^* \propto \sigma^{-0.988}$, implying an inverse relationship between E^* and solution conductivity.

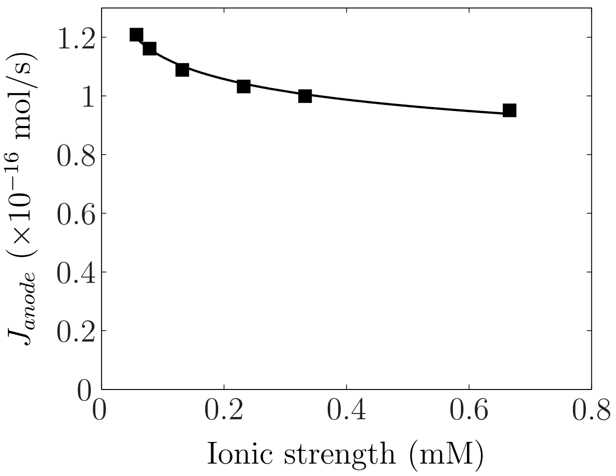

Figure 6.6: Total flux of protons out of the anode end as a function of solution ionic strength, varied using KCl. The addition of electrolyte alters the proton concentration in the diffuse layer, altering the reaction rate on the cathode such that leading to a net decrease in the reaction rates on both ends.

how the entire electric field distribution affects the rod on aggregate. We see from the fitting curve in Fig. 6.5 that E^* is roughly inversely proportional to conductivity, scaling as $E^* \propto \sigma^{-0.988}$.

Figure 6.6 visualizes the decrease in reaction-driven flux as a function of solution conductivity. As before, reaction-driven flux is given by the total flux out of the anode side,

$$J_{anode} = \int_{anode} j_{anode} dA, \tag{6.15}$$

where j_{anode} is given by (2.42). Again, due to current conservation, Fig. 6.6 would look identical if the ordinate variable were instead $J_{cathode}$.

To understand why the reaction rate seems to depend on conductivity, let us examine the reaction kinetic expressions, (2.42) and (2.43), which determine the total fluxes at the anode and cathode, respectively. The rate constants $K_{O,anode}$ and $K_{R,cathode}$ cannot be responsible for the decrease, as they are kept constant in all cases at the values indicated in table 6.2. The bulk hydrogen peroxide concentration is set to 1.11 mol/L for all of the simulations in Fig. 6.6, and the surface concentration

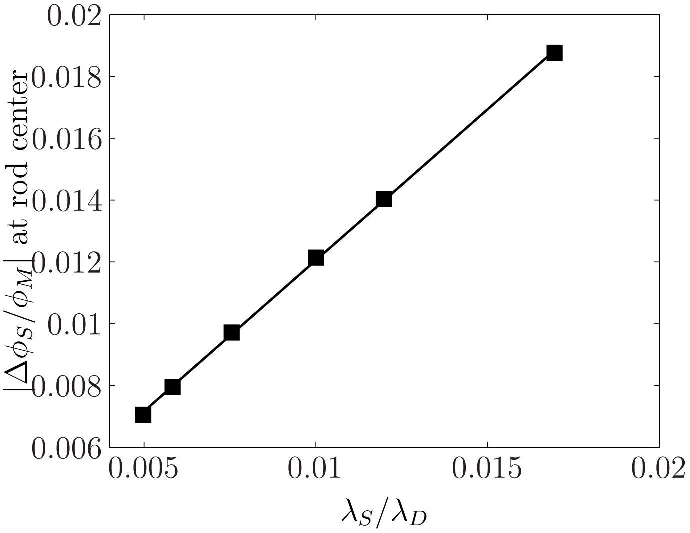

Figure 6.7: Magnitude of the Stern voltage divided by rod potential as a function of the ratio of Stern layer thickness to Debye thickness λ_S/λ_D, validating (2.23). The abscissa is varied by keeping λ_S constant at 2 Å and changing λ_D by adding KCl. Black squares indicate simulation data, with a linear fit line predicted by (2.23) superimposed.

of peroxide is never perturbed by more than 1 % from the bulk value in any of the cases considered in Fig. 6.6. Thus, the change in reaction rate with conductivity is due primarily to either the change in proton concentration with conductivity or the change in Stern-layer voltage with conductivity. Let us now examine the dependence on Stern voltage with solution conductivity, in order to assess whether it contributes significantly to the decrease in reaction rate.

Figure 6.7 shows the Stern voltage measured at the midpoint of the rod normalized by the rod potential, ϕ_M, as a function of the ratio λ_S/λ_D, showing a strong linear relationship and validating the scaling result (2.23). Considering that λ_S is a constant while λ_D depends inversely on the square root of ionic strength, the abscissa in Fig. 6.7 is proportional to the inverse square root of ionic strength. This figure suggests that the Stern voltage becomes more important as the salt concentration is increased. The agreement between Fig. 6.7 and (2.23) is robust considering that (2.23) assumes

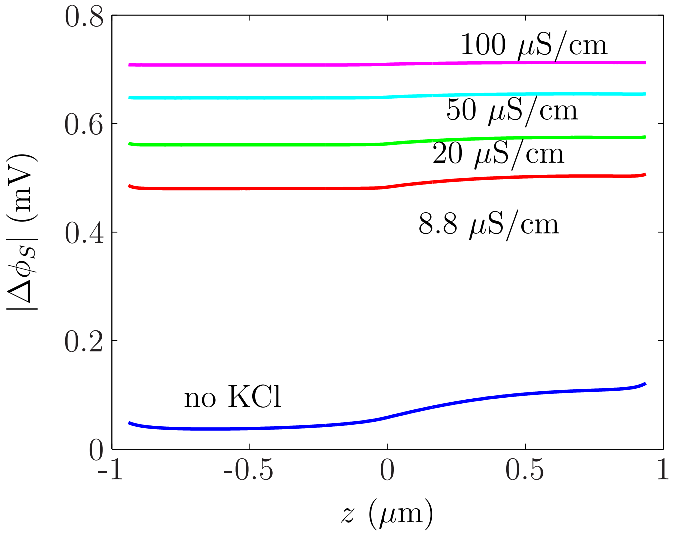

Figure 6.8: Magnitude of Stern voltage as a function of position along the rod for several different conductivities. Conductivity increases from the bottom to the top curve, and is varied by adding KCl. The left half of the plot ($z < 0$) corresponds to the cathode segment of the rod, and the right half ($z > 0$) to the anode segment. Stern voltage is controlled by the Stern-layer thickness and electric field normal to the surface. As conductivity is increased, the diffuse layer shrinks, steepening the potential gradient at the surface and increasing the Stern voltage.

the validity of the Debye-Hückel solution, which assumes that the surface potential is less than the thermal voltage; this assumption is not rigorously justified at the values of the zeta potential calculated for the rods, which can be up to three times the thermal voltage.

The inverse dependence of Stern voltage on conductivity is observed at other points along the rod as well. Figure 6.8 shows the absolute value of Stern voltage (since, as defined, the Stern voltage in these cases is negative) as a function of position along the rod at the indicated conductivities. According to the Stern model of the EDL, the electric potential gradient is extrapolated across the Stern layer, from the outer Helmholtz plane to the metal interior. Thus, the Stern voltage is linearly related to the normal electric field at the nanorod surface (see (2.19)). The variations in Stern voltage in Fig. 6.8 therefore arise from variations of the normal electric field with position along the surface. The Stern voltage is significantly higher than in Chapter 5, in which we do not consider added electrolytes; in that case the Stern voltage is of order 10^{-6} V.

However, it is unlikely that Stern voltage by itself is responsible for the decrease in reaction rate with conductivity visualized in Fig. 6.6. The maximum absolute value of the Stern voltage on the anode is attained when $\Delta\phi_S = -0.7127$ mV at 100 μS/cm, implying an exponential term in (2.42) equal to 0.973. Thus, the increase in Stern voltage should lead to a slight decrease in the reaction rate on the anode. The Stern voltage on the cathode reaches its maximum absolute value at a value of -0.7092 mV, also at 100 μS/cm, implying an exponential term of 1.028. The increase in Stern voltage leads to a slight increase in reaction rate on the cathode. Thus, the increase in Stern voltage with increasing conductivity tends to slightly increase the reaction rate on the cathode and slightly decrease the reaction rate on the anode.

Since current must still be conserved, the rod potential ϕ_M adjusts to compensate for the asymmetric change in reaction rates until the net currents out of the anode and into the anode are equal again. This requires that ϕ_M be made less negative, which favors oxidation and disfavors reduction, which evens out the reaction rates.

However, the Stern voltage cannot be the only reason for the decrease in reaction rate with increased conductivity because the increase occurs even if the Stern voltage terms are ignored. Test simulations, run with the Chang-Jaffé boundary conditions (5.2) and (5.3), show a decrease in reaction rate by a factor of 1.15 upon increasing the conductivity from 8.8 to 35 μS/cm. When the Stern voltage terms are included, the reaction rate decreases by a factor of 1.17 for the same conductivities. Thus, we conclude that the Stern-layer voltage makes a nonzero, but relatively insignificant difference in decreasing the reaction rates as conductivity increases. The rest of the decrease must be due to the change in the concentration of protons, which is plotted as a function of position along the rod for two different conductivities in Fig. 6.9.

In summary, as more electrolyte is added to the solution, the shrinking diffuse

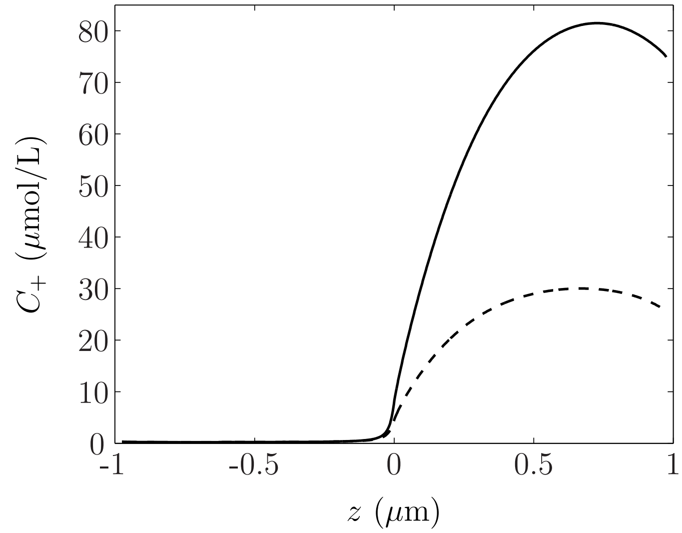

Figure 6.9: Proton concentration as a function of z along the surface of the rod for two conductivities: 8.8 μS/cm (solid line) and 100 μS/cm (dotted line). Positive z values indicated the anode; negative values indicate the cathode. The plot makes clear that protons are generated at the cathode at a slower rate in the high-conductivity case, due to the reduced reaction rates. As a result of current conservation, the proton concentration along the cathode is reduced, further limiting the cathode reaction rate (which depends on the square of proton concentration).

layer causes stronger radial electric fields at the particle surface, leading to a larger Stern voltage. The exponential terms in the Butler-Volmer equations (2.42,2.43) thus deviate further from unity as electrolyte concentration is increased. However, even at the highest salt concentration considered, the exponential terms are bounded by 0.97 and 1.03, and thus they likely exert relatively little influence on the reaction kinetics.

6.3.1 Speed Reduction Factors

Figure 6.2 shows that increasing the conductivity from 8.8 to 100 μS/cm, an increase of roughly an order of magnitude, leads to a decrease in speed from 22 to 1.11 μm/s, a decrease of roughly a factor of 20. As we have witnessed, this speed decrease is due to several factors, each of which cause a partial reduction in the swimming speed. In descending order of importance, these factors are (i) the decrease of the electric field due to the increase in solution conductivity, (ii) the decrease in magnitude of the area-averaged zeta potential with conductivity, and (iii) the decrease in reaction rate with solution conductivity.

As in the scaling analysis, we calculate the characteristic electric field E^* of the system as the electric field that would need to be externally applied to drive conventional electrophoresis of the rod at a speed equal to the measured swimming speed. As conductivity is increased from 8.8 to 100 μS/cm, the electric field E^* decreases from 415 to 38 V/m. Thus, between the minimum and maximum conductivities, the electric field E^* decreases by approximately 90 %:

$$\frac{E^*(\sigma = 100)}{E^*(\sigma = 8.8)} = 0.092. \tag{6.16}$$

Thus, the reduction in electric field reduces the swimming velocity of the rod by roughly an order of magnitude.

In all cases, the electrolyte added to the solution was at a significantly higher bulk concentration than protons and bicarbonate ions. While proton/bicarbonate concentration was kept fixed at 0.9 μmol/L, the electrolyte concentration was varied from

56.4 to 820 μmol/L. The counterions making up the electrolyte are attracted to the rod to help screen the surface charge. In doing so, and since they are more concentrated than protons, the net concentration of protons in the diffuse layer decreases due to the greater presence of electrolyte. When conductivity is increased from its minimum to its maximum value (8.8 to 100 μS/cm), the total reaction rates on the anode and cathode decrease by roughly 20 %:

$$\frac{J_{anode}(\sigma = 100)}{J_{anode}(\sigma = 8.8)} = 0.786, \tag{6.17}$$

where J_{anode} is again given by (6.15).

Due to the proportionality between speed and surface activity originally identified by Golestanian *et al.* [38] and also proposed and validated in the scaling analysis in this work (see (2.71)), we conclude that the reduction in reaction rate causes a decrease in swimming speed of roughly 20 % from the minimum to the maximum conductivity.

The decrease in reaction rates is asymmetric on the anode and cathode, which alters the value of the rod potential at which current is conserved. Rod potential is closely related to the zeta potential, as shown by (2.18), and so Fig. 6.4 shows that the zeta potential magnitude thus decreases upon the addition of salt. When the conductivity is raised from 8.8 to 100 μS/cm, the average zeta potential is observed to decrease from -67.9 mV to -37.1 mV. Thus, as conductivity is raised to its maximum value, the zeta potential decreases by approximately 45 %:

$$\frac{\bar{\zeta}(\sigma = 100)}{\bar{\zeta}(\sigma = 8.8)} = 0.546. \tag{6.18}$$

Thus the change in zeta potential causes a reduction in the swimming speed by roughly a factor of 2.

Since speed is linearly related to E^*, zeta potential, and reaction rate (see (2.71) and (6.3)), we can multiply the reduction factors in (6.16-6.18) together to obtain an estimate of the total velocity reduction factor caused by all three effects. The result is 0.04, which is in good agreement with the observed speed reduction factor of $U_{ev,\sigma=100}/U_{ev,\sigma=8.8} = 0.05$. Possible reasons for this small deviation could include the fact that current was not perfectly conserved (we stop the simulations when the total flux of the anode and total flux into the cathode differ by less than 1 %).

6.4 Conclusion

In this chapter, we have explored the physical reasons for the observed inverse dependence of swimming speed on solution conductivity. We have found that the speed decrease can be attributed to three main effects: the decrease in zeta potential with electrolyte concentration, the decrease in reaction-driven flux with electrolyte concentration, and the decrease in electric field due to the increase in conductivity. These results seem to suggest that the self-electrophoresis mechanism is inherently susceptible to speed reductions brought about by adding salt; thus, it appears that self-electrophoretic nanomotors are not practical for salt-rich environments in general (although silver solutions have been shown to produce a significant speed increase [50]). An alternative nanomotor which has been proven capable of transporting cargo in salt-rich environments was studied by Wang's group [63].

Chapter 7

CONCLUSIONS

In this thesis, we have developed a mathematical model for the electrokinetic locomotion of bimetallic nanorod particles. The model has been tested through computational simulations, whose results were compared to previous experimental and analytical results. The simulations show strong evidence that the rod movement is the result of fluid slip driven by electrical body forces, which in turn are generated by a coupling of free charge in the solution and the reaction-induced electric fields. Important trends in the rods' behavior may be identified and understood through the scaling analysis developed in §2.6 for uncharged and charged rods. Finally, we have sought to deepen our understanding of whether the conductivity-induced speed decrease is an inherent limitation on the rods, or if it may be overcome. In this chapter we assess the contributions as well as the shortcomings of the results presented here.

The results in this thesis have illuminated the importance of the surface charge on the rod in generating the motion. In the case of the uncharged rod, §4.3, no locomotion was observed. When surface charge was included in the uncoupled (§4.4) and coupled (§5.3) models, the magnitude of the surface charge was shown to be directly related to the swimming speed. Additional simulations have shown that if the sign of the surface charge is reversed, the motion occurs at the same speed but in the opposite direction. Finally, for the cases in which we vary electrolyte conductivity and ionic strength (§6.3), the differences in speed between rods in different salts at the same conductivity can partially be traced to differences in rod potential at those conductivities. The magnitude and sign of the surface charge determine the speed and direction of the motion; without surface charge, the rod does not move.

Given the importance of the surface charge, it might seem surprising that we have not accounted for the possible effect of surface adsorption on the zeta potential. Here, our focus has primarily been on describing the physical phenomena occurring in the fluid, and on describing the effect of the reactions on the zeta potential, which has not been described in the literature in detail. Incorporation of surface adsorption into a future model of a self-propelling particle would be relatively straightforward.

Through the use of an appropriate adsorption isotherm, the amount of charged and uncharged species bound to the surface could be determined, giving an estimate of the resulting surface charge density due to adsorption, which will likely be different on the anode and athode. From the charge density, the contribution of adsorption to the zeta potential could be computed relatively easily.

This thesis has argued that the internal rod potential ϕ_M that satisfies the current conservation constraint (2.47) directly influences the potential at the outer Helmholtz plane (OHP), which we have defined here to be the zeta potential. Similar arguments can be found in the works of Bard and Faulkner [5] and Bazant *et al.* [6]. Regardless of the relative importance of the reaction-determined rod potential or surface adsorption, this work makes clear that the potential at the surface is directly related to the swimming speed, and plausible swimming speeds are obtained if the surface potential is between -10 and -70 mV. The impact of the internal electrode potential on the zeta potential of a self-electrophoretic particle has only recently been considered outside of this work, by Sabass & Seifert [84], who used similar boundary conditions to those presented here.

In this thesis we have considered the peroxide oxidation and reduction reactions as single-step processes. This is likely a simplifying assumption. It is widely believed that the electrochemical oxidation of H_2O_2 on platinum surfaces proceeds at least one intermediate step. Hall *et al.* [41] proposed a mechanism incorporating reversible binding of peroxide to electrochemically generated Pt(II) surface sites, inhibitory binding of O_2 to these same sites, and a side reaction involving protonation of an adsorbed H_2O_2 complex. Sabass & Seifert [84] recently proposed reaction schemes for the reduction and oxidation of H_2O_2. They concluded that if intermediate steps are accounted for, both processes are likely first-order in H_2O_2 concentration. They also assumed the peroxide reduction reaction was first-order in H^+ concentration, but allowed for the possibility of a second-order dependence on proton concentration, which we have considered here.

This work, along with others, has established that the ideal conditions for fast self-electrophoretic swimming exist when the bulk solution conductivity is low. In addition, we have seen that surface charge is essential for locomotion to occur. In the vicinity of the rod surface, the conductivity is elevated from its bulk value due to the enrichment of ions in the diffuse layer. The greater the surface charge, the more significant the enrichment. Therefore, conditions for swimming are most favorable when the conductivity is significantly higher in the diffuse layer than in the bulk solution. In this case, the Dukhin number, which tells the relative importance of surface conduction to bulk conduction, should be finite, and surface conduction may be important. What role does surface conduction have to play in self-electrophoresis?

I have begun to investigate this issue using data from the simulations presented here. By estimating the Dukhin number of the rod from the established formula for the Dukhin number of a 2-μm-diameter spherical particle, I observed a linear correlation between swimming speed and Dukhin number, implying that the presence of surface conduction, at the very least, does not impede self-electrophoresis. The question to be answered is, of course, whether this correlation is indicative of a causal link between surface conduction and self-electrophoresis. Khair & Squires [53] recently showed that for highly charged particles undergoing conventional, externally driven electrophoresis, surface conduction effectively leads to a *decrease* in electrophoretic mobility. Thus, surface conduction may enhance motion by self-electrophoresis, but has been shown to hinder conventional electrophoresis. Future work could explore this somewhat counter-intuitive result, *e.g.* by obtaining an asymptotic or numerical solution to the governing equations for a simple swimmer undergoing self-electrophoresis, specifically accounting for surface conduction, following the methods of O'Brien [71] and Khair & Squires [53], and seeing if the same trend of speed versus Dukhin number emerges. A better understanding of the relationship between surface conduction and self-electrophoretic swimming could help us better understand why the swimming speed decreases rapidly with an increase in electrolyte concentration, which stands as one of the most important issues facing self-electrophoretic swimmers.

Given the growing interest in self-propelling micro- and nanoparticles [97, 31, 90], the development of accurate, predictive models for nanoscale self-propelled motion is timely. Many prototypes of practical nanomotors exist whose propulsion mechanisms are poorly understood. In this thesis, we have taken a few steps toward the goal of understanding the motion of one important subclass of nanomotors, and have thus contributed to the physical understanding of electrokinetic locomotion.

BIBLIOGRAPHY

[1] JL Anderson, ME Lowell, and DC Prieve. Motion of a particle generated by chemical gradients .1. Non-Electrolytes. *Journal of Fluid Mechanics*, 117(Apr):107–121, 1982.

[2] John Anderson. Colloid transport by interfacial forces. *Annual Review of Fluid Mechanics*, 21:61–100, 1989.

[3] J. E. Avron, O. Kenneth, and D. H. Oaknin. Pushmepullyou: an efficient micro-swimmer. *New Journal of Physics*, 7, November 2005.

[4] Shankar Balasubramanian, Daniel Kagan, Kalayil Manian Manesh, Percy Calvo-Marzal, Gerd-Uwe Flechsig, and Joseph Wang. Thermal modulation of nanomotor movement. *Small*, 5(13):1569–1574, 2009.

[5] Allen J. Bard and Larry R. Faulkner. *Electrochemical Methods: Fundamentals and Applications*. Wiley, New York, 2 edition, December 2000.

[6] M. Z. Bazant, K. T. Chu, and B. J. Bayly. Current-voltage relations for electrochemical thin films. *SIAM Journal on Applied Mathematics*, 65(5):1463–1484, 2005.

[7] Martin Z. Bazant and Todd M. Squires. Induced-Charge electrokinetic phenomena: Theory and microfluidic applications. *Physical Review Letters*, 92(6):066101, February 2004.

[8] Jason J. Benkoski, Jennifer L. Breidenich, O. Manuel Uy, Allen T. Hayes, Ryan M. Deacon, H. Bruce Land, Jane M. Spicer, Pei Yuin Keng, and Jeffrey Pyun. Dipolar organization and magnetic actuation of flagella-like nanoparticle assemblies. *Journal of Materials Chemistry*, 21(20):7314–7325, 2011.

[9] P.M. Biesheuvel, M. van Soestbergen, and M.Z. Bazant. Imposed currents in galvanic cells. *Electrochimica Acta*, 54(21):4857–4871, August 2009.

[10] Jared Burdick, Rawiwan Laocharoensuk, Philip M. Wheat, Jonathan D. Posner, and Joseph Wang. Synthetic nanomotors in microchannel networks: Directional microchip motion and controlled manipulation of cargo. *Journal of the American Chemical Society*, 130(26):8164–8165, July 2008.

[11] Percy Calvo-Marzal, Kalayil Manian Manesh, Daniel Kagan, Shankar Balasubramanian, Maria Cardona, Gerd-Uwe Flechsig, Jonathan Posner, and Joseph Wang. Electrochemically-triggered motion of catalytic nanomotors. *Chemical Communications*, (30):4509–4511, 2009.

[12] J. M. Catchmark, S. Subramanian, and A. Sen. Directed rotational motion of microscale objects using interfacial tension gradients continually generated via catalytic reactions. *Small*, 1(2):202–206, February 2005.

[13] Hung-Chi Chang and George Jaffé. Polarization in electrolytic solutions. part i. theory. *The Journal of Chemical Physics*, 20(7):1071, 1952.

[14] Kevin T. Chu. *Asymptotic Analysis of Extreme Electrochemical Transport*. PhD thesis, Massachusetts Institute of Technology, 2005.

[15] Ubaldo M. Córdova-Figueroa and John F. Brady. Osmotic propulsion: The osmotic motor. *Physical Review Letters*, 100(15), 2008.

[16] Ubaldo M. Córdova-Figueroa and John F. Brady. Córdova-figueroa and brady reply:. *Physical Review Letters*, 102(15):159802, April 2009.

[17] Ubaldo M. Córdova-Figueroa and John F. Brady. Córdova-figueroa and brady reply:. *Physical Review Letters*, 103(7):079802, August 2009.

[18] Paul Delahay. *Double Layer and Electrode Kinetics*. Interscience, 1965.

[19] U. Korcan Demirok, Rawiwan Laocharoensuk, Kalayil Manian Manesh, and Joseph Wang. Ultrafast catalytic alloy nanomotors. *Angewandte Chemie International Edition*, 47(48):93499351, 2008.

[20] BV Derjaguin, SS Dukhin, and AA Korotkova. Diffusiophoresis in electrolyte solutions and its role in mechanism of film formation from rubber latexes by method of ionic deposition. *Kolloidnyi Zhurnal*, 23(1):53–&, 1961.

[21] Rahul Dhopeshwarkar, Dzmitry Hlushkou, Mark Nguyen, Ulrich Tallarek, and Richard M Crooks. Electrokinetics in microfluidic channels containing a floating electrode. *Journal of the American Chemical Society*, 130(32):10480–10481, August 2008.

[22] George M Dougherty, Klint A Rose, Jeffrey B. -H Tok, Satinderpall S Pannu, Frank Y. S Chuang, Michael Y Sha, Gabriela Chakarova, and Sharron G Penn. The zeta potential of surface-functionalized metallic nanorod particles in aqueous solution. *Electrophoresis*, 29(5):1131–1139, March 2008.

[23] H. -Y Du, C. -H Wang, H. -C Hsu, S. -T Chang, U. -S Chen, S. C Yen, L. C Chen, H. -C Shih, and K. H Chen. Controlled platinum nanoparticles uniformly dispersed on nitrogen-doped carbon nanotubes for methanol oxidation. *Diamond and Related Materials*, 17(4-5):535–541, May 2008.

[24] SS Dukhin and BV Derjaguin. *Electrokinetic Phenomena*, volume 7 of *Surface and Colloid Science*. John Wiley & Sons, 1974.

[25] J. F. L. Duval. Electrokinetics of the amphifunctional metal/electrolyte solution interface in the presence of a redox couple. *Journal of Colloid and Interface Science*, 269(1):211–223, January 2004.

[26] J. F. L. Duval, G. K. Huijs, W. F. Threels, J. Lyklema, and H. P. van Leeuwen. Faradaic depolarization in the electrokinetics of the metal-electrolyte solution interface. *Journal of Colloid and Interface Science*, 260(1):95–106, April 2003.

[27] J. F. L. Duval, H. P. van Leeuwen, J. Cecilia, and J. Galceran. Rigorous analysis of reversible faradaic depolarization processes in the electrokinetics of the metal/electrolyte solution interface. *The Journal of Physical Chemistry B*, 107(28):6782–6800, July 2003.

[28] Jérôme F. L. Duval, Jacques Buffle, and Herman P. van Leeuwen. Quasi-reversible faradaic depolarization processes in the electrokinetics of the Metal/Solution interface. *The Journal of Physical Chemistry B*, 110(12):6081–6094, March 2006.

[29] Stephen Ebbens, Richard A. L. Jones, Anthony J. Ryan, Ramin Golestanian, and Jonathan R. Howse. Self-assembled autonomous runners and tumblers. *Physical Review E*, 82(1):015304, July 2010.

[30] Stephen Ebbens, Mei-Hsien Tu, Jonathan R. Howse, and Ramin Golestanian. Size dependence of the propulsion velocity for catalytic janus-sphere swimmers. *Physical Review E*, 85(2):020401, February 2012.

[31] Stephen J. Ebbens and Jonathan R. Howse. In pursuit of propulsion at the nanoscale. *Soft Matter*, 6(4):726, 2010.

[32] Stephen J. Ebbens and Jonathan R. Howse. Direct observation of the direction of motion for spherical catalytic swimmers. *Langmuir*, 27(20):12293–12296, October 2011.

[33] Thomas M. Fischer and Prajnaparamita Dhar. Comment on Osmotic propulsion: The osmotic motor. *Physical Review Letters*, 102(15):159801, April 2009.

[34] S. Fournier-Bidoz, A. C. Arsenault, I. Manners, and G. A. Ozin. Synthetic self-propelled nanorotors. *Chemical Communications*, (4):441–443, January 2005.

[35] A. Frumkin. Hydrogen overvoltage and the structure of the double layer. *Zeitschrift fur Physikalische Chemie-Abteilung A - Chemische Thermodynamik Kinetik Elektrochemie Eigenschaftslehre*, 164(1/2):121–133, March 1933.

[36] Wei Gao, Allen Pei, and Joseph Wang. Water-driven micromotors. *ACS nano*, August 2012. PMID: 22891973.

[37] Ambarish Ghosh and Peer Fischer. Controlled propulsion of artificial magnetic nanostructured propellers. *Nano Letters*, 9(6):2243–2245, June 2009.

[38] R. Golestanian, T. B. Liverpool, and A. Ajdari. Designing phoretic micro- and nano-swimmers. *New Journal of Physics*, 9(5):126, 2007.

[39] Ramin Golestanian, Tanniemola B. Liverpool, and Armand Ajdari. Propulsion of a molecular machine by asymmetric distribution of reaction products. *Physical Review Letters*, 94(22), 2005.

[40] Nicolas G Green and Thomas B Jones. Numerical determination of the effective moments of non-spherical particles. *Journal of Physics D - Applied Physics*, 40(1):78–85, January 2007.

[41] Simon B. Hall, Emad A. Khudaish, and Alan L. Hart. Electrochemical oxidation of hydrogen peroxide at platinum electrodes. part 1. an adsorption-controlled mechanism. *Electrochimica Acta*, 43(56):579–588, November 1997.

[42] D. C. Henry. The cataphoresis of suspended particles. part i. the equation of cataphoresis. *Proceedings of the Royal Society of London. Series A, Containing Papers of a Mathematical and Physical Character*, 133(821), September 1931.

[43] Dzmitry Hlushkou, Robbyn K Perdue, Rahul Dhopeshwarkar, Richard M Crooks, and Ulrich Tallarek. Electric field gradient focusing in microchannels with embedded bipolar electrode. *Lab on a Chip*, 9(13):1903–1913, 2009.

[44] James F. Hoburg and James R. Melcher. Internal electrohydrodynamic instability and mixing of fluids with orthogonal field and conductivity gradients. *Journal of Fluid Mechanics*, 73(2):333–351, 1976.

[45] Jonathan R Howse, Richard A. L Jones, Anthony J Ryan, Tim Gough, Reza Vafabakhsh, and Ramin Golestanian. Self-motile colloidal particles: From directed propulsion to random walk. *Physical Review Letters*, 99(4), July 2007.

[46] Jyh-Ping Hsu, James Lou, Yan-Ying He, and Eric Lee. Diffusiophoresis of concentrated suspensions of spherical particles with distinct ionic diffusion velocities. *The Journal of Physical Chemistry B*, 111(10):2533–2539, March 2007.

[47] R. F. Ismagilov, A. Schwartz, N. Bowden, and G. M. Whitesides. Autonomous movement and self-assembly. *Angewandte Chemie-International Edition*, 41(4):652–654, 2002.

[48] Thomas B. Jones. *Electromechanics of particles.* Cambridge University Press, 1995.

[49] Frank Jülicher and Jacques Prost. Comment on Osmotic propulsion: The osmotic motor. *Physical Review Letters*, 103(7):079801, August 2009.

[50] Daniel Kagan, Percy Calvo-Marzal, Shankar Balasubramanian, Sirilak Sattayasamitsathit, Kalayil Manian Manesh, Gerd-Uwe Flechsig, and Joseph Wang. Chemical sensing based on catalytic nanomotors: Motion-Based detection of trace silver. *Journal of the American Chemical Society*, 131(34):12082+, September 2009.

[51] Huan J. Keh and Yeu K. Wei. Diffusiophoretic mobility of spherical particles at low potential and arbitrary double-layer thickness. *Langmuir*, 16(12):5289–5294, June 2000.

[52] Arturo A Keller, Hongtao Wang, Dongxu Zhou, Hunter S Lenihan, Gary Cherr, Bradley J Cardinale, Robert Miller, and Zhaoxia Ji. Stability and aggregation of metal oxide nanoparticles in natural aqueous matrices. *Environmental Science & Technology*, 44(6):1962–1967, March 2010.

[53] Aditya S. Khair and Todd M. Squires. The influence of hydrodynamic slip on the electrophoretic mobility of a spherical colloidal particle. *Physics of Fluids*, 21(4):042001–042001–14, April 2009.

[54] T. R. Kline, W. F. Paxton, T. E. Mallouk, and A. Sen. Catalytic nanomotors: Remote-controlled autonomous movement of striped metallic nanorods. *Angewandte Chemie - International Edition*, 44(5):744–746, 2005.

[55] T. R. Kline, W. F. Paxton, Y. Wang, D. Velegol, T. E. Mallouk, and A. Sen. Catalytic micropumps: Microscopic convective fluid flow and pattern formation. *Journal of the American Chemical Society*, 127(49):17150–17151, December 2005.

[56] Timothy R Kline, Jodi Iwata, Paul E Lammert, Thomas E Mallouk, Ayusman Sen, and Darrell Velegol. Catalytically driven colloidal patterning and transport. *Journal of Physical Chemistry B*, 110(48):24513–24521, December 2006.

[57] P. E. Lammert, J. Prost, and R. Bruinsma. Ion drive for vesicles and cells. *Journal of Theoretical Biology*, 178(4):387–391, February 1996.

[58] R. Laocharoensuk, J. Burdick, and J. Wang. Carbon-nanotube-induced acceleration of catalytic nanomotors. *ACS Nano*, 2(5):1069–1075, 2008.

[59] Eric Lauga and Thomas R Powers. The hydrodynamics of swimming microorganisms. *Reports on Progress in Physics*, 72(9), September 2009.

[60] Derek R Laws, Dzmitry Hlushkou, Robbyn K Perdue, Ulrich Tallarek, and Richard M Crooks. Bipolar electrode focusing: Simultaneous concentration enrichment and separation in a microfluidic channel containing a bipolar electrode. *Analytical Chemistry*, 81(21):8923–8929, November 2009.

[61] H. Lin, B. D. Storey, M. H. Oddy, C. H. Chen, and J. G. Santiago. Instability of electrokinetic microchannel flows with conductivity gradients. *Physics of Fluids*, 16(6):1922–1935, June 2004.

[62] EJ Lund. *Bioelectric fields and growth.* U. Texas Press, Austin, 1947.

[63] Kalayil Manian Manesh, Maria Cardona, Rodger Yuan, Michael Clark, Daniel Kagan, Shankar Balasubramanian, and Joseph Wang. Template-assisted fabrication of salt-independent catalytic tubular microengines. *Acs Nano*, 4(4):1799–1804, April 2010.

[64] N. Mano and A. Heller. Bioelectrochemical propulsion. *Journal of the American Chemical Society*, 127(33):11574–11575, August 2005.

[65] B. R. Martin, D. J. Dermody, B. D. Reiss, M. M. Fang, L. A. Lyon, M. J. Natan, and T. E. Mallouk. Orthogonal self-assembly on colloidal gold-platinum nanorods. *Advanced Materials*, 11(12):1021–1025, August 1999.

[66] P. Mitchell. Self-Electrophoretic locomotion in microorganisms - bacterial flagella as giant ionophores. *FEBS Letters*, 28(1):1–4, 1972.

[67] Peter Mitchell. Hypothetical thermokinetic and electrokinetic mechanisms of locomotion in micro-organisms. *Proceedings of the Royal Physical Society of Edinburgh*, 25, 1956.

[68] J. L. Moran, P. M. Wheat, and J. D. Posner. Locomotion of electrocatalytic nanomotors due to reaction induced charge autoelectrophoresis. *Physical Review E*, 81(6):065302, June 2010.

[69] Guru Navaneetham and Jonathan D. Posner. Electrokinetic instabilities of non-dilute colloidal suspensions. *Journal of Fluid Mechanics*, 619:331, 2009.

[70] J. Newman and K.E. Thomas-Alyea. *Electrochemical Systems*. The Electrochemical Society Series. Wiley, 2004.

[71] R.W O'Brien. The solution of the electrokinetic equations for colloidal particles with thin double layers. *Journal of Colloid and Interface Science*, 92(1):204–216, March 1983.

[72] G. A. Ozin, I. Manners, S. Fournier-Bidoz, and A. Arsenault. Dream nanomachines. *Advanced Materials*, 17(24):3011–3018, December 2005.

[73] Ryan A. Pavlick, Samudra Sengupta, Timothy McFadden, Hua Zhang, and Ayusman Sen. A polymerization-powered motor. *Angewandte Chemie International Edition*, 50(40):93749377, 2011.

[74] W. F. Paxton, K. C. Kistler, C. C. Olmeda, A. Sen, S. K. St Angelo, Y. Y. Cao, T. E. Mallouk, P. E. Lammert, and V. H. Crespi. Catalytic nanomotors: Autonomous movement of striped nanorods. *Journal of the American Chemical Society*, 126(41):13424–13431, October 2004.

[75] W. F. Paxton, A. Sen, and T. E. Mallouk. Motility of catalytic nanoparticles through self-generated forces. *Chemistry - A European Journal*, 11(22):6462–6470, November 2005.

[76] Walter F Paxton, Paul T Baker, Timothy R Kline, Yang Wang, Thomas E Mallouk, and Ayusman Sen. Catalytically induced electrokinetics for motors and micropumps. *Journal of the American Chemical Society*, 128(46):14881–14888, November 2006.

[77] TP Pitta and HC Berg. Self-Electrophoresis is not the mechanism for motility in swimming cyanobacteria. *Journal of Bacteriology*, 177(19):5701–5703, October 1995.

[78] M. N. Popescu, S. Dietrich, M. Tasinkevych, and J. Ralston. Phoretic motion of spheroidal particles due to self-generated solute gradients. *European Physical Journal E*, 31(4):351–367, April 2010.

[79] Jonathan D. Posner and Juan G. Santiago. Convective instability of electrokinetic flows in a cross-shaped microchannel. *Journal of Fluid Mechanics*, 555:1, 2006.

[80] DC Prieve, JL Anderson, JP Ebel, and ME Lowell. Motion of a particle generated by chemical gradients .2. electrolytes. *Journal of Fluid Mechanics*, 148:247–269, 1984.

[81] E. M. Purcell. Life at low reynolds number. *American Journal of Physics*, 45(1):3–11, January 1977.

[82] Raúl A. Rica and Martin Z. Bazant. Electrodiffusiophoresis: Particle motion in electrolytes under direct current. *Physics of Fluids*, 22(11):112109, 2010.

[83] Klint A. Rose, John A. Meier, George M. Dougherty, and Juan G. Santiago. Rotational electrophoresis of striped metallic microrods. *Physical Review E*, 75(1):011503, January 2007.

[84] Benedikt Sabass and Udo Seifert. Nonlinear, electrocatalytic swimming in the presence of salt. *Journal of Chemical Physics*, 136(21), June 2012.

[85] David Saintillan, Eric Darve, and Eric S. G. Shaqfeh. Hydrodynamic interactions in the Induced-Charge electrophoresis of colloidal rod dispersions. *Journal of Fluid Mechanics*, 563(-1):223–259, 2006.

[86] David Saintillan, Eric S. G. Shaqfeh, and Eric Darve. Stabilization of a suspension of sedimenting rods by induced-charge electrophoresis. *Physics of Fluids*, 18(12):121701, 2006.

[87] Timothy Sanchez, David Welch, Daniela Nicastro, and Zvonimir Dogic. Cilia-like beating of active microtubule bundles. *Science*, 333(6041):456–459, July 2011.

[88] Olaf Schenk and Klaus Gärtner. Solving unsymmetric sparse systems of linear equations with PARDISO. *Future Generation Computer Systems*, 20(3):475–487, April 2004.

[89] Olaf Schenk and Klaus Gärtner. On fast factorization pivoting methods for sparse symmetric indefinite systems. *Electronic Transactions on Numerical Analysis*, 23:158–179, 2006.

[90] Samudra Sengupta, Michael E. Ibele, and Ayusman Sen. Fantastic voyage: Designing self-powered nanorobots. *Angewandte Chemie International Edition*, 51(34):84348445, 2012.

[91] Alexander A. Solovev, Samuel Sanchez, Martin Pumera, Yong Feng Mei, and Oliver G. Schmidt. Magnetic control of tubular catalytic microbots for the transport, assembly, and delivery of micro-objects. *Advanced Functional Materials*, 20(15):2430–2435, August 2010.

[92] Josef Spek. Zustandsnderungen der plasmakolloide bei befruchtung und entwicklung des Nereis-Eies. *Protoplasma*, 9(1):370–427, 1930.

[93] T. M. Squires and M. Z. Bazant. Induced-charge electro-osmosis. *Journal of Fluid Mechanics*, 509:217–252, June 2004.

[94] Todd M. Squires and Martin Z. Bazant. Breaking symmetries in induced-charge electro-osmosis and electrophoresis. *Journal of Fluid Mechanics*, 560:65, 2006.

[95] Po Staffeld and Ja Quinn. Diffusion-induced banding of colloid particles via diffusiophoresis .2. non-electrolytes. *Journal of Colloid and Interface Science*, 130(1):88–100, June 1989.

[96] Shakuntala Sundararajan, Paul E Lammert, Andrew W Zudans, Vincent H Crespi, and Ayusman Sen. Catalytic motors for transport of colloidal cargo. *Nano Letters*, 8(5):1271–1276, May 2008.

[97] Joseph Wang. Can Man-Made nanomachines compete with nature biomotors? *ACS Nano*, 3(1):4–9, 2009.

[98] Yang Wang, Rose M Hernandez, Jr. Bartlett, Julia M Bingham, Timothy R Kline, Ayusman Sen, and Thomas E Mallouk. Bipolar electrochemical mechanism for the propulsion of catalytic nanomotors in hydrogen peroxide solutions. *Langmuir*, 22(25):10451–10456, December 2006.

[99] JB Waterbury, JM Willey, DG Franks, FW Valois, and SW Watson. A cyanobacterium capable of swimming motility. *Science*, 230(4721):74–76, 1985.

[100] Li Zhang, Jake J. Abbott, Lixin Dong, Bradley E. Kratochvil, Dominik Bell, and Bradley J. Nelson. Artificial bacterial flagella: Fabrication and magnetic control. *Applied Physics Letters*, 94(6), February 2009.

[101] Yang Zhang, Yongsheng Chen, Paul Westerhoff, Kiril Hristovski, and John C Crittenden. Stability of commercial metal oxide nanoparticles in water. *Water Research*, 42(8-9):2204–2212, April 2008.